ICFO

PhD Dissertation

Dynamics of optically levitated nanoparticles in high vacuum

Supervisor:
Prof. Romain Quidant

Author:
Jan Gieseler

Co-Supervisor:
Prof. Lukas Novotny

February 3rd, 2014

Dedicated to Marie Emilia Gieseler

Contents

Introduction

0.1 Motivation

Nanotechnology was named one of the key enabling technologies by the european commission [Europe, 2012] and it's tremendous impact on technology was envisioned early by 20^{th} century physicist R.Feynman in his now oft-quoted talk "Plenty of Room at the bottom" [Feynman, 1960].
Nanotechnology and nanoscience deal with structures barely visible with an optical microscope, yet much bigger than simple molecules. Matter at this mesoscale is often awkward to explore. It contains too many atoms to be easily understood by straightforward application of quantum mechanics (although the fundamental laws still apply). Yet, these systems are not so large as to be completely free of quantum effects; thus, they do not simply obey the classical physics governing the macroworld. It is precisely in this intermediate regime, the mesoworld, that unforeseen properties of collective systems emerge [Roukes, 2001]. To fully exploit the potential of nanotechnology, a thorough understanding of these properties is paramount.

The objective of the present thesis is to investigate and to control the dynamics of an optically levitated particle in high vacuum. This system belongs to the broader class of nanomechanical oscillators. Nanomechanical oscillators exhibit high resonance frequencies, diminished active masses, low power consumption and high quality factors - significantly higher than those of electrical circuits [Ekinci and Roukes, 2005]. These attributes make

them suitable for sensing [Chaste et al., 2012; Moser et al., 2013; Cleland and Roukes, 1998; Yang et al., 2006; Arlett et al., 2011], transduction [Lin et al., 2010; Bagci et al., 2013; Unterreithmeier et al., 2009] and signal processing [Liu et al., 2008]. Furthermore, nanomechanical systems are expected to open up investigations of the quantum behaviour of mesoscopic systems. Testing the predictions of quantum theory on meso- to macroscopic scales is one of todays outstanding challenges of modern physics and addresses fundamental questions on our understanding of the world [Kaltenbaek et al., 2012].

The state-of-the-art in nanomechanics itself has exploded in recent years, driven by a combination of interesting new systems and vastly improved fabrication capabilities [Verhagen et al., 2012; Eichenfield et al., 2009; Sankey et al., 2010]. Despite major breakthroughs, including ground state cooling [O'Connell et al., 2010], observation of radiation pressure shot noise [Purdy et al., 2013], squeezing [Safavi-Naeini et al., 2013] and demonstrated ultra-high force [Moser et al., 2013] and mass sensitivity [Chaste et al., 2012; Hanay et al., 2012; Yang et al., 2006], difficulties in reaching ultra-high mechanical quality (Q) factors still pose a major limitation for many of the envisioned applications. Micro-fabricated mechanical systems are approaching fundamental limits of dissipation [Cleland and Roukes, 2002; Mohanty et al., 2002], thereby limiting their Q-factors. In contrast to micro-fabricated devices, optically trapped nanoparticles in vacuum do not suffer from clamping losses, hence leading to much larger Q-factors.

0.2 Overview and state of the art

At the beginning of the present PhD thesis (early 2009), quantum optomechanics had just emerged as a promising route toward observing quantum behaviour at increasingly large scales. Thus far, most experimental efforts had focused on cooling mechanical systems to their quantum ground states, but significant improvements in mechanical quality (Q) factors are gener-

ally needed to facilitate quantum coherent manipulation. This is difficult given that many mechanical systems are approaching fundamental limits of dissipation [Cleland and Roukes, 2002; Mohanty et al., 2002]. To overcome the limitations set by dissipation, I developed an experiment to trap and cool nanoparticles in high vacuum.

Figure 1 summarises the content of the thesis. It consists of six chapters, ranging from a detailed description of the experimental apparatus (chapter 1) and proof-of-principle experiments (parametric feedback cooling - chapter 3) to the first observation of phenomena owing to the unique parameters of this novel optomechanical system (thermal nonlinearities - chapter 5). Aside from optomechanics and optical trapping, the topics covered include the dynamics of complex (nonlinear) systems (chapter 4) and the experimental and theoretical study of fluctuation theorems (non-equilibrium relaxation - chapter 6), the latter playing a pivotal role in statistical physics.

0.2.1 Optomechanics and optical trapping

Except for Ashkin's seminal work on optical trapping of much larger micro-sized particles from the early seventies [Ashkin, 1970, 1971; Ashkin and Dziedzic, 1976], there was no further experimental work and little theoretical work [Libbrecht and Black, 2004] on optical levitation in vacuum published at the time. Still, trapping in air had been demonstrated by different groups [Summers et al., 2008; Omori et al., 1997]. Two years later, Li et al. demonstrated linear feedback cooling of micron sized particles [Li et al., 2011] in high vacuum. However, due to fundamental limits set by recoil heating, nanoscale particles are necessary to reach the quantum regime. During my thesis, I developed a novel parametric feedback mechanism for cooling and built an experimental setup, which is capable of trapping and cooling nanoparticles in high vacuum (c.f. chapters 3 and 1). The combination of nanoparticles and vacuum trapping results in a very light and ultra-high-Q mechanical oscillator. In fact, the Q-factor achieved with this setup is the highest observed so far in any nano- or micromechanical system.

	Chapter	Summary	Main Result
1.	**Experimental Setup**	Description of the experimental apparatus, which allows to trap and cool single dielectric nanoparticles in high vacuum.	Trapping of nanoparticles in high vacuum is achieved by a novel parametric feedback scheme, which allows for thee dimensional cooling with a single laser beam. Subwavelength particles can be trapped by single beam because the optical gradient force dominates over the scattering force. Demonstrated cooling from room temperature to 50mK and ultra-high Q-factors exceeding 100 million.
2.	**Theory of optical tweezers**	A simple model is provided to gain insight into the optical forces and the conditions under which single beam trapping in vacuum can be achieved.	
3.	**Parametric Feedback Cooling**	Experimental demonstration of parametric feedback cooling.	
4.	**Dynamics of driven particle**	Study of the nonlinear dynamics of a levitated nanoparticle under deterministic parametric driving	Particle dynamics is well explained by a Duffing model. The Duffing nonlinearity has it's origin in the shape of the optical potential.
5.	**Thermal Nonlinearities**	Study of the dynamics of a levitated nanoparticle under stochastic (thermal) driving.	First observation of nonlinear thermal motion in a mechanical oscillator, enabled by a combination of high Q and low mass.
6.	**Relaxation from non-Equilibrium**	Study of relaxation dynamics to thermal equilibrium from non-equilibrium steady states.	Validation of fluctuation theorem for relaxation dynamics from non-equilibrium steady states.

Figure 1: **Overview of the thesis.** *The thesis consists of the six chapters summarised above.*

0.2.2 Complex systems

Discovering new effects by either pushing existing techniques to their fundamental limit or by developing new ones is the main motivation behind

fundamental research. The exceptional high Q-factor in combination with the low mass of the vacuum trapped nanoparticle allowed me to observe a novel dynamic regime in which thermal excitations suffice to drive a mechanical oscillator into the nonlinear regime (c.f. chapter 5). The interplay of thermal random forces and the intrinsic nonlinearity of the oscillator gives rise to very rich dynamics. Yet, compared to other systems where this effect can become important (i.e. lattice vibrations in a solid state), a vacuum trapped nanoparticle is simple enough that it can be modelled efficiently starting from first principles, thereby making it amenable to rigorous theoretical analysis. Therefore, a vacuum trapped nanoparticle is an ideal testbed to study complex nonlinear dynamics both theoretically and experimentally.

0.2.3 Statistical physics

Due to low coupling to the environment, random forces act on a vacuum trapped particle on timescales much larger than the characteristic timescale of the system (i.e. the oscillation period). However, despite these random forces being small, they still dominate the dynamics of the particle. This insight initiated me to study fluctuation relations in the context of optomechanics. Fluctuation relations are a generalisation of thermodynamics on small scales and have been established as tools to measure thermodynamic quantities in non-equilibrium mesoscopic systems. However, it is paramount to study the theoretical predictions on controlled experiments in order to apply them to more complex systems.
During my PhD, I studied experimentally and theoretically non-equilibrium relaxation of a vacuum trapped nanoparticle between initial and final steady state distributions. In a newly formed collaboration with Prof. Christoph Dellago (University of Vienna, Austria), we showed experimentally and theoretically (c.f. chapter 6) the validity of the fluctuation theorem for relaxation of a non-thermal initial distribution. The same framework allows also to study experimentally non-equilibrium fluctuation theorems for arbitrary steady states and can be extended to investigate quantum fluctuation theorems [Huber et al., 2008] and situations where detailed balance does not

hold [Dykman, 2012].

CHAPTER 1

Experimental Setup

The experimental setup is at the very heart of all experimental results presented in this PhD thesis and its design and development constitute a main part of the PhD work. The purpose of this chapter is to provide guidelines for a researcher interested in reproducing a similar experimental setup.
The setup consists of an optical trap in a vacuum chamber, a loading mechanism, optical detection, feedback electronics and data acquisition. Data acquisition is performed with LabView and will not be detailed in this chapter. The other parts are described in detail in the following sections.

1.1 Optical setup

The optical setup serves two purposes, trapping of a nano-particle with an optical tweezer and detection of the particle motion.
In section 1.1.1 we give a detailed description of the optical setup. Section 1.1.2 gives the mathematical analysis of the detected signal. Sections 1.1.3 and 1.1.4 discuss the differences between measuring the backscattered or the forward scattered light as well as homodyne versus heterodyne detection.

1.1.1 Overview of the optical setup

The optical setup for trapping and cooling is depicted schematically in figure 1.1. The light source is an ultra-stable low noise Nd:YAG laser[1] with an optical wavelength of $\lambda = 1064\,\mathrm{nm}$ (Fig. 1.1). The optical table[2] has active vibration isolation to reduce mechanical noise.

A stable single beam optical trap is formed by focusing the laser ($\sim 80\,\mathrm{mW}$ at focus) with a high NA objective[3] (c.f. chapter 2), which is mounted inside a vacuum chamber. To parametrically actuate the particle, the beam passes through a Pockels cell (EOM)[4] before entering the vacuum chamber. We use parametric actuation to either cool (c.f. chapter 3) or drive the particle (c.f. chapter 4).

For feedback cooling the particle position must be monitored with high precision and high temporal resolution. This is achieved with optical interferometry. The particle position is imprinted into the phase of light scattered by the particle. Through interference of the scattered light with a reference beam, the phase modulation induced by particle motion is converted into an intensity modulation. The intensity modulation is measured with fast balanced photodetectors. We have chosen to measure the forward scattered light. In this configuration, the non-scattered part of the incident beam serves as a reference. Since light scattered in the forward direction and the transmitted beam follow the same optical path, the relative phase between the two is fixed in the absence of particle motion. If the particle moves, the interference of scattered light and transmitted beam causes an intensity modulation of the light propagating in forward direction. We collimate the light propagating in forward direction with an aspheric lens[5] which is mounted on a three dimensional piezo stage[6] for alignment with respect to the objective (Fig. 1.2b).

[1] InnoLight Mephisto 1W
[2] CVI Melles Griot
[3] Nikon LU PLan Fluor 50x, NA = 0.8
[4] Conoptics 350-160 and amplifier M25A
[5] Thorlabs AL1512-C, NA = 0.546
[6] Attocube 2×ANPx101, 1×ANPz101

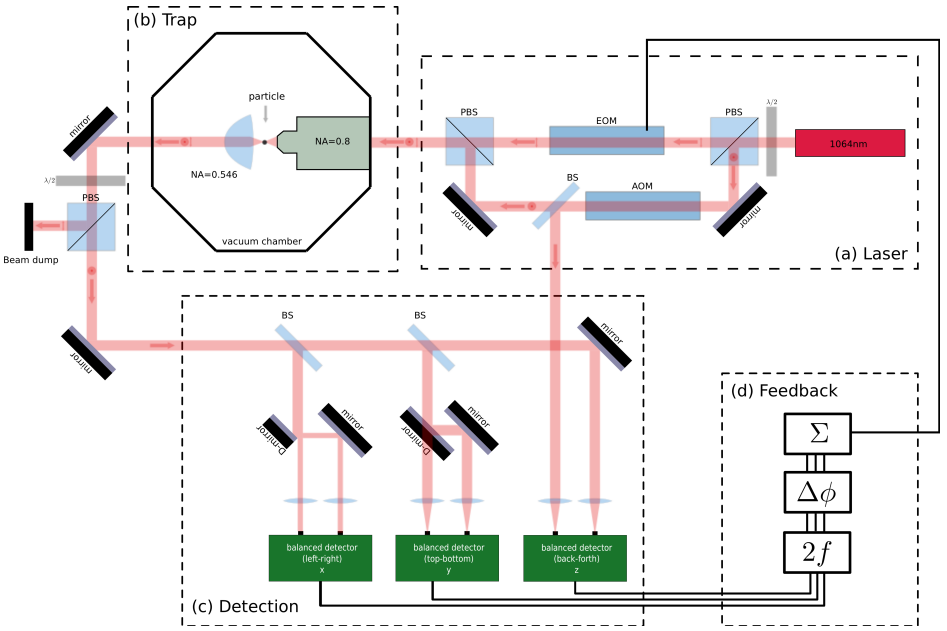

Figure 1.1: **Optical Detection***(a) The beam from the laser source is split in two polarisations. The bulk (horizontally polarised) passes a EOM while the rest (vertically polarised) is frequency shifted by an AOM. Before the vacuum chamber the two beams are recombined with a second PBS. (b) In the chamber the light is focused with a high-NA objective to form a single beam trap. The scattered and the transmitted light are collected with an aspheric lens. (c) After the vacuum chamber the two polarisations are separated. The horizontally polarised part of the beam is dumped. The vertically polarised part of the beam is sent to three balanced photodetectors for detection of particle motion in all three spatial directions. (d) The detector signal is processed by a home-built electronic feedback unit and sent to the EOM.*

To detect particle displacement along the transversal x and y axes, we split the collimated beam with a D-shaped mirror[1] vertically and horizontally, respectively. The two parts of each beam ($\sim 200\,\mu$W each) are sent to the two ports of a fast (80MHz) balanced detector[2]. The signal proportional to z is obtained by balanced detection of the transmitted beam with a constant reference (Fig. 1.1c). Note that the reference beam for the balanced detection in z is not interfered with the beam that carries the signal. The interferometric signal is already contained in the signal beam. Here, the reference beam only cancels the offset. This could also be achieved by a standard photodetector and an electronic high pass filter.

At the detectors, the optical intensity is converted into an electrical signal. This signal is processed by an electronic feedback unit (c.f. section 1.2) and used to drive the EOM which modulates the intensity of the trapping laser to cool the motion of the particle. Since an intensity modulation at the detector resulting from motion of the particle can not easily be distinguished from an intensity modulation due to an applied signal at the EOM, we use an auxiliary beam for detection. The auxiliary beam is obtained by splitting off a small fraction (ratio 1:20) of the original laser beam before it enters the EOM. To avoid interference in the laser focus, the auxiliary beam is cross polarised and frequency shifted by an acusto optic modulator (AOM)[3]. Before the chamber the auxiliary beam is recombined with the trapping beam with a polarising beam splitter (PBS) and separated again after the chamber by another PBS. The trapping beam (horizontal polarisation) is dumped because it contains both the feedback signal and the particle motion. The auxiliary beam (vertical polarisation), which contains only the particle motion, is sent to the photodetectors (Fig. 1.2c). A photograph of the experimental setup is depicted in figure 1.2.

[1] Thorlabs, BBD1-E03
[2] Newport, 1817-FS
[3] Brimrose 410-472-7070, rf-driver AA opto-electronic MODA110-B4-34

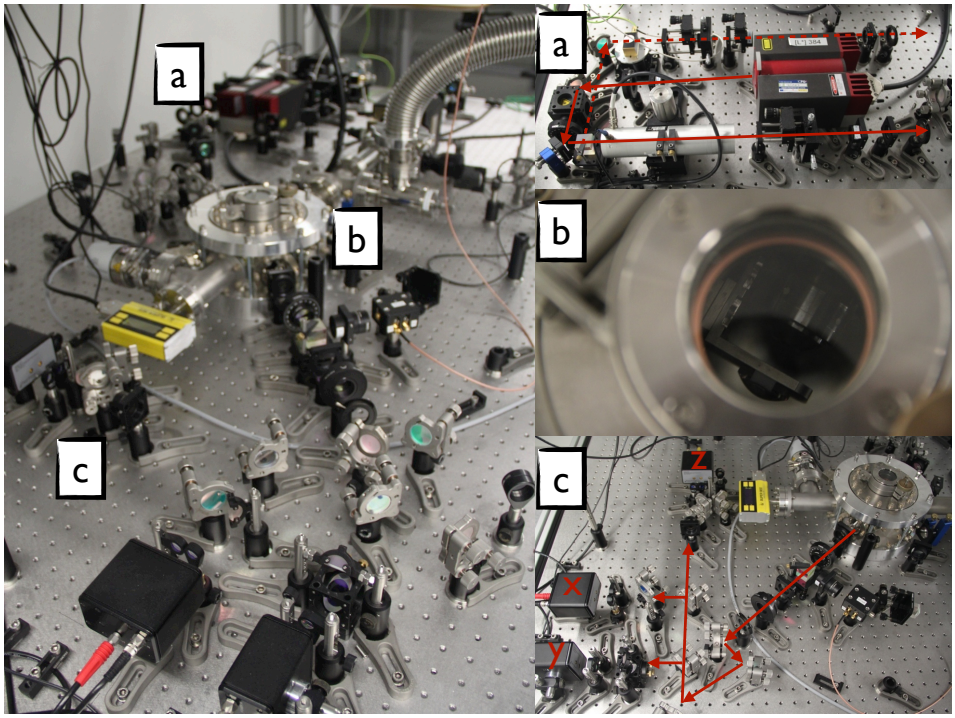

Figure 1.2: **Experimental Setup** *(a) The laser source is split into two polarisations. One (horizontally polarised) is used for trapping and the other (vertically polarised) is used for detection. (b) The high-NA objective is mounted inside the vacuum chamber. The scattered and the transmitted light is collected with an aspheric lens which is mounted on a piezoelectric stage for alignment. (c) The vertically polarised light is sent to three balanced detectors to detect the particle motion is all three spatial directions.*

1.1.2 Detector signal

In this section we look into the formalism of interferometric detection. This helps us to get a better understanding of how particle motion is related to the detected signal.

We consider an incident Gaussian beam polarised along x. The electric field at position $\mathbf{r} = (x, y, z)$ is given by

$$\mathbf{E}_{00}(\mathbf{r}) = E_0 \frac{\mathrm{w}_0}{w(z)} e^{-\frac{\rho^2}{w(z)^2}} e^{i\left(kz - \eta(z) + \frac{k\rho^2}{2R(z)}\right)} \mathbf{n}_x \tag{1.1}$$

with beam waist w_0, Rayleigh range z_0, radial position $\rho = (x^2 + y^2)^{1/2}$, wavevector k electric field at focus E_0 and polarisation vector $\mathbf{n}_x$.
We used the following abbreviations

$$w(z) = \mathrm{w}_0 \sqrt{1 + z^2/z_0^2} \qquad \text{beam radius} \tag{1.2}$$

$$R(z) = z\left(1 + z_0^2/z^2\right) \qquad \text{wavefront radius} \tag{1.3}$$

$$\eta(z) = \arctan\left(z/z_0\right) \qquad \text{phase correction.} \tag{1.4}$$

The incident field excites a dipole moment $\boldsymbol{\mu}_{\mathrm{dp}}\left(\mathbf{r}_{\mathrm{dp}}\right) = \alpha\, \mathbf{E}_{00}\left(\mathbf{r}_{\mathrm{dp}}\right)$ in a particle situated at $\mathbf{r}_{\mathrm{dp}}$ with polarisability α. The induced dipole in turn radiates an electric field

$$\mathbf{E}_{\mathrm{Dipole}}(\mathbf{r}, \mathbf{r}_{\mathrm{dp}}) = \omega^2 \mu_0 \mathbf{G}(\mathbf{r}, \mathbf{r}_{\mathrm{dp}}) \mu_{\mathrm{dp}}, \tag{1.5}$$

where $\mathbf{G}(\mathbf{r}, \mathbf{r}_{\mathrm{dp}})$ is the dyadic Green's function [Novotny and Hecht, 2006] of an electric dipole loacted at $\mathbf{r}_{\mathrm{dp}}$. μ_0 and ω are the vacuum permeability and optical frequency, respectively.

In the paraxial approximation ($z \gg x, y$, hence $z \approx f$), the far field of the dipole at distance f from the focus is a spherical wave

$$\mathbf{E}_{\mathrm{dp}}(\mathbf{r}, \mathbf{r}_{\mathrm{dp}}) = E_{\mathrm{dp}} \exp i(kf + \phi_{\mathrm{dp}}) \mathbf{n}_x \tag{1.6}$$

with amplitude $E_{\mathrm{dp}} \propto 1/f$ and phase ϕ_{dp}, which depend on the particle position. A lens with focal length f transforms the spherical wave into a plane wave with $\mathbf{k} = \mathbf{x}k/f$ (c.f. Fig. 1.3). Here, $\mathbf{x} = (x, y, f)$ is the position on the reference sphere. Hence, the scattered light that arrives at the detector is a plane wave with amplitude

$$E_{\mathrm{dp}} = E_0 \frac{\alpha\omega^2\mu_0}{4\pi f} e^{-\rho_{\mathrm{dp}}^2/{\mathrm{w}_0}^2} \tag{1.7}$$

and phase

$$\begin{aligned} \phi_{\mathrm{dp}} =& -\mathbf{k}\cdot\mathbf{r}_{\mathrm{dp}} + (k - 1/z_0)\, z_{\mathrm{dp}} \\ =& -k_x x_{\mathrm{dp}} - k_y y_{\mathrm{dp}} - k_z z_{\mathrm{dp}} + (k - 1/z_0)\, z_{\mathrm{dp}} \\ \approx& -k_x x_{\mathrm{dp}} - k_y y_{\mathrm{dp}} - k\left(1/kz_0 - \left[k_x^2 + k_y^2\right]/2k^2\right) z_{\mathrm{dp}}, \end{aligned} \tag{1.8}$$

where we used the approximation $k_z \approx k(1 - [k_x^2 + k_y^2]/2k^2)$. For clarity, we dropped the propagation phase $k(f + d)$, where d is the distance between lens and detector. Both the amplitude and the phase depend on the particle position $\mathbf{r}_{\mathrm{dp}}(t)$. But for small displacements of the nano-particle ($|\mathbf{r}_{\mathrm{dp}}| \ll \mathrm{w}_0, z_0$), the dependency of the amplitude is weak. Thus, for the sake of simplicity we assume in the further discussion that the amplitude of the scattered field is constant.

As argued in the previous paragraph, the particle motion is primarily imprinted into the phase of the scattered light. Thus, a phase sensitive measurement is required. Additionally, the scattering cross section $\sigma_s = k^4\alpha^2/6\pi\epsilon_0^2$ is only $258\,\mathrm{nm}^2$ for a $a = 75\,\mathrm{nm}$ SiO_2 particle. This means that the total scattered light intensity is very weak (typically a few μW). To read out the phase and to amplify the signal, the scattered light is interfered with a reference beam field $\mathbf{E}_{\mathrm{ref}}$. As a result, the intensity distribution at the detector is

$$\begin{aligned} I(\mathbf{r}, \mathbf{r}_{\mathrm{dp}}) \propto& |\mathbf{E}_{\mathrm{total}}|^2 = |\mathbf{E}_{\mathrm{dp}} + \mathbf{E}_{\mathrm{ref}}|^2 \\ =& E_{\mathrm{dp}}^2 + 2E_{\mathrm{dp}}E_{\mathrm{ref}}\cos\left(\phi_{\mathrm{dp}}(\mathbf{r}, \mathbf{r}_{\mathrm{dp}}) + \phi_{\mathrm{ref}}\right) + E_{\mathrm{ref}}^2, \end{aligned} \tag{1.9}$$

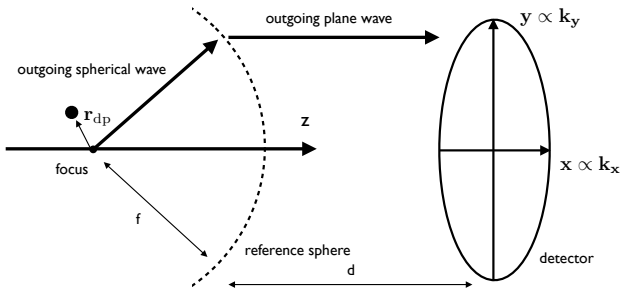

Figure 1.3: **Light collection** *In the far field, light scattered from the particle has the form of a spherical wave. A lens with focal length f maps the spherical wave into a plane wave. Hence, each* **k***-vector is mapped onto a point in the detector plane.*

where ϕ_{ref} depends on the relative phase between the scattered light and the reference. If the intensity of the reference is much larger than the scattered intensity, the first term of the last expression in (1.9) is small compared to the other two and can be neglected.

For detection of the longitudinal displacement z we focus the transmitted beam on one port of a balanced detector. This amounts to integration of (1.9) over the full detector area. Due to the symmetry of $I(\mathbf{r}, \mathbf{r}_{\mathrm{dp}})$, the dependency on x and y vanishes (c.f. Fig. 1.4b). Hence, the detector output only depends on z. To cancel the constant offset E_{ref}^2, we focus a second beam of equal intensity on the second port of the balanced detector. Thus, the detector signal reads:

$$S_z = 2 \int_0^{k_{\max}} \int_0^{2\pi} E_{\mathrm{dp}} E_{\mathrm{ref}} \cos\left(\phi_{\mathrm{dp}}(\mathbf{r}, \mathbf{r}_{\mathrm{dp}}) + \phi_{\mathrm{ref}}\right) \, dk d\phi. \tag{1.10}$$

Here, $k_{\max} = k\,\mathrm{NA}_{\mathrm{det}}$ is the maximum k vector that is detected and which depends on the numerical aperture $\mathrm{NA}_{\mathrm{det}}$ of the collimating lens.

For the detection of the lateral displacement x (y), we split the beam vertically (horizontally) with a D-shaped mirror (c.f. Fig. 1.4a). Each of the two parts is focused onto one of the two ports of a balanced detector. Thus, the detector signal for $x\,(y)$ is given by:

$$S_{x\,(y)} = \int_0^{k_{\max}} \int_{\pi/2\,(0)}^{3\pi/2\,(\pi)} I(\mathbf{r}, \mathbf{r}_{\mathrm{dp}})\, dk d\phi - \int_0^{k_{\max}} \int_{3\pi/2\,(\pi)}^{\pi/2\,(2\pi)} I(\mathbf{r}, \mathbf{r}_{\mathrm{dp}})\, dk d\phi. \tag{1.11}$$

Since the polarisation of the beam is aligned parallel (perpendicular) to the edge of the D-shaped mirror, the symmetry of the beam is conserved. As a consequence, the orthogonal displacement cancels and we measure a signal that only depends on x_{dp} (y_{dp}).

1.1.3 Homodyne measurement

We now consider the situation in which the scattered light interferes with a reference beam at the same optical frequency. This is the situation encountered when analysing the forward scattered light. In that case the reference is simply the non-scattered transmitted beam. Alternatively, we can also analyse the backscattered light. However, in that case, we have to manually set up a reference beam. Under the assumption that the scattered light intensity is much weaker than the reference and that the term E_{ref}^2 can be eliminated by balanced detection, the intensity distribution is given by

$$2E_{\mathrm{dp}}E_{\mathrm{ref}} \cos\left(\phi_{\mathrm{dp}}(\mathbf{r}, \mathbf{r}_{\mathrm{dp}}) + \phi_{\mathrm{ref}}\right). \tag{1.12}$$

To first approximation, the motion of the particle is harmonic, that is $\phi_{\mathrm{dp}} \approx q_0 \cos\Omega_0$ with oscillation amplitude q_0 and angular frequency Ω_0. With the identity

$$e^{ia\cos(b)} = J_0(a) + 2\sum_{k=1}^{\infty} i^k J_k(a) \cos(\mathrm{kb}), \tag{1.13}$$

we find that the spectrum of the detected signal (1.12) consists of harmonics of the particle oscillation frequency Ω_0. The relative strength of the

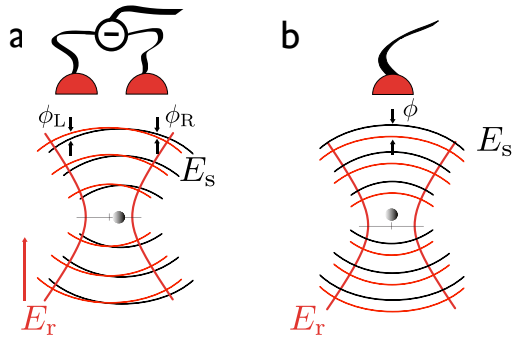

Figure 1.4: **Optical detection of the particle position.** *The total light that propagates towards the detector consists of the transmitted beam (red) and the scattered light (black). The red arrow indicated the direction of beam propagation. (a) To detect lateral displacements, the transmitted light is split and the two resulting beams are detected in differential mode. Because scattered light from the particle travels distances that are different for the two detectors, the accumulated phase at each detector is different. At the detector the scattered light interferes with the unscattered light, which serves as reference beam, making the detector signal sensitive to changes in the phase. Since the phase depends on the position of the particle, the detector signal is proportional to the motion of the particle. (b) To detect the motion along the optical axis, the entire transmitted beam is detected. The total intensity at the detector is the sum of scattered light and transmitted beam. The former has a phase that depends on the particle's position on the optical axis. Due to interference of the two, the detector signal is sensitive to the phase and therefore to the position of the particle. Note that this detection is not dependent on lateral displacement as the phase due to lateral displacements at one half of the detector cancels with the phase at the other half of the detector.*

harmonics is given by Bessel functions J_k and depends on the particle amplitude q_0. For small amplitudes only the first terms contribute significantly.

The homodyne signal (1.12) is the real part of (1.13). If $\phi_{\text{ref}} = -\pi/2$ we get an additional factor i in (1.13). Hence, the main contribution to the signal is $\propto J_1(q_0)\cos\Omega_0 t$. In contrast, if the relative phase is $\phi_{\text{ref}} = 0$, the main contribution is $\propto J_2(q_0)\cos 2\Omega_0 t$. Therefore, to get a detector signal that is a linear function of the particle displacement, the relative phase ϕ_{ref} has to be fixed to $-\pi/2$.
Note that, if the phase is fixed to 0, the detector signal is $\propto \cos 2\Omega_0 t$. This is the signal required for feedback cooling. Hence, if we can interfere the scattered light with a reference that is in-phase, we can circumvent an electronic frequency doubler (c.f. section 1.2).

Forward detection

In forward detection the reference beam is the non-scattered transmitted beam. In the paraxial approximation, the far-field of the transmitted Gaussian is a spherical wave

$$\mathbf{E}_{\text{ref}}(\mathbf{r}) = E_{\text{ref}} \exp i(kR - \pi/2)\mathbf{n}_x, \tag{1.14}$$

with amplitude $E_{\text{ref}} \approx E_0 z_0/R$ and phase $-\pi/2$, known as the Gouy phase shift. The spherical wave is collected by a lens and propagates as a plane wave to the detector. Since the transmitted beam and the forward scattered light follow the same optical path, they acquire the same propagation phase. Hence, the phase difference at the detector is given by the Gouy phase shift $\phi_{\text{ref}} = -\pi/2$ and the detector signal is linear with respect to particle position.

Note that in forward scattering the scattered light and the reference are both proportional to the incident laser $E_{\text{dp}} \propto E_{\text{ref}} \propto E_0$. As a consequence, if the trapping laser is used for detection, the intensity of the reference (the last term of (1.9)) is time dependent because of the feedback signal. If the detectors are not 100% balanced, they will pickup the intensity modulation and feed it back into the feedback circuit. This results in undesired back-action. To resolve this problem, we chose to split off a part of the incident beam before it is modulated as explained in section 1.1.1. But it also means

that we do not use the scattered light from the trapping beam, which is much more intense than the scattered light from the auxiliary beam. Hence, the sensitivity is not as high as it potentially could be if we could use the scattered light from the trapping beam.

Backward detection

In backward detection we use the same lens for collection as for focusing of the light. The collected light is interfered with an independent reference. This gives us the freedom to choose the strength of the reference field freely and to optimise it to get the best signal-to-noise ratio (SNR). The light scattered back into the objective is of the same form as the forward scattered light of equation (1.6) because the dipole radiation pattern is symmetric. Hence, the detector signal is given by (1.12). However, since the reference beam and backscattered light do not follow the same optical path, the relative phase of reference and backscattered light ϕ_{ref} is not fixed anymore. It depends on the relative path difference and is therefore subject to any noise source that alters the optical path length, for example air currents and mechanical drift of the optical elements.

1.1.4 Heterodyne measurement

Measuring in back-reflection not only allows us to choose the intensity of the reference field but also it's frequency. If the optical frequency of the reference differs from that of the scattered light, it is called a heterodyne measurement. The detector signal is then given by

$$2E_{\mathrm{dp}}E_{\mathrm{ref}}\cos\left(\phi_{\mathrm{dp}}(\mathbf{r},\mathbf{r}_{\mathrm{dp}})+\phi_{\mathrm{ref}}+\Delta\omega t\right), \tag{1.15}$$

where $\Delta\omega$ is the difference in optical frequency. For $\Delta\omega = 0$ (1.15) reduces to (1.12). The spectrum of the detector signal is now shifted to $\Delta\omega$ with sidebands at $\Delta\omega \pm \Omega_0$. In order to benefit from a lower noise floor at high frequencies, one would typically choose $\Delta\omega \gg \Omega_0$. With a lock-in amplifier that locks to the modulation frequency $\Delta\omega$ one can measure both

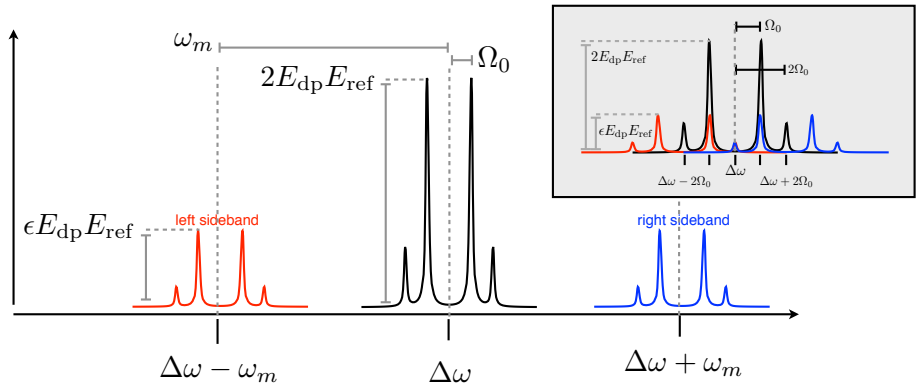

Figure 1.5: **Spectrum of detector signal.** *In the heterodyne measurement the spectrum is shifted to $\Delta\omega$. The particle oscillation shows up as side-peaks around $\Delta\omega$ at harmonics of the particle oscillation frequency Ω_0 (black). A modulation of the intensity at ω_m reproduces the main structure at side-frequencies $\Delta\omega \pm \omega_m$ (red and blue). The feedback modulates the intensity of the laser at $\omega_m = 2\Omega_0$. As a consequence, the sidebands overlap with the main peaks (see inset). However, since the phase of the intensity modulation is fixed to the particle oscillation, this results only in a constant phase offset, which is eliminated by the lock-in.*

quadratures of (1.13) and extract, therefore, the phase $\phi_{\mathrm{dp}} + \phi_{\mathrm{ref}}$. To get rid of the low frequency spurious phase ϕ_{ref}, the lock-in amplifier output has to be high-pass filtered.

Note that the bandwidth B of the lock-in has to be large enough so that the signal from the particle passes, that is $B \gg \Omega_0$. This requirement is quite demanding, given that typical particle frequencies are of the order of 100kHz-1Mhz. For an ideal harmonic oscillator, the damping Γ_0 determines the timescale on which the energy and the phase change. Thus, the minimum required bandwidth for an harmonic oscillator is of the order Γ_0, which is a factor $Q \sim 10^8$ less than Ω_0. However, since for efficient feedback cooling the phase stability is paramount, a higher bandwidth might be

necessary (still $\ll \Omega_0$) if there are additional sources of phase noise such as frequency fluctuations due to nonlinear amplitude to frequency conversion (c.f. chapter 5). A detection scheme with a bandwidth $B \sim \Gamma_0 \ll \Omega_0$ could be realized for instance with a phase locked loop (PLL), where the particle itself acts as the frequency determining element.

Detection with the trapping laser

As mentioned before, we would get a much stronger signal if we could use the scattered light from the trapping laser. Let's assume the trapping laser is modulated at frequency ω_m and modulation depth ϵ. The scattered field is $\sim E_\mathrm{dp}(1+\epsilon\cos\omega_m t)$. Hence, the spectrum of the detector signal exhibits sidebands at the modulation frequency ω_m and amplitude $\propto \epsilon E_\mathrm{dp}E_\mathrm{ref}$ as shown in figure 1.5. However, for small modulation ϵ the amplitude of the main signal $\propto E_\mathrm{dp}E_\mathrm{ref}$ is much stronger than the sidebands.

If the trapping laser is used for detection, the intensity modulation is at $\omega_m = 2\Omega_0$. Therefore, the sidebands from the intensity modulation overlap with the main signal. But, since the feedback fixes the phase of the sideband to the main signal, this results only in a constant phase, which is eliminated by lock-in detection.

1.2 Feedback Electronics

For feedback cooling of the particle's center of mass (CoM) motion we use an analog electronic feedback signal. The signal is used to modulate the intensity of the trapping laser with an EOM.
Figure 1.6 shows the electronic feedback system. It consists of five units: a bandpass filter, a variable amplifier, a phase shifter, a frequency doubler and an adder. The first four units are replicas of the same electronic circuit, each one optimised for one specific frequency. The frequencies correspond to the three oscillation frequencies of the vacuum trapped particle. Table 1.1 shows the feedback parameters for the three axes. The fifth unit adds

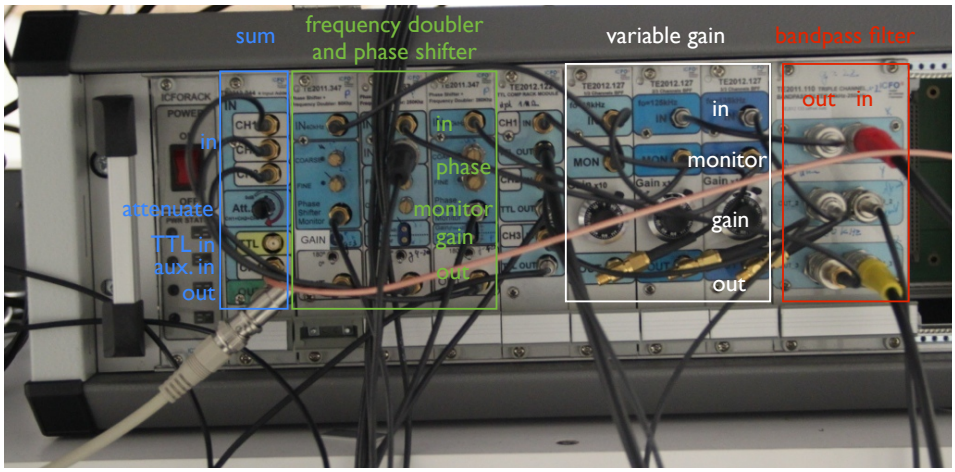

Figure 1.6: *The* **Feedback Electronics** *consist of of five modules. A bandpass filter (red), variable gain (white), frequency doubler (green), phase shifter (same module, also green) and adder.*

the three signals together and sends the resulting signal to the EOM.

The following sections describe the functionality of each of the individual modules.

1.2.1 Bandpass filter

The signal of interest is at the natural frequency of the particle. However, there are low frequency components because of mechanical drift and beam pointing instability. Furthermore, the auxiliary beam and the part of the trapping beam that leaks through the polarising beam splitter interfere at the detector and create a high frequency beating at the AOM frequency. The unwanted frequency components can have a detrimental effect on the output signal because each electronic circuit has a maximum range of input voltages before it saturates. Since the peak values at the unwanted frequencies exceed

	axes		
parameters	x	y	z
f_0 [kHz]	125	140	38
$\phi(f_0)$ [°]	12	149	159
BW [kHz]	15-250	15-250	15-150

Table 1.1: **Parameters of electronic feedback.** *Each stage of the electronic circuit is optimised for one specific particle frequency. f_0 is the frequency of the frequency doubler. ϕ is the phase difference between a sinusoidal input at the bandpass filter and the frequency doubled output at the adder. BW is the bandwidth of the bandpass filter. All subsequent modules have a higher cut-off frequency.*

the peak values at the signal frequency, it is necessary to filter them at an early stage of the feedback circuit. Therefore, each of the three signals from the balanced photodetectors is filtered by a second order bandpass filter[1]. Because every electronic circuit adds noise, the detector signals are also amplified at this first stage of the feedback by a factor $\times 20$. This mitigates the noise contribution from subsequent stages of the feedback and thereby gives a better SNR at the output of the feedback circuit.

1.2.2 Variable gain amplifier

To get the optimum SNR at the end of the feedback circuit, it is important amplify the signal enough to mitigate subsequent additive noise, but not too much to saturate any of the circuits. Therefore, to tune to the optimum gain, the bandpass is followed by a variable gain amplifier[2] from $\times 1$ to $\times 10$ that is controlled with a potentiometer.

[1] multiple feedback, AD817
[2] OPA1611AID

1.2.3 Phase shifter

As shown in figure 1.7, the optical power P has to be larger than the average power P_0 when the particle moves away from the trap center and smaller if the particle comes closer. Thus, the feedback signal has to be exactly in phase ($\phi = 0$) with respect to the particle oscillation to achieve cooling. Since every stage (detector, electronics, electro-optic modulator) adds some

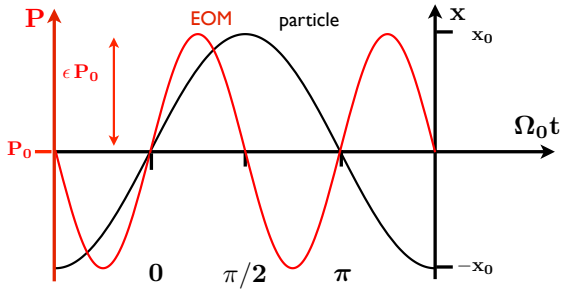

Figure 1.7: **Feedback Phase** *To achieve cooling, the modulation of the EOM has to be exactly in phase $\phi = 0$ with respect to the particle oscillation. The modulation depth ϵ depends on the feedback gain.*

phase to the feedback signal, the phase of the electronic signal has to be tuned to the right value. This is achieved with a two stage phase shifter, as a single stage would not be able to cover the full range of 180°. Further, it allows us to have one control for coarse and one for fine tuning. The phase shifter is essentially a bandpass filter with unitary gain where the center frequency can be tuned by a potentiometer. Thus, the phase response of that filter is not flat but has a slope that depends on the value of the potentiometer. The operational amplifier used was AD8671ARZ.

1.2.4 Frequency doubler

The frequency doubler is integrated in the same module as the phase shifter. To create a signal at twice the frequency of the input signal, we use a com-

mercial multiplier circuit[1]. For an input signal $X_{\text{in}} = X_0 \sin \omega t$, the resulting signal is $X_{\text{out}} = X_0^2 \omega \cos 2\omega t \,/(10V)$. Hence, the device is optimised for a single frequency where an input amplitude of $10V$ gives and output also at $10V$.

1.2.5 Adder

To cool the particle in all three spatial dimensions, we sum the three processed signals together[2] and send it to the EOM. The summed signal can be switched off through a TTL signal by an analog switch[3]. This feature is used in the relaxation experiment of chapter 6. Additionally, there is an extra input that is added to the output. This is needed in chapter 4 to drive and cool the particle simultaneously.

1.3 Particle Loading

Loading a particle into the optical trap is a critical first step. In a liquid particles can be captured easily. By moving the chamber that contains the liquid with a translation stage, the suspended particles are dragged along and can thereby be brought into close vicinity of the trapping laser. In contrast, particles in a gas will quickly fall down due to gravity.

The size of the optical trap is of the order of the focal volume $\sim \lambda^3$. Therefore, a particle that passes the focus at a distance larger than $\sim \lambda$ will not be captured. Furthermore, if a particle enters the volume at high speed, the low damping in vacuum will not slow the particle down sufficiently. The maximum allowed speed is $v_{\text{max}} \sim \lambda \Gamma_0$, where Γ_0 is the damping constant. In water Γ_0 is given by Stokes formula $\Gamma_0 = 6\pi\eta a/m$, where a and m are the radius and mass of the particle and η the viscosity of the surrounding medium. In water $\eta^{(\text{water})} = 890\,\mu Pa\,s$. Hence, the maximum velocity for a

[1] AD734/AD
[2] AD817
[3] NC7SB3157P6X

$a = 75$nm SiO_2 particle is $v_{\max}^{(\text{water})} = 344\,\text{m/s}$. In air the viscosity is about two orders of magnitude smaller $\eta^{(\text{air})} = 18\,\mu\text{Pa s}$. Hence, the particle velocity should not exceed $v_{\max}^{(\text{air})} = 7\,\text{m/s}$. The challenge lies, therefore, in finding a technique by which a slow single nano-particle is brought into the focal volume.

One strategy to bring a nano-particle into the focal volume in a controlled manner, is to place it onto a substrate, which can be manipulated with high accuracy by piezo-electric actuators. However, a particle on a substrate remains there due to dipole-dipole interactions known as van der Waals (VdW)-forces. The VdW-force in the "DMT limit" of the Derjaguin-Muller-Toporov theory is given by [Israelachvili]

$$F_{\text{VdW}} = 4\pi a\gamma, \tag{1.16}$$

where a is the radius of the particle and γ is the effective surface energy. Measurements on silica spheres on glass give $F_{\text{VdW}} = 176\,\text{nN}$ for $a = 1\,\mu\text{m}$ [Heim et al., 1999]. For comparison, the gravitational force for a particle of this size is only $\sim 0.1\,\text{pN}$ and therefore much too weak to remove the particle.

Sections 1.3.1 and 1.3.2 discuss two approaches that aim at removing nano-particles form a surface, pulsed optical forces and inertial forces. Both are found to be insufficient to overcome the forces that keep the particle on the surface. Section 1.3.3 gives a detailed description of the successfull nebuliser approach. The nebuliser creates an aerosol of nano-particles, which are then trapped by the optical tweezer.

1.3.1 Pulsed optical forces

The maximum force from a typical continuous wave optical tweezer ($\sim 1\,\text{nN}$) is two to three orders of magnitude weaker than the VdW-force. The optical force depends linearly on the optical power. A pulsed laser can have a peak power much higher than a continuous wave laser (CW-laser). Therefore, it was suggested in [Ambardekar and Li, 2005] that a pulsed laser should have

a maximum force strong enough to overcome the VdW-force. Generally, the shorter the pulse the higher the maximum peak power that can be achieved. However, the force has to bring the particle at least to a critical distance d_{crit}, so that the VdW-force doesn't pull the particle back to the surface once the pulse ends. Hence, assuming a constant acceleration throughout the pulse, the minimum pulse duration is $\tau_{\mathrm{pulse}} = (2d_{\mathrm{crit}}m/F_{\mathrm{pulse}})^{1/2}$.

We used a Nd:YAG laser with a pulse duration of $\sim 50\,ns$ and a total energy per pulse of $\sim 0.1\,mJ$ at the sample. Thus, the maximum power ($\sim$ 2kW) is three orders of magnitude higher than what can be achieved with a CW-laser. Indeed, we managed to remove several silica particles from a glass coverslip that was coated with a thin film ($\sim 20nm$) of either aluminium or gold. However, the laser pulse often left a crater behind. This suggests that actually thermal forces due to light absorption in the metal film removed the particle. Some of the released particles disappeared from the field of view and some landed a few μm away from their initial position. Still, we did not manage to trap any of the released particles with a second superimposed CW laser and decided to pursue other approaches. In retrospective, this is not too surprising. To trap a particle, we do not only have to remove it, but also shoot it close to the optical trap with not too much kinetic energy. From the above discussion about the trap volume and the required particle speed, it is clear that the probability of catching a particle is rather small.

1.3.2 Piezo approach

Already Ashkin in his pioneering experiments [Ashkin, 1971] used a piezoelectric transducer to overcome the VdW-forces. This method was also used to trap and cool microspheres to mK temperatures [Li et al., 2011] and is described in detail in reference [Li, 2011]. For a sinusoidally driven piezo with oscillation amplitude q_{p} and frequency ω_{p}, the force due to the particle's inertia is

$$F_{\mathrm{piezo}} = m\omega_{\mathrm{p}}^2 q_{\mathrm{p}}, \tag{1.17}$$

where m is the mass of the particle. Consequently, the acceleration needed to release the particle is

$$a_{\mathrm{p}} = \omega_{\mathrm{p}}^2 q_{\mathrm{p}} = 4\pi a\gamma/m \propto a^{-2}. \tag{1.18}$$

Hence, for a given maximum acceleration the piezo can provide, there is a minimum particle size that can be shaken off. For typical values this is $a_{\mathrm{min}} \sim 1\mu m$. Therefore, this approach can not be used to shake nanoparticles off a substrate.

1.3.3 Nebuliser

From the preceding sections it is clear that optical, gravitational and inertial forces are too weak to remove a particle from a substrate. In this section we describe a surprisingly simple but functional approach to load the trap with nanoparticles [Summers et al., 2008]. We use a commercial nebuliser[1] and a highly diluted solution of silica beads[2] of 147 nm diameter. The diluted solution is obtained from mixing $10\mu l$ initial solution (50 mg/ml) with $\sim 1ml$ of ethanol. The nebuliser consists essentially of a mesh on top of a piezo element. A little bit of liquid is brought into the space between the piezo and the mesh. The motion of the piezo pushes the liquid through the mesh. The mesh breaks the liquid into little droplets of diameter smaller than $2\,\mu m$. Under standard humidity conditions, the droplets quickly evaporate and only the solid component is left behind. The concentration of the solution is such that on average there is one or no particles in a single droplet. As shown in figure 1.8, we use a nozzle in an upside down configuration to funnel the falling particles close to the laser focus. Through a viewport on the side of the vacuum chamber we observe the falling particles with a CCD camera[3] and wait until one is trapped. Then we remove the nozzle, close the chamber and pump down. Note that because the light scattered by the particle has a dipole radiation pattern the polarisation of the laser beam

[1] Omron NE-U22-W
[2] Microparticles SIO2-R-B1181
[3] Hamamatsu C8484-05G01

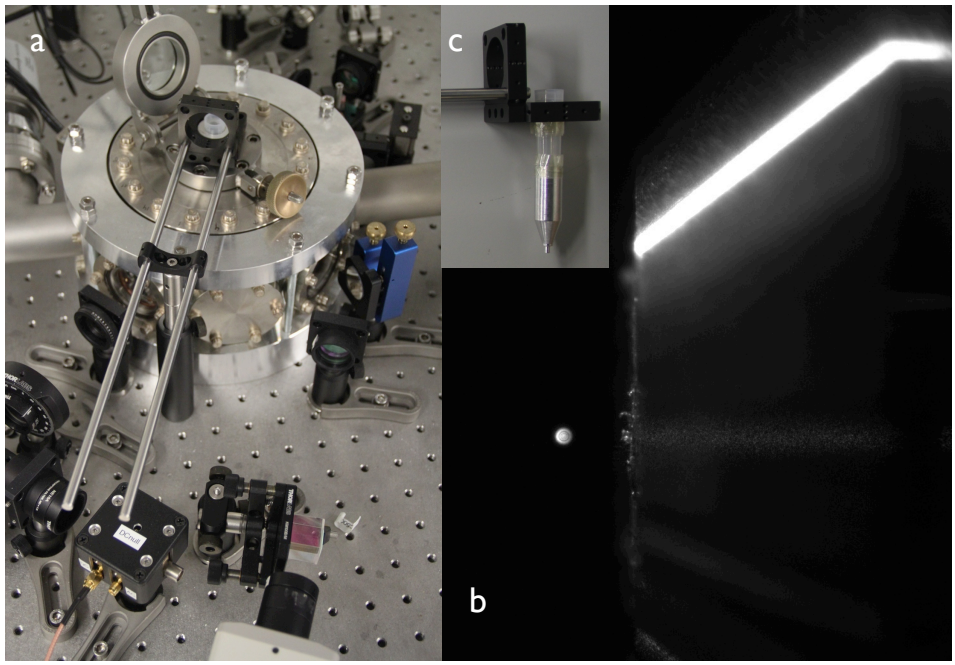

Figure 1.8: **Particle loading**. *The particle is loaded by spraying a solution of nano-particles through a nozzle which is placed above the focus. (a) Positioning of the nozzle in the vacuum chamber. (b) Trapped particle imaged with a CCD camera from the side. (c) Nozzle to funnel the falling particles towards the focus of the trapping laser.*

should be orthogonal to the direction of observation to see the particle with the camera.

1.4 Vacuum system

Figure 1.9 shows the vacuum system. Close to the main chamber there are two gauges to measure the pressure as close to the particle as possible.

One is a convection gauge[1] which can be read with the computer and that covers the range $1.3 \times 10^3 - 10^{-4}$ mBar. The other one is a combined Pirani and cold cathode gauge[2] which can be read off at the display of the pump station and that covers $10^2 - 5 \times 10^{-9}$ mBar.
The chamber is evacuated in a first stage with a membrane pump[3] and later with a turbo-molecular pump[4]. Both are integrated in a pump station[5].
Between the chamber and the pumps is an all-metal valve[6] that can be closed to disconnect the pump from the chamber. The valve is also used to evacuate the chamber adiabatically from $\sim 1\,$mBar down to $\sim 10^{-3}\,$mBar, which is a regime of high particle losses in the absence of feedback cooling. In that case, the valve is closed, while the pump is still running. As a result, a pressure difference builds up between the chamber and the pump. When the pump is at a lower pressure than the main chamber, the rate at which the pressure in the main chamber decreases can be controlled with the valve. The minimum pressure we can achieve with the pump station is $\sim 10^{-6}\,$mBar.

1.4.1 Towards ultra-high vacuum

To go to lower pressure, we have an ion pump installed. The ion pump can achieve ultra high vacuum below $10^{-10}\,$mBar. However, to reach such extreme values, the chamber has to be kept clean with high diligence and baked to temperatures of $\sim 300°$. This is currently not compatible with our loading mechanism because the chamber has to be opened to load a particle. Thus, even with the ion pump we can not improve the vacuum. To achieve, ultrahigh vacuum we are implementing a load-lock. The load-lock consists of two chambers and a translation stage. In the loading chamber, a particle is trapped and brought to high vacuum ($10^{-6}\,$mBar). The transfer system

[1] CVM-201 "Super bee", InstruTec
[2] PKR 251, Pfeiffer vacuum
[3] MVP 015-2, Pfeiffer vacuum
[4] TMH 071, Pfeiffer vacuum
[5] TSH 071E, Pfeiffer vacuum
[6] Hositrad technology

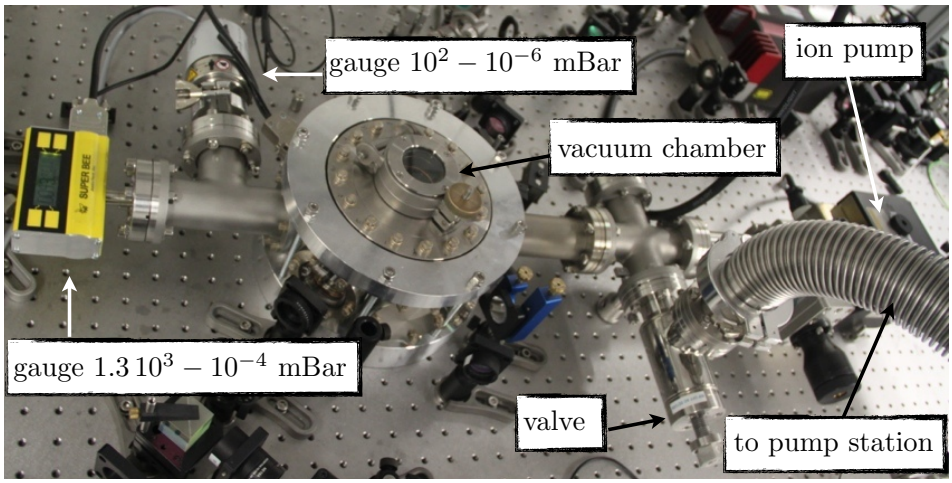

Figure 1.9: *The* **Vacuum System** *consists of a vacuum chamber, with two gauges, that cover pressure ranges from* $1.3\times10^3-10^{-3}$ *mBar and* 10^3-10^{-6} *mBar, respectively. The chamber is connected to a pump station and an ion pump.*

translates the trapped particle under high vacuum into the main chamber. After the particle has been loaded into the main chamber, the main chamber is disconnected from the rest of the vacuum system and pumped down to ultra high vacuum. Hence, the main chamber will always be under a high vacuum and it is possible to pump down to ultra high vacuum with the ion pump.

1.5 Conclusion

In this chapter we presented the technical details of an experimental setup which allows for trapping, cooling and parametrically driving of nanoparticles in high vacuum. This is a major step towards employing trapped nano-particles for ultra-sensitive detection and ground state cooling. How-

ever, to exploit the full capabilities of the system, improved detection and higher vacuum are required.
An improved detection can be achieved by several means. One way is to detect the scattered light of the trapping beam by heterodyne interferometry as discussed in section 1.1.4. An alternative way is to place the particle inside a high finesse cavity. The cavity modes are very sensitive to changes in optical path length. The optical path length depends on the particle position inside the cavity. Therefore, light which is transmitted though or reflected from the cavity becomes highly correlated with the particle motion. Since the light inside the cavity also exerts a force on the particle, a cavity can not only be used as a detector but also to cool the particle motion [Chang et al., 2010; Romero-Isart et al., 2010; Kiesel et al., 2013].
Better vacuum requires that the vacuum chamber is always kept under high vacuum. This is incompatible with our current loading technique, which requires operation at ambient pressure. To reconcile the two requirements we are currently developing a load-lock.

CHAPTER 2

Theory of Optical Tweezers

To understand the working principle of optical tweezers, we have to understand the forces exerted by electromagnetic fields. To this end we discuss a simple analytical model based on the Rayleigh approximation and a Gaussian description of the trapping laser.

2.1 Introduction

The optical force has two components, the gradient force and the scattering force. The former points toward the region of highest intensity and, therefore, allows for stable trapping in the focus of a laser beam. The latter points in the direction of beam propagation and therefore pushes the particle out of the trap. Thus, to achieve a stable trap, the scattering force has to be eliminated or the gradient force has to overcome the scattering force. The scattering force can be cancelled by two counter propagating beams. However, the two beams have to be well aligned and symmetric in shape and power [Ashkin, 1970]. Instead of a second independent beam one can also use the back-reflection from a mirror to form a standing wave [Zemánek et al., 1998, 1999]. The scattering force of a single beam can also be compen-

sated by any other force, for example as in Ashkin's pioneering experiments [Ashkin, 1971], by gravity. However, alignment inaccuracies tend to make all these configurations unstable. If the scattering force is not cancelled, the gradient force has to dominate over the scattering force to achieve stable trapping. This configuration requires a tightly focused laser beam [Ashkin et al., 1986] and is known as optical tweezer. The conditions under which a sub-wavelength particle can be trapped with an optical laser tweezer is discussed in this chapter.

2.2 Optical fields of a tightly focused beam

For a stable single beam optical trap it is necessary to tightly focus the optical field. In this section we discuss, therefore, some of the properties of optical fields focused with a high numerical aperture objective. For a detailed treatment see reference [Novotny and Hecht, 2006].

As depicted in figure 2.1, the field incident on the refractive element (lens or objective) is treated as a bundle of light rays [Wolf, 1959; Richards and Wolf, 1959]. Each ray represents a plane wave propagating along z. The refractive element maps the incident field onto a reference sphere of radius f. From the reference sphere, the plane waves propagate towards the focus, which lies at the center of the reference sphere. The wave vector $\mathbf{k}$ of the transformed plane waves depends on the position where the incident ray hits the reference sphere.

Interference of all the plane waves at the focus creates a field distribution that can be expressed in the angular spectrum representation [Novotny and Hecht, 2006]:

$$\mathbf{E}(\rho,\varphi,z) = \frac{ikfe^{-ikf}}{2\pi}\int_0^{\theta_{\max}}\int_0^{2\pi}\mathbf{E}_\infty(\theta,\phi)e^{ikz\cos\theta}e^{ik\rho\sin\theta\cos(\phi-\varphi)}\sin\theta d\phi\theta, \tag{2.1}$$

where $\mathbf{E}_\infty(\theta,\phi)$ is the field distribution on the reference sphere, f the focal length and $k = \lambda/2\pi$ the wave vector. The maximum angle $\theta_{\max}$ depends on the numerical aperture (NA) of the lens $\mathrm{NA} = n_m \sin\theta_{\max}$, where n_m is

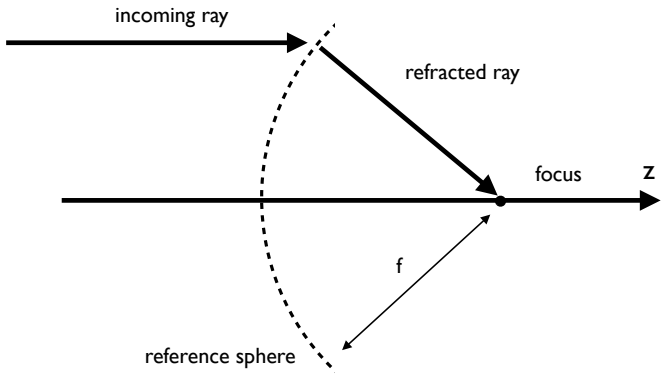

Figure 2.1: **Focusing of the optical field.** *An incoming ray is refracted at a lens with focal length f. The wave vector of the refracted ray is determined by the position where the incident ray hits a reference sphere with radius f*

the refractive index of the surrounding medium. The above integral is also known as the Debye integral.

For lenses with high NA, wave vectors with high angles are involved in the construction of the field at the focus. As a consequence, new polarisations are generated and the field distribution is slightly elongated along the direction of polarisation $\mathbf{n}_x$ of the incident field [Novotny and Hecht, 2006]. Even for a high NA lens the aperture of the lens is finite. Hence, field components with very high spatial frequencies are cut-off. Therefore, the field is defracted and the spatial profile of the focus has oscillatory side-lobes (c.f. Fig. 2.2).

In the limit of weak focusing and neglecting the finite size of the aperture, the above integral (2.1) can be solved analytically. For an incident Gaussian beam we obtain the familiar paraxial expression [Novotny and Hecht, 2006]

$$\mathbf{E}(\rho, z) = E_0 \left[1 + (z/z_0)^2\right]^{-1/2} e^{-\frac{\rho^2}{w^2(z)} + i\phi(z,\rho)} \mathbf{n}_x, \tag{2.2}$$

where $\mathbf{n}_x$ is the direction of polarisation, w_0 is the beam waist and E_0 the electrical field at the focus. For clarity, we have defined the following quantities

$$w(z) = \mathrm{w}_0 \sqrt{1 + z^2/z_0^2} \qquad \text{beam radius} \tag{2.3}$$

$$\phi(z, \rho) = kz - \eta(z) + k\rho^2 / 2R(z) \qquad \text{phase} \tag{2.4}$$

$$R(z) = z \left(1 + z_0^2/z^2\right) \qquad \text{wavefront radius} \tag{2.5}$$

$$\eta(z) = \arctan\left(z/z_0\right) \qquad \text{phase correction.} \tag{2.6}$$

The gradual phase shift $\eta(z)$ as the beam propagates through the focus is known as the Gouy phase shift.

Despite the strong approximations that lead to equation (2.2), the exact intensity distribution even for a tightly focused beam is very similar to that of a Gaussian beam. However, the Rayleigh range and focal width are no longer given by the simple paraxial expressions $z_0 = {\mathrm{w}_0}^2/2$ and $\mathrm{w}_0 = 2/k\theta_{\max}$, respectively. Instead, they are free parameters that are obtained by a fit to the exact solution (2.1) (see Table 2.1). Thus, the analytical expression of the focal field is given by a slightly modified equation (2.2):

$$\mathbf{E}(\rho, z) = E_0 \left[1 + (z/z_0)^2\right]^{-1/2} e^{-\left(\frac{x^2}{\mathrm{w}_x^2(z)} + \frac{y^2}{\mathrm{w}_y^2(z)}\right) + i\phi(z,\rho)} \mathbf{n}_x, \tag{2.7}$$

where the separate beam waists w_x and w_y account for the asymmetry of the focus along x and y, respectively. Note that in this model, the asymmetry of the focus is only accounted for in the amplitude but not in the phase.

Figure 2.2 shows the field distribution in the focal planes. The first row shows the intensity distribution calculated with the Debye integral (2.1) in the x-z and x-y plane, respectively. For comparison, the bottom row

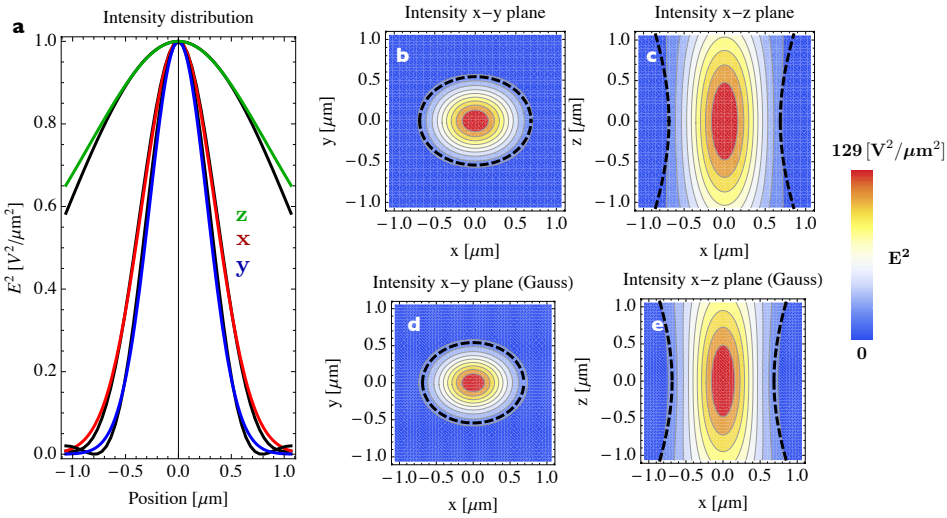

Figure 2.2: **Intensity distribution of tightly focused optical fields.** *(a) The intensity distribution computed with the Debye integral* (2.1) *is shown as black lines for the three mayor axes. The coloured lines are fits to the Gaussian model* (2.2)*. The exact solution exhibits side lobes as a consequence of diffraction. Both models take the asymmetry of the focal spot into account. (b,c) The intensity distribution computed with the Debye integral in the x-y plane and y-z plane, respectively. (d,e) The same fields computed with the Gaussian model. In the calculation we assumed focusing in air with a NA= 0.8 objective, a filling factor (ratio between beam waist of incident beam and lens aperture) of 2 and wavelength* $\lambda = 1064$nm*. For a detailed description of how to apply equation* (2.1) *see reference [Novotny and Hecht, 2006].*

shows the same distributions obtained with the Gaussian model (2.7). The Gaussian model does not include diffraction and therefore doesn't have side-lobes. However, up to $\lambda/2$ away from the center, the Gaussian model fits the exact solution well.

	Beam parameter	Paraxial approx.
w_x	687 nm	423 nm
w_y	542 nm	423 nm
z_0	1362 nm	529 nm

Table 2.1: **Beam parameters** *for the computation of the field at the focus. The parameters are obtained from a fit to the exact numerical solution. For comparison, the right column shows the parameters obtained with the paraxial approximation.*

2.3 Forces in the Gaussian approximation

From the optical field we will now calculate the optical forces. Generally, these forces are summarised by the Maxwell stress tensor [Novotny and Hecht, 2006]

$$\mathbf{F} = \int_{\partial V} \overleftrightarrow{\mathbf{T}} \cdot \mathbf{n}(\mathbf{r}) da, \tag{2.8}$$

which is a derivation of the conservation laws of electromagnetic energy and momentum. Remarkably, the Maxwell stress tensor and therefore the optical forces are entirely determined by the electromagnetic fields at the surface of the object. That is, all the information is contained in the electromagnetic fields and no material properties enter in (2.8). To calculate $\overleftrightarrow{\mathbf{T}}$, the self-consistent fields are needed. Generally, this is a non-trivial task because the presence of the object changes the incident field. Hence, if the body deforms, the boundary conditions in (2.8) change. Consequently, the material properties enter the problem through the changed boundary conditions. However, in the following we will assume that the body is rigid. Even under the assumption that the body is rigid, evaluation of (2.8) is generally computationally expensive. Furthermore, equation (2.8) has to be evaluated for each particle position. Thus, for practical purposes it is desirable to have a closed-form expression or a numerically efficient approximation of

the integral (2.8) [Rohrbach and Stelzer, 2001].

For a spherical object of arbitrary size, Mie-theory provides an exact analytical solution [Van De Hulst, 1981] in form of an infinite series of multipoles [Neto and Nussenzveig, 2000]. The bigger the sphere, the more multipoles have to be taken into account. Forces on large dielectric spheres ($a \gg \lambda$) can be calculated by ray-optics [Ashkin, 1992]. The ray-optics calculation uses Snells law and the Fresnel formulas. If the particle is small compared to the wavelength of the incident radiation (Rayleigh limit $a \ll \lambda$), the only significant contribution comes from the electric dipole term.

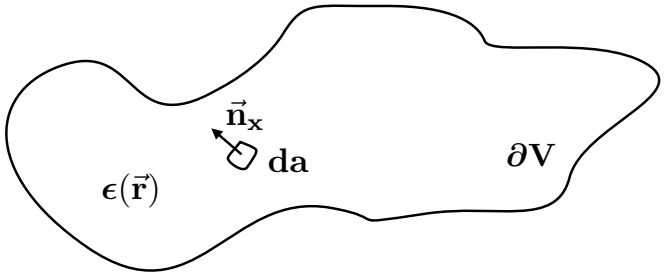

Figure 2.3: **Dielectric body** *The optical forces are determined by the total electromagnetic fields at the surface ∂V of the object.*

2.3.1 Derivation of optical forces

It is instructive to write the optical force as a sum of two terms, the gradient force $\mathbf{F}_{\text{grad}}(\mathbf{r})$ and the scattering force $\mathbf{F}_{\text{scatt}}(\mathbf{r})$ [Novotny and Hecht, 2006; Rohrbach and Stelzer, 2001]:

$$\mathbf{F}(\mathbf{r}) = \mathbf{F}_{\text{grad}}(\mathbf{r}) + \mathbf{F}_{\text{scatt}}(\mathbf{r}). \tag{2.9}$$

Under the assumption that we can represent the complex amplitude of the electric field in terms of a real amplitude E_0 and phase ϕ, the forces are given by

$$\mathbf{F}_{\text{grad}}(\mathbf{r}) = \alpha'/4 \, \nabla I_0(\mathbf{r}) \tag{2.10}$$

and

$$\mathbf{F}_{\text{scatt}}(\mathbf{r}) = \alpha''/2\, I_0(\mathbf{r})\nabla\phi(\mathbf{r}), \tag{2.11}$$

where $I_0(\mathbf{r}) = E_0^2(\mathbf{r})$ is the field intensity and α' and α'' are the real and imaginary part of the polarisability, respectively. This approximation is valid if the phase varies spatially much stronger than the amplitude. This is the case for weakly focused fields and for the fields given by Eq. (2.7).

For a spherical particle with volume $V = 4/3\,\pi a^3$ and dielectric constant ε_p embedded in a medium with dielectric constant ε_{m}, the polarisability is given by Clausius-Mossotti relation (also Lorentz-Lorenz formula) [Rohrbach and Stelzer, 2001; Novotny and Hecht, 2006]:

$$\alpha = 3V\epsilon_0(\epsilon_p - \epsilon_m)/(\epsilon_p + 2\epsilon_m). \tag{2.12}$$

Generally, α is a tensor of rank two. However, for a spherical particle α becomes a scalar.

The gradient force is proportional to the dispersive (real) part α', whereas the scattering force is proportional to the dissipative (imaginary) part α'' of the complex polarisability α. The phase $\phi(\mathbf{r})$ can be written in terms of the local $\mathbf{k}$ vector $\phi(\mathbf{r}) = \mathbf{k}\cdot\mathbf{r}$. Hence, the scattering force results from momentum transfer from the radiation field to the particle. Momentum can be transferred either by absorption or scattering of a photon. Photon scattering by the particle changes the electric field. This, in turn, modifies the optical force acting on the particle. This backaction effect also known as radiation reaction is accounted for by an effective polarisability [Novotny and Hecht, 2006]

$$\alpha_{\text{eff}} = \alpha\left(1 - i\frac{k^3}{6\pi\epsilon_0}\alpha\right)^{-1}. \tag{2.13}$$

Consequently, even for a lossless particle ($\text{Im}(\epsilon_p) = 0$), the scattering force does not vanish completely!

From (2.10), (2.11) and (2.7) we calculate the optical forces in the Gaussian approximation

$$\mathbf{F}_{\text{grad}}(\mathbf{r}) = -\alpha'_{\text{eff}} I_0(\mathbf{r}) \times \begin{pmatrix} x\, z_0^2 \,/\mathrm{w}_x^2(z^2+z_0^2) \\ y\, z_0^2 \,/\mathrm{w}_y^2(z^2+z_0^2) \\ z\left[(z/z_0)^2 + \left(1 - 2x/\mathrm{w}_x^2 - 2y/\mathrm{w}_y^2\right)\right]\left[z_0^2\,/2(z^2+z_0^2)\right] \end{pmatrix} \tag{2.14}$$

and

$$\mathbf{F}_{\text{scatt}}(\mathbf{r}) = \frac{\alpha''_{\text{eff}}}{2} I_0(\mathbf{r}) k \times \begin{pmatrix} x\,/R(z) \\ y\,/R(z) \\ 1 + \left(x^2+y^2\right) z_0^2\,/z^2 R(z)^2 \,-\left[x^2+y^2+2z\,z_0\right]/2zR(z) \end{pmatrix}, \tag{2.15}$$

where $I_0(\mathbf{r}) = E_0^2\left[1+(z/z_0)^2\right]^{-1} \exp\left(-2\left[x^2/\mathrm{w}_x^2(z) + y^2/\mathrm{w}_y^2(z)\right]\right)$.

The field intensity at the focus, E_0^2, is related to the total power of the Gaussian beam by

$$P = \int_{-\infty}^{\infty}\int_{-\infty}^{\infty} \langle \mathbf{S}\rangle \mathbf{n}_z dx dy = c\epsilon_0 \pi \mathrm{w}_x \mathrm{w}_y E_0^2\,/4\,, \tag{2.16}$$

where c is the speed of light, $\mathbf{n}_z$ is the direction of beam propagation and $\langle \mathbf{S}\rangle = \langle \mathbf{H}\times\mathbf{E}\rangle$ is the the Poynting vector.

For small displacements $|\mathbf{r}| \ll \lambda$, we expand equations (2.14) and (2.15) to get the first order nonlinear terms

$$\mathbf{F}_{\text{grad}}(\mathbf{r}) \approx -\begin{pmatrix} \mathrm{k}_{\text{trap}}^{(x)}\left[1 - 2x^2/\mathrm{w}_x^2 - 2y^2/\mathrm{w}_y^2 - 2z^2/z_0^2\right] x \\ \mathrm{k}_{\text{trap}}^{(y)}\left[1 - 2x^2/\mathrm{w}_x^2 - 2y^2/\mathrm{w}_y^2 - 2z^2/z_0^2\right] y \\ \mathrm{k}_{\text{trap}}^{(z)}\left[1 - 4x^2/\mathrm{w}_x^2 - 4y^2/\mathrm{w}_y^2 - 2z^2/z_0^2\right] z \end{pmatrix} \tag{2.17}$$

and

$$\mathbf{F}_{\text{scatt}}(\mathbf{r}) \approx \frac{\alpha''_{\text{eff}}}{\alpha'_{\text{eff}}} \mathrm{k}_{\text{trap}}^{(z)} \begin{pmatrix} k\,xz \\ k\,yz \\ \gamma_0 + \gamma_z z^2 + \gamma_x x^2 + \gamma_y y^2, \end{pmatrix} \tag{2.18}$$

where

$$\gamma_0 = z_0(z_0 k - 1), \tag{2.19a}$$
$$\gamma_z = (2 - z_0 k)/z_0, \tag{2.19b}$$
$$\gamma_x = \left[k/2 - 2(z_0 - k\, z_0^2)\,/\mathrm{w}_x^2\right] \text{ and} \tag{2.19c}$$
$$\gamma_y = \left[k/2 - 2(z_0 - k\, z_0^2)\,/\mathrm{w}_y^2\right]. \tag{2.19d}$$

are constants that depend only on the optical field but not on the properties of the particle.

The longitudinal and transversal trap stiffness are given by

$$\mathrm{k}_{\mathrm{trap}}^{(x)} = \alpha'_{\mathrm{eff}} E_0^2/\mathrm{w}_x^2, \tag{2.20a}$$
$$\mathrm{k}_{\mathrm{trap}}^{(y)} = \alpha'_{\mathrm{eff}} E_0^2/\mathrm{w}_y^2 \text{ and} \tag{2.20b}$$
$$\mathrm{k}_{\mathrm{trap}}^{(z)} = \alpha'_{\mathrm{eff}} E_0^2/2z_0^2, \tag{2.20c}$$

respectively. As expected, the trap stiffness increases with polarisability, laser power and field confinement.

2.3.2 Discussion

Since the scattering force points mainly in the direction of beam propagation, the equilibrium position $z_{\mathrm{eq.}}$ is not exactly at the intensity maximum but is displaced along z. For the Gaussian model we find

$$z_{\mathrm{eq.}} \approx \frac{\alpha''_{\mathrm{eff}}}{\alpha'_{\mathrm{eff}}}\gamma_0. \tag{2.21}$$

If the scattering force is too strong, the particle is pushed out of the optical trap. Expanding (2.13) to lowest order $\alpha_{\mathrm{eff}} \approx \alpha(1 + ik^3[6\pi\epsilon_0]^{-1}\alpha)$, we find that

$$\alpha''_{\mathrm{eff}}/\alpha'_{\mathrm{eff}} \propto (ka)^3 \Delta\epsilon, \tag{2.22}$$

where $\Delta\epsilon = (\epsilon_p - \epsilon_m)/(\epsilon_p + 2\epsilon_m) \approx (\epsilon_p - \epsilon_m)\,/3\epsilon_m$ is the relative dielectric contrast between the particle and the surrounding medium. Hence,

the relative strength of the scattering force decreases for smaller particles and lower dielectric contrast. For SiO_2, the dielectric contrast is about five times higher in air/vacuum ($\Delta\epsilon_{\text{air}} = 0.15$) than in water ($\Delta\epsilon_{\text{water}} = 0.03$). Consequently, it is more difficult to trap big SiO_2 particles in air/vacuum than in water. However, the total optical force $\mathbf{F} \propto a^3\Delta\epsilon$ scales with the volume and the relative dielectric contrast. This makes it easier to trap small SiO_2 particles in air/vacuum than in water.

The optical force becomes weak for small particles. If it becomes too weak, any external disturbance destabilises the trap. In vacuum, the main disturbance comes from collisions with residual air molecules (c.f. section 2.4). In consequence, to successfully trap particles with a single laser beam we have to choose a particle size in the intermediate region where the gradient force dominates over the scattering force but the total optical force is still strong enough to dominate all other forces. The range of stable trapping is shown as a white region in Figs. 2.4, 2.6 and 2.7.

Figure 2.4 shows the optical force in the direction of beam propagation at the focus as a function of particle radius. The force has been calculated with full Mie theory following reference [Neto and Nussenzveig, 2000]. Due to symmetry, the gradient force vanishes at the focus and the total force equals the scattering force. For small particles, the scattering force is negligible and the trap center coincides with the focus. The force increases with particle size. It is always positive and, therefore, pushes the particle away from the focus. As the particle moves away from the focus, the gradient force (which is zero at the focus and points toward the focus otherwise) increases until the total force is zero and a stable trap is formed ahead of the optical focus. Interference of scattered and incident light gives rise to Mie-resonances and leads to a more complex dependency for bigger particles. For particles larger than $\sim 120\,\text{nm}$, the scattering force is too strong and the particle is pushed out of the trap, except of a few special resonances. For particle smaller than $\sim 35\,\text{nm}$, thermal excitations destabilise the trap.

Figure 2.5 shows the force profile along the optical axes for a $a = 75\text{nm}$

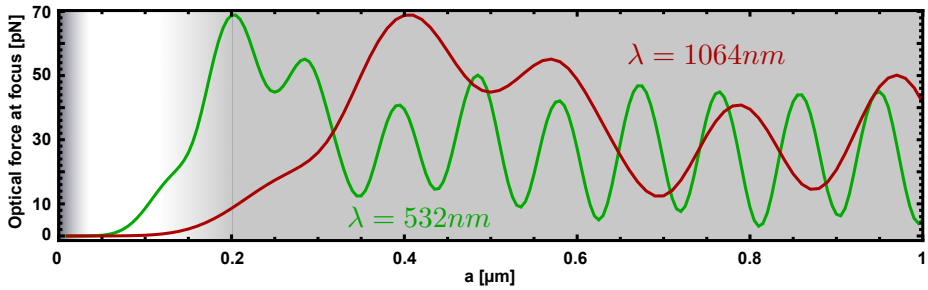

Figure 2.4: **Optical force at focus along z axis as a function of particle size** *calculated for* $\lambda = 1064nm$ *and* $\lambda = 532nm$*. At the focus, the gradient force vanishes and the total optical force equals the scattering force. For small particle size, the force is almost zero and a stable trap is formed near the focus. The force at the focus is always positive and scales with the volume for small particles . Therefore, the particle is pushed along the optical axes and the equilibrium position is displaced ahead of the focus. Interference of scattered and incident light gives rise to Mie-resonances and leads to a more complex dependency for bigger particles. For particles larger than* $a \sim 120\,\mathrm{nm}$*, the scattering force is too strong and the particle is pushed out of the trap, except of a few special resonances. For particle smaller than* $a \sim 35\,\mathrm{nm}$*, thermal excitations destabilize the trap. The region where stable trapping is possible is shown in white.*

Silica particle calculated with Mie theory [Neto and Nussenzveig, 2000], from the Debye integral (equations (2.1), (2.10) and (2.11)) and with the Gaussian model (equations (2.17) and (2.18)). All three models yield similar results close to the trap center. For larger distances ($> 0.5\,\mu\mathrm{m}$), the optical fields are not accurately described by the Gaussian model (see also 2.2) and the simple model fails. However, we are mostly interested in small displacements from the trap center ($z_{\mathrm{eq.}} \approx 0.2\,\mu\mathrm{m}$) for which the model still gives good results. The inset of figure 2.5 shows the optical forces for a larger $a = 250\,\mathrm{nm}$ particle. For this particle size the dipolar approximation

breaks down and the values obtained with the dipolar models (Debye and Gauss) differ significantly from the exact Mie-solution. The two dipolar models predict that there is no stable trapping position anywhere on the optical axis, whereas Mie theory finds a stable position at $\approx 1.5\,\mu$m.

Figure 2.6 shows the position of the trap center and the trap stiffness as a

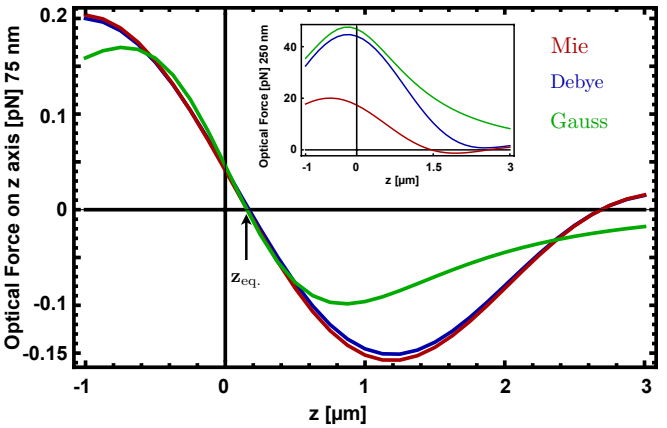

Figure 2.5: **Optical forces along axis for 75nm particle** *calculated with different models. Around the center of the trap ($z_{\text{eq.}} \approx 0.2\,\mu$m) all models give similar results. At larger distances the Gaussian description of the optical fields breaks down. Inset: For bigger particles (here $a = 250\,$nm), the dipole approximation for the polarisability fails. The two dipolar models don't find a stable trap, whereas Mie theory predicts a stable, albeit shallow trap at $\approx 1.5\,\mu$m.*

function of particle size calculated with all three models. The trap stiffness is given by the slope of the optical force at the trap center. For particles larger than $\sim$ 120nm the center of the trap is already more than half a wavelength away from the focus and trapping with a single beam is very difficult. A stable trapping position does not exist because the scattering force is always stronger than the gradient force. Mie theory still finds a few exceptional particle sizes where trapping of larger particles is possible.

When the particle size is commensurate with the optical wavelength, the particle acts as a resonator. As a consequence the scattered field and therefore the optical forces exhibit resonances (see also Fig. 2.4), which can result in a stable optical trap even for bigger particles (But a stable trap does not exist for all optical resonances!). However, the range of particle sizes for which resonant trapping is possible is very narrow. This makes trapping of particles larger than $\sim 120\,\mathrm{nm}$ impractical for the experimental parameters considered here.

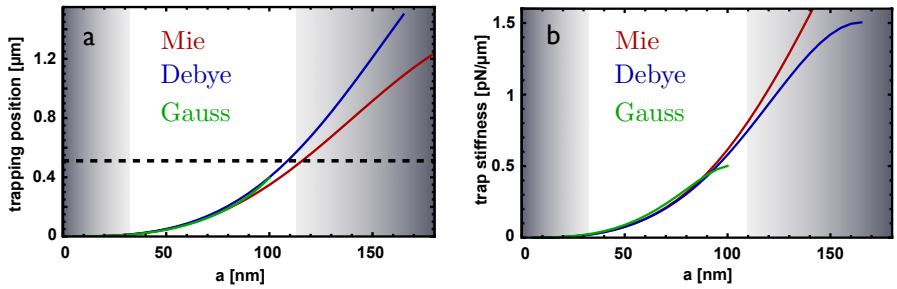

Figure 2.6: **Trap position and trap stiffness** *as a function of particle radius a. We compare the three models discussed in the text. (a) Trap position along z. The black dashed line marks where the equilibrium position* $z_{\mathrm{eq.}}$ *is half a wavelength ahead of the focus. For larger displacements of* $z_{\mathrm{eq.}}$*, we assume that the trap is unstable. The white space marks the particle sizes for which stable trapping is possible. (b) Trap stiffness along z axis. The two dipolar models, Gauss and Debye, don't find a solution for particles larger than* $a \approx 100\,\mathrm{nm}$ *and* $a \approx 160\,\mathrm{nm}$*, respectively. The exact Mie theory finds a solution up to* $a \approx 300\,\mathrm{nm}$*. For larger particles, a stable trap only exists when very specific resonance conditions are fulfilled (not shown here).*

2.4 Optical potential

In this section we introduce the concept of an optical potential. From the optical potential we can estimate a lower bound of particle size for which a stable trap can be formed.

Strictly speaking a potential can only be defined for a conservative force. As we have seen in the previous section, the scattering force is not a conservative force (c.f. Eq. (2.11)). However, for sub-wavelength particles, the non-conservative scattering force is negligible and we can define a potential $U = -\alpha'/4\ I_0(\mathbf{r})$ (c.f. Eq. (2.10)). With (2.16) the depth of the potential is given by

$$\Delta U = \alpha' / \pi c \epsilon_0 \mathrm{w}_x \mathrm{w}_y\ P\ . \tag{2.23}$$

Comparing the depth of the potential to the thermal energy of the environment we can estimate a lower bound of particle sizes for which a stable trap exists. If the thermal energy is comparable to or larger than the depth of the potential, a thermally excited particle can escape. The energy of the thermal bath follows a Maxwell-Boltzmann distribution with mean value of $k_B T_0$. Since the tail of the distribution extends to high energies, the potential depth should be at least $\simeq 10 k_B T_0$ [Ashkin et al., 1986] to make particle escape through thermal excitation unlikely (The likelihood of finding the particle with energy $10\, k_B T_0$ is less than 0.02%). Assuming that the trap becomes unstable at $\simeq 10 k_B T_0$, we can measure the potential depth at optical power P_0 by measuring the optical power P_{lost} when the particle is lost. For our typical experimental conditions we find $\Delta U(P_0) = 10\, k_B T_0\, P_0 / P_{\mathrm{lost}} \approx 28 k_B T_0$.

2.5 Conclusions

In conclusion, we have derived a simple analytical model of the optical forces. The model is based on a Gaussian description of the focal field and the dipolar approximation for the particle polarisability. Thus, it is valid for small sub-wavelength particles and small displacements from the

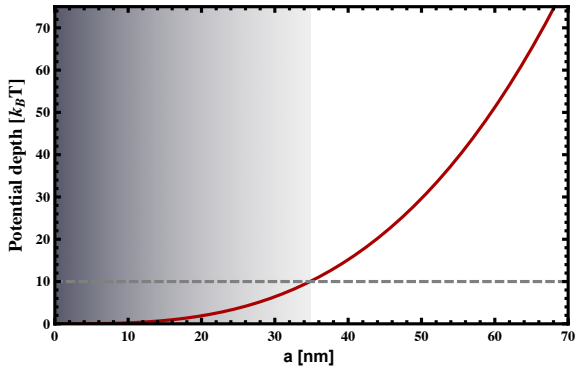

Figure 2.7: **Potential Depth** *as a function of particle size for* $P = 0.1\,\mathrm{W}$, $\mathrm{NA} = 0.8$ *and* $\lambda = 1064\,\mathrm{nm}$. *The gray region marks the particle sizes where the potential depth is below* $10\,k_BT_0$. *Hence, trapping at the given power will be difficult for particles with radius of less than* $\sim 35\,\mathrm{nm}$.

trap center. These requirements are generally fulfilled for our experimental conditions. The model allows us to understand the dependence of the trap parameters (trap stiffness and trap position) on the experimental conditions (optical power, field confinement and particle polarisability). For typical experimental conditions we find that a stable optical trap exists for particles in the range $a \approx 35 \ldots 120\,\mathrm{nm}$. For smaller particles, thermal excitations have a high probability to kick the particle out of the trap. Bigger particles experience a strong scattering force, which pushes them out of the trap.

Optical forces not only allow us to cool and drive the mechanical oscillator but they also determine the mechanical properties of the device. This is different from conventional nanomechanical oscillators, where the mechanical properties depend on the material properties and the fabrication process. There exist also an intermediate solution, where the intrinsic mechanical properties are enhanced by optical forces [Chang et al., 2012].

CHAPTER 3

Parametric Feedback Cooling of a Laser-trapped Nanoparticle

We optically trap a single nanoparticle in high vacuum and cool its three spatial degrees of freedom by means of active parametric feedback. Using a single laser beam for both trapping and cooling we demonstrate a temperature compression ratio of four orders of magnitude. The absence of a clamping mechanism provides robust decoupling from the heat bath and eliminates the requirement of cryogenic precooling. The small size and mass of the nanoparticle yield high resonance frequencies and high quality factors along with low recoil heating, which are essential conditions for ground state cooling and for low decoherence. The trapping and cooling scheme presented here opens new routes for testing quantum mechanics with mesoscopic objects and for ultrasensitive metrology and sensing.

3.1 Introduction

The interaction between light and matter sets ultimate limits on the accuracy of optical measurements. Vladimir B. Braginsky predicted that the finite response time of light in an optical interferometer can lead to me-

chanical instabilities [Braginsky, 1977] and impose limits on the precision of laser-based gravitational interferometers. Later, it was demonstrated that this "dynamic back-action mechanism" can be used to reduce the oscillation amplitude of a mechanical system and to effectively cool it below the temperature of the environment [Metzger and Karrai, 2004; Cohadon et al., 1999; Arcizet et al., 2006; Gigan et al., 2006; Schliesser et al., 2006; Usami et al., 2012] and even to its quantum ground state [Chan et al., 2011; Teufel et al., 2011; Verhagen et al., 2012]. In addition to the fascinating possibility of observing the quantum behavior of a mesoscopic system, many applications have been proposed for such systems ranging from detection of exotic forces [Geraci et al., 2010; Romero-Isart et al., 2011b; Manjavacas and García de Abajo, 2010] to the generation of non-classical states of light and matter [Chang et al., 2010; Romero-Isart et al., 2010].

Most of the mechanical systems studied previously are directly connected to their thermal environment, which imposes limits to thermalization and decoherence. As a consequence, clamped systems require cryogenic precooling. A laser-trapped particle in ultrahigh vacuum, by contrast, has no physical contact to the environment [Ashkin and Dziedzic, 1976, 1977], which makes it a promising system for ground state cooling even at room temperatures [Chang et al., 2010; Romero-Isart et al., 2010]. Cooling of micron-sized particles to milli-Kelvin temperatures has recently been achieved by applying an *active* optical feedback inspired by atom cooling experiments [Li et al., 2011]. A particle is trapped by two counter-propagating beams and cooling is performed with three additional laser beams via radiation pressure. However, because light scattering leads to recoil heating there is a limit for the lowest attainable temperature. Eliminating recoil heating as the limiting factor for ground state cooling requires considerably smaller mechanical systems, such as single dielectric nanoparticles [Chang et al., 2010; Romero-Isart et al., 2010]. Here we demonstrate for the first time optical trapping in high vacuum of a fused silica nanoparticle of radius $a \sim 70\,\mathrm{nm}$. Additionally, we employ a novel cooling scheme based on the optical gradient force to cool its motional degrees of freedom from room temperature to $\sim 50\,\mathrm{mK}$ (compression factor of $\sim 10^4$).

3.2 Description of the experiment

In our experiments we use a laser beam of wavelength $\lambda = 1064\,\mathrm{nm}$ ($\sim 100\,\mathrm{mW}$), focused by an NA=0.8 lens mounted in a vacuum chamber (details chapter 1). A single nanoparticle is trapped by means of the optical gradient force, which acts towards the center of the trap for all three translational degrees of the nanoparticle (c.f. Fig. 3.1). For particles much smaller than the wavelength, the polarisability scales as $\alpha \propto a^3$ and the gradient force dominates over the scattering force (c.f. chapter 2). Scattered light from the particle is measured interferometrically with three separate photodetectors that render the particle's motion in the x, y, and z directions (c.f. section 1.1). This phase-sensitive detection scheme makes use of balanced detection and yields a noise floor of $\sim 1.2\,\mathrm{pm}/\sqrt{\mathrm{Hz}}$. Fig. 3.1 shows a photograph of a trapped nanoparticle along with a typical time trace of the particle's x coordinate. Trapping times of several days have been achieved at pressures below $10^{-5}\,\mathrm{mBar}$, indicating that the particle's internal temperature does not affect the center of mass motion [Chang et al., 2010] and that melting of the particle is not a concern.

3.2.1 Particle dynamics

At ambient pressure the particle's motion is dominated by the viscous force (Stokes force) due to the random impact of gas molecules. However, as shown in Fig. 3.1(b), the inertial force dominates in a vacuum of a few millibars as the particle's motion becomes ballistic [Li et al., 2010].
For small oscillation amplitudes, the trapping potential is harmonic and the three spatial dimensions are decoupled. Each direction can be characterised by a frequency Ω_0, which is defined by the particle mass $m$and the trap stiffness $\mathrm{k_{trap}}$ as $\Omega_0 = \sqrt{\mathrm{k_{trap}}/m}$. The equation of motion for the particle's

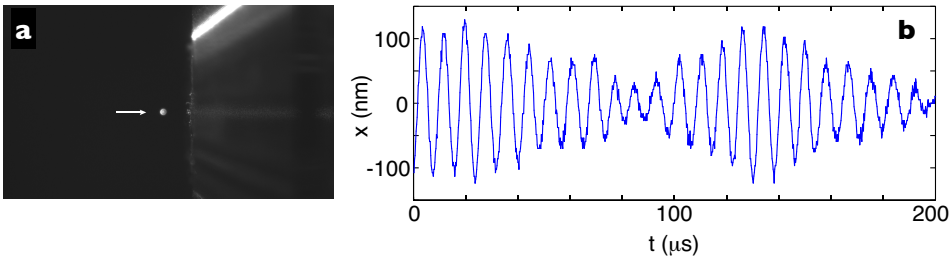

Figure 3.1: **Trapping of a nanoparticle. (a)** *light scattered from a trapped silica nanoparticle (arrow). The object to the right is the outline of the objective that focuses the trapping laser.* **(b)** *Time trace of the particle's x coordinate (transverse to the optical axis) at 2 mBar pressure.*

motion ($q = x, y, z$) is

$$\ddot{q}(t) \;+\; \Gamma_0\,\dot{q}(t) \;+\; \Omega_0^2\,q(t) \;=\; \frac{1}{m}\left[\mathcal{F}_{\mathrm{fluct}}(t) + F_{\mathrm{opt}}(t)\right], \tag{3.1}$$

where $\mathcal{F}_{\mathrm{fluct}}$ is a random Langevin force that satisfies $\langle \mathcal{F}_{\mathrm{fluct}}(t)\,\mathcal{F}_{\mathrm{fluct}}(t')\rangle = 2m\Gamma_0\,k_B T_0\,\delta(t-t')$ according to the fluctuation-dissipation theorem. $F_{\mathrm{opt}}(t) = \Delta k_{\mathrm{trap}}(t)\,q(t)$ is a time-varying, non-conservative optical force introduced by parametric feedback. It leads to shifts $\delta\Gamma$ and $\delta\Omega$ in the particle's natural damping rate Γ_0 and oscillation frequency Ω_0, respectively.

3.2.2 Parametric feedback

To control and stabilise the particle's motion in the optical trap we implemented an active feedback loop (c.f. 1.1). All three spatial degrees of freedom are controlled with the same laser used for trapping. To cool the CoM motion of the particle we employ a *parametric* feedback scheme, similar to parametric amplification of laser fields [Yariv, 1989] and stabilization of nanomechanical oscillators [Villanueva et al., 2011]. After trapping a single nanoparticle at ambient temperature and pressure we evacuate the

vacuum chamber in order to reach the desired vacuum level.

Parametric feedback is activated as soon as we enter the ballistic regime. In a time-domain picture, the feedback loop hinders the particle's motion by increasing the trap stiffness whenever the particle moves away from the trap center and reducing it when the particle falls back toward the trap. In the frequency domain, this corresponds to a modulation at twice the trap frequency with an appropriate phase shift. Our parametric feedback is fundamentally different from previous active feedback schemes based on radiation pressure [Poggio et al., 2007]. Radiation pressure acts only along the direction of beam propagation and therefore requires a separate cooling laser for every oscillation direction [Li et al., 2011]. In contrast, the gradient force points towards the center of the trap, thus allowing us to cool all three directions with a single laser beam.

Fig. 3.2 illustrates our parametric feedback mechanism. To obtain a signal at twice the oscillation frequency we multiply the particle's position $q(t)$ with it's time derivative. The resulting signal $q(t)\,\dot{q}(t)$ is then phase-shifted by a controlled amount in order to counteract the particle's oscillation. Note that depending on the latency of the feedback loop we can achieve damping or amplification of the particle's oscillation. In the absence of active feedback, the particle's oscillation naturally locks to the modulation phase in such a way as to achieve amplification [Yariv, 1989]. Cooling therefore requires active feedback to adjust the modulation phase constantly.

In our cooling scheme, frequency doubling and phase shifting is done independently for each of the photodetector signals x, y and z. Since the three directions are spectrally separated (see Fig. 3.3b), there is no cross-coupling between the three signals, that is, modulating one of the signals does not affect the other signals. Therefore, it is possible to sum up all three feedback signals and use the result to drive a single EOM that modulates the power P of the trapping laser. Thus, using a single beam we are able to effectively cool all spatial degrees of freedom.

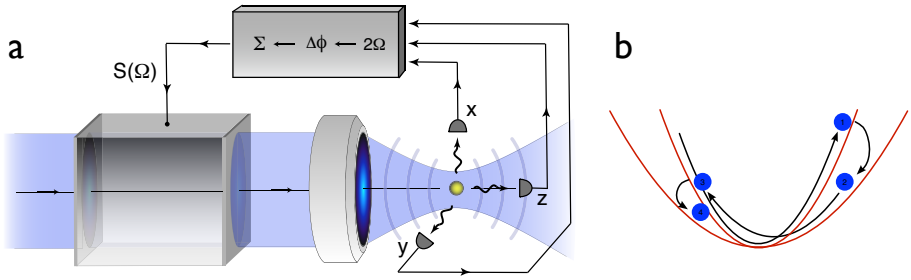

Figure 3.2: **Principle of parametric feedback cooling. (a)** *The center-of-mass motion of a laser-trapped nanoparticle in ultrahigh vacuum is measured interferometrically with three detectors, labeled x, y, and z. Each detector signal is frequency doubled and phase shifted. The sum of these signals is used to modulate the intensity of the trapping beam.* **(b)** *The particle's motion is hindered by increasing the trap stiffness whenever the particle moves away from the trap center. When the particle falls back towards the center of the trap the power decreases, thereby reducing the potential energy of the particle. As a result of the modulation, the particle's energy decreases.*

3.3 Theory of parametric feedback cooling

Starting from Eq. (3.1), we now derive a stochastic differential equation for the energy in the limit of a highly underdamped system ($Q \gg 1$)[1]

$$E(p,q) = \frac{1}{2}m\Omega_0^2 q^2 + \frac{p^2}{2m}. \tag{3.2}$$

It turns out that in the low friction limit, the stochastic equation of motion for the energy (or rather, for the square root of the energy) can be written in a form which resembles over-damped Brownian motion. As a result, we can consider the energy as the only variable[2]. As a side product we also obtain the energy distribution in the non-equilibrium steady state generated by the

[1] This section is based on a private note from C.Dellago.
[2] note that this works only in the low friction limit

application of the feedback loop. In fact, in energy space the dynamics of the system with feedback can be viewed as an equilibrium dynamics occurring in a system with an additional force term.

3.3.1 Equations of motion

For the developments below it is more convenient to write (3.1) as a stochastic differential equation (SDE),

$$\mathrm{d}q = \frac{p}{m}\mathrm{d}t, \tag{3.3a}$$

$$\mathrm{d}p = (-m\Omega_0^2 q - \Gamma_0 p - \Omega_0 \eta q^2 p)\mathrm{d}t + \sqrt{2m\Gamma_0 k_\mathrm{B} T_0}\mathrm{d}W, \tag{3.3b}$$

where we have used $p = m\dot{q}$, $F_\mathrm{opt} = \Omega_0\eta q^2\dot{q}$ and $\mathcal{F}_\mathrm{fluct} = \sqrt{2m\Gamma_0 k_\mathrm{B} T_0}\mathrm{d}W$. Here, $W(t)$ is a Wiener process with

$$\langle W(t)\rangle = 0 \tag{3.4a}$$

$$\langle W(t)W(t')\rangle = t' - t. \tag{3.4b}$$

Note that in particular $\langle W^2(t)\rangle = t$ for any time $t \geq 0$. Accordingly, for a short (infinitesimal) time interval $\mathrm{d}t$ we have

$$\langle \mathrm{d}W\rangle = 0 \tag{3.5}$$

$$\langle (\mathrm{dW})^2\rangle = \mathrm{d}t. \tag{3.6}$$

The time derivative of the Wiener process, $\eta(t) = \mathrm{d}W(t)/\mathrm{d}t$, is white noise and it is related to the random force by $\mathcal{F}_\mathrm{fluct}(t) = \sqrt{2m\Gamma_0 k_\mathrm{B} T_0}\eta(t)$.

3.3.2 Stochastic differential equation for the energy

We determine the energy change $\mathrm{d}E$ that occurs during the short time interval $\mathrm{d}t$ during which position and momentum change by $\mathrm{d}q$ and $\mathrm{d}p$ as specified by the equations of motion (3.3a) and (3.3b). To lowest order, the energy change is given by

$$\mathrm{d}E = \left(\frac{\partial E}{\partial q}\right)\mathrm{d}q + \left(\frac{\partial E}{\partial p}\right)\mathrm{d}p + \frac{1}{2}\left(\frac{\partial^2 E}{\partial p^2}\right)(\mathrm{d}p)^2 \tag{3.7}$$

Note that this equation differs from the usual chain rule because we have to keep the term proportional to $(\mathrm{d}p)^2$. The reason is that according to Eq. (3.3b), $\mathrm{d}p$ depends on $\mathrm{d}W$ which is of order $\sqrt{\mathrm{d}t}$. Hence, if we want to keep all terms at last up to order $\mathrm{d}t$, we cannot neglect the second order term in the above equation because $(\mathrm{d}p)^2$ is of order $\mathrm{d}t$. In contrast, we can safely neglect the terms proprtional to $(\mathrm{d}q)^2$ and $\mathrm{d}q\mathrm{d}p$, because they are of order $\mathrm{d}t$ and $(\mathrm{d}t)^{3/2}$, respectively[1].

Computing the derivatives of the energy with respect to q and p we obtain

$$\mathrm{d}E = m\Omega_0^2 q\mathrm{d}q + \frac{p}{m}\mathrm{d}p + \frac{1}{2m}(\mathrm{d}p)^2. \tag{3.8}$$

Inserting $\mathrm{d}q$ and $\mathrm{d}p$ from Eqns. (3.3a) and (3.3b) and neglecting all terms of order $(\mathrm{d}t)^{3/2}$ or higher yields

$$\mathrm{d}E = -m(\Gamma_0 + \Omega_0\eta q^2)\left(\frac{p}{m}\right)^2 \mathrm{d}t + \frac{p}{m}\sqrt{2m\Gamma_0 k_\mathrm{B} T_0}\mathrm{d}W + \Gamma_0 k_\mathrm{B} T_0 \mathrm{d}W^2. \tag{3.9}$$

To avoid the multiplicative noise of Eq. (3.9) we consider the variable $\epsilon = \sqrt{E}$ instead of the energy E. The change $\mathrm{d}\epsilon$ due to the changes $\mathrm{d}q$ and $\mathrm{d}p$ occurring during an infinitesimal time interval $\mathrm{d}t$ is given by

$$\mathrm{d}\epsilon = \left(\frac{\partial\epsilon}{\partial q}\right)\mathrm{d}q + \left(\frac{\partial\epsilon}{\partial p}\right)\mathrm{d}p + \frac{1}{2}\left(\frac{\partial^2\epsilon}{\partial p^2}\right)(\mathrm{d}p)^2 \tag{3.10}$$

as all other terms are of order $(\mathrm{d}t)^{3/2}$ or higher. Evaluation of the partial derivatives yields

$$\mathrm{d}\epsilon = m\Omega_0^2\frac{q}{2\epsilon}\mathrm{d}q + \frac{1}{2\epsilon}\frac{p}{m}\mathrm{d}p + \frac{1}{2}\left(\frac{1}{2m\epsilon} - \frac{1}{4\epsilon^3}\frac{p^2}{m^2}\right)(\mathrm{d}p)^2. \tag{3.11}$$

Using the equations of motion (3.3a) and (3.3b) and exploiting that $(\mathrm{d}p)^2 =$

[1] This way to apply the chain rule is the basis of the so-called Itô calculus.

$2m\Gamma_0 k_\mathrm{B} T_0 (\mathrm{d}W)^2$ up to order $\mathrm{d}t$ we obtain

$$\begin{aligned} \mathrm{d}\epsilon &= -\frac{m}{2\epsilon}(\Gamma_0 + \Omega_0 \eta q^2)\left(\frac{p}{m}\right)^2 \mathrm{d}t + \frac{\sqrt{2m\Gamma_0 k_\mathrm{B} T_0}}{2\epsilon}\frac{p}{m}\mathrm{d}W \\ &\quad + \frac{\Gamma_0 k_\mathrm{B} T_0}{2\epsilon}\left(1 - \frac{p^2}{2m\epsilon^2}\right)(\mathrm{d}W)^2. \end{aligned} \tag{3.12}$$

We now integrate this equation over an oscillation period $\tau = 2\pi/\Omega_0$ to obtain the change $\Delta\epsilon = \int_0^\tau \mathrm{d}\epsilon$ over one oscillation period,

$$\begin{aligned} \Delta\epsilon &= -\frac{\Gamma_0}{2}\int_0^\tau \frac{p^2}{m\epsilon}\mathrm{d}t - \frac{\Omega_0 \eta}{2}\int_0^\tau \frac{q^2 p^2}{m\epsilon}\mathrm{d}t \\ &\quad + \sqrt{2m\Gamma_0 k_\mathrm{B} T_0}\int_0^\tau \frac{p}{2m\epsilon}\mathrm{d}W \\ &\quad + \Gamma_0 k_\mathrm{B} T_0 \int_0^\tau \frac{1}{2\epsilon}\left(1 - \frac{p^2}{2m\epsilon^2}\right)(\mathrm{d}W)^2. \end{aligned} \tag{3.13}$$

To compute the integrals on the right hand side of the above equation, we assume that in the low-friction limit the energy E, and hence also ϵ remains essentially constant over one oscillation period. We also assume that the feedback mechanism changes the energy of the system slowly and that the motion of the system during one oscillation period is practically not affected by the feedback either. In the low friction regime, where the coupling to the bath is weak, a small feedback strength (i.e., a small η) should be sufficient for considerable cooling. Accordingly, during one oscillation period the position q and the momentum p are assumed to evolve freely:

$$q(t) = \epsilon\sqrt{\frac{2}{m\Omega_0^2}}\sin\Omega_0 t, \tag{3.14}$$

$$p(t) = m\dot{q}(t) = \epsilon\sqrt{2m}\cos\Omega_0 t, \tag{3.15}$$

where we have selected the phase of the oscillation such that the position $q = 0$ at time 0. Hence, the first two integrals of (3.13) are given by

$$\int_0^\tau \frac{p^2}{m\epsilon}\mathrm{d}t = 2\epsilon\int_0^\tau \cos^2\Omega_0 t\,\mathrm{d}t = \epsilon\tau \tag{3.16}$$

and

$$\int_0^\tau \frac{q^2p^2}{m\epsilon}\mathrm{d}t = \frac{4\epsilon^3}{m\Omega_0^2}\int_0^\tau \sin^2\Omega_0 t\cos^2\Omega_0 t\,\mathrm{d}t = \frac{\epsilon^3\tau}{2\Omega_0^2 m}. \tag{3.17}$$

Insertion of these results and of the harmonic expressions for $q(t)$ and $p(t)$ from above into Eq. (3.13) gives

$$\begin{aligned}\Delta\epsilon &= -\frac{\Gamma_0\epsilon}{2}\tau - \frac{\Omega_0\eta\epsilon^3}{4m\Omega_0^2}\tau \\ &\quad +\sqrt{\Gamma_0 k_\mathrm{B}T_0}\Delta R_1 \\ &\quad +\frac{\Gamma_0 k_\mathrm{B}T_0}{2\epsilon}\Delta R_2.\end{aligned} \tag{3.18}$$

where ΔR_1 and ΔR_2 are given by

$$\Delta R_1 = \int_0^\tau \cos\Omega_0 t\,\mathrm{d}W \tag{3.19}$$

and

$$\Delta R_2 = \int_0^\tau \sin^2\Omega_0 t\,(\mathrm{d}W)^2, \tag{3.20}$$

Since $W(t)$ is a Wiener process, ΔR_1 and ΔR_2 are random numbers. Next we will determine the statistical properties of ΔR_1 and ΔR_2.

As ΔR_1 is the result of a (weighted) sum of Gaussian random numbers, it will be a Gaussian random number, too. The mean of ΔR_1 is given by

$$\langle\Delta R_1\rangle = \langle\int_0^\tau \cos\Omega_0 t\,\mathrm{d}W\rangle = \int_0^\tau \cos\Omega_0 t\langle\mathrm{d}W\rangle = 0, \tag{3.21}$$

where the angular brackets imply an average over all noise histories. The variance of ΔR_1 is given by

$$\begin{aligned}\langle(\Delta R_1)^2\rangle &= \langle\int_0^\tau \cos\Omega_0 t\,\mathrm{d}W\int_0^\tau \cos\Omega_0 t'\,\mathrm{d}W'\rangle \\ &= \int_0^\tau\int_0^\tau \cos\Omega_0 t\cos\Omega_0 t'\langle\mathrm{d}W\mathrm{d}W'\rangle \\ &= \int_0^\tau \cos^2\Omega_0 t\,\mathrm{d}t = \frac{\tau}{2},\end{aligned} \tag{3.22}$$

where we have exploited that $\langle \mathrm{d}W \mathrm{d}W' \rangle = \delta(t'-t)\mathrm{d}t$. Hence, the random variable ΔR_1 can be written as

$$\Delta R_1 = \sqrt{\frac{1}{2}} W(\tau), \tag{3.23}$$

where $W(\tau)$ is a Wiener process at τ, i.e. a Gaussian random variable with variance τ.

In a similar way, we can show that the mean of ΔR_2 is given by

$$\begin{aligned} \langle \Delta R_2 \rangle &= \langle \int_0^\tau \sin^2 \Omega_0 t \, (\mathrm{d}W)^2 \rangle \\ &= \int_0^\tau \sin^2 \Omega_0 t \langle (\mathrm{d}W)^2 \rangle \\ &= \int_0^\tau \sin^2 \Omega_0 t \mathrm{d}t = \frac{\tau}{2}, \end{aligned} \tag{3.24}$$

because of $\langle (\mathrm{d}W)^2 \rangle = \mathrm{d}t$. For the second moment of ΔR_2 we obtain

$$\begin{aligned} \langle (\Delta R_2)^2 \rangle &= \langle \int_0^\tau \sin^2 \Omega_0 t \, (\mathrm{d}W)^2 \int_0^\tau \sin \Omega_0 t' \, (\mathrm{d}W')^2 \rangle \\ &= \int_0^\tau \int_0^\tau \sin^2 \Omega_0 t \sin^2 \Omega_0 t' \langle (\mathrm{d}W)^2 (\mathrm{d}W')^2 \rangle \\ &= \int_0^\tau \int_0^\tau \sin^2 \Omega_0 t \sin^2 \Omega_0 t' \mathrm{d}t \mathrm{d}t' \\ &= \left(\int_0^\tau \sin^2 \Omega_0 t \mathrm{d}t \right)^2 = \frac{\tau^2}{4}, \end{aligned} \tag{3.25}$$

where we have used that $(\mathrm{d}W)^2$ and $(\mathrm{d}W')^2$ are uncorrelated and that $\langle (\mathrm{d}W)^2 \rangle = \mathrm{d}t$. Thus, the variance of ΔR_2 vanishes,

$$\langle (\Delta R_2)^2 \rangle - \langle \Delta R_2 \rangle^2 = \frac{\tau^2}{4} - \frac{\tau^2}{4} = 0. \tag{3.26}$$

This result implies that the random variable ΔR_2 is sharp such that it can be replaced by its average, $\Delta R_2 = \tau/2$.

Putting everything together we get

$$\Delta\epsilon = \left(-\frac{\Gamma_0\epsilon}{2} - \frac{\Omega_0\eta\epsilon^3}{4m\Omega_0^2} + \frac{\Gamma_0 k_\mathrm{B}T_0}{4\epsilon}\right)\tau + \sqrt{\frac{\Gamma_0 k_\mathrm{B}T_0}{2}}W(\tau). \tag{3.27}$$

Since the oscillation period τ is assumed to be short compared to the dissipation time scale $1/\Gamma_0$ (also the feedback strength η needs to be appropriately small), we can finally write the stochastic differential equation for the variable ϵ,

$$\mathrm{d}\epsilon = \left(-\frac{\Gamma_0\epsilon}{2} - \frac{\Omega_0\eta\epsilon^3}{4m\Omega_0^2} + \frac{\Gamma_0 k_\mathrm{B}T_0}{4\epsilon}\right)\mathrm{d}t + \sqrt{\frac{\Gamma_0 k_\mathrm{B}T_0}{2}}\mathrm{d}W. \tag{3.28}$$

This equation, in which ϵ is the only variable, is the main result of this section. It implies that the relaxation process can be understood as a Brownian motion of ϵ (or, equivalently, of the energy) under the influence of an external "force". Using Itô's formula we can derive the corresponding stochastic differential equation for the energy $E = \epsilon^2$:

$$\mathrm{d}E = \left(-\Gamma_0 E - \frac{\Omega_0\eta E^2}{2m\Omega_0^2} + \Gamma_0 k_\mathrm{B}T_0\right)\mathrm{d}t + \sqrt{E}\sqrt{2\Gamma_0 k_\mathrm{B}T_0}\mathrm{d}W. \tag{3.29}$$

Note that, in contrast to ϵ, the energy is subject to multiplicative noise.

3.3.3 Energy distribution

Equation (3.28) derived in the previous section resembles the Langevin equation of a variable ϵ evolving at temperature $k_\mathrm{B}T_0$ under the influence of an external force $f(\epsilon)$ at high friction ν:

$$\mathrm{d}\epsilon = \frac{1}{\nu}f(\epsilon)\mathrm{d}t + \sqrt{\frac{2k_\mathrm{B}T_0}{\nu}}\mathrm{dW} \tag{3.30}$$

This equation is known to sample the Boltzmann-Gibbs distribution

$$\rho(\epsilon) \propto \exp(-\beta_0 U(\epsilon)), \tag{3.31}$$

where $\beta_0 = 1/k_B T_0$ is the inverse temperature and

$$U(\epsilon) = \epsilon^2 + \frac{\alpha}{4}\epsilon^4 - k_B T_0 \ln \epsilon. \tag{3.32}$$

is the potential corresponding to the force $f(\epsilon) = -\mathrm{d}U(\epsilon)/\mathrm{d}\epsilon$. Here, we have introduced

$$\alpha = \frac{\eta}{m\Omega_0\Gamma_0} \tag{3.33}$$

to simplify the notation. Hence, Eq. (3.28) generates the distribution

$$\rho(\epsilon, \alpha) \propto \epsilon \exp\left\{-\beta_0\left(\epsilon^2 + \frac{\alpha}{4}\epsilon^4\right)\right\}, \tag{3.34}$$

which can be viewed as the equilibrium distribution of the "potential" $U(\epsilon)$. In the above equation we have included the feedback strength α explicitly as parameter for $\rho(\epsilon, \alpha)$ in order to indicate that this distribution is valid also for the non-equilibrium steady state generated by the feedback mechanism. The effect of the feedback is, however, reduced to a particular term in this potential. As can be easily seen by a change of variables from ϵ to E, the distribution of Eq. (3.34) corresponds to the energy distribution

$$\rho(E, \alpha) = \frac{1}{Z}\exp\left\{-\beta_0 E - \frac{\beta_0\alpha}{4}E^2\right\}, \tag{3.35}$$

where the normalisation factor $Z = \int \mathrm{d}E \rho(E, \alpha)$ is given by

$$Z = \sqrt{\frac{\pi}{\alpha\beta_0}} e^{\beta_0/\alpha} \mathrm{erfc}\left(\sqrt{\frac{\beta_0}{\alpha}}\right). \tag{3.36}$$

3.3.4 Effective temperature

The average energy is obtained by integration over the energy distribution of Eq. (6.7),

$$\langle E \rangle = Z^{-1} \int \mathrm{d}E\, E \exp\left\{-\beta_0 E - \frac{\beta_0\alpha}{4}E^2\right\}. \tag{3.37}$$

Evaluation of the integrals yields

$$\langle E\rangle = \frac{2}{\beta_0}\left(\sqrt{\frac{\beta_0}{\alpha}}\frac{e^{-\beta_0/\alpha}}{\sqrt{\pi}\,\mathrm{erfc}\left(\sqrt{\frac{\beta_0}{\alpha}}\right)} - \frac{\beta_0}{\alpha}\right), \tag{3.38}$$

where α is given by Eq. (3.33). Thus, the effective temperature T_{eff} obtained by applying the feedback mechanism is:

$$k_{\mathrm{B}}T_{\mathrm{eff}} = k_{\mathrm{B}}T_0\left\{\frac{2}{\sqrt{\alpha k_{\mathrm{B}}T_0}}\frac{e^{-1/\alpha k_{\mathrm{B}}T_0}}{\sqrt{\pi}\,\mathrm{erfc}\left(\frac{1}{\sqrt{\alpha k_{\mathrm{B}}T_0}}\right)} - \frac{2}{\alpha k_{\mathrm{B}}T_0}\right\}. \tag{3.39}$$

For large values of α, the asymptotic behaviour of the effective temperature is given by

$$k_{\mathrm{B}}T_{\mathrm{eff}} \approx \sqrt{\frac{4k_{\mathrm{B}}T_0}{\pi\alpha}} = \sqrt{\frac{4k_{\mathrm{B}}T_0 m\Omega\Gamma_0}{\pi\eta}}. \tag{3.40}$$

Hence, at low friction, the effective temperature decreases as $\sqrt{\Gamma_0}$ and inversely proportional to $\sqrt{\eta}$.

3.4 Experimental results

In this section we present the main experimental results: linear dependence of the trap stiffness on optical power, linear dependence of the damping coefficient on pressure and parametric feedback cooling down to $T_{\mathrm{eff}} \sim 50\mathrm{mK}$.

3.4.1 Power dependence of trap stiffness

We first consider the particle's dynamics with the feedback loop deactivated. For small oscillation amplitudes, the particle experiences a harmonic trapping potential with a trap stiffness $\mathrm{k_{trap}}$, which is a linear function of

P. In the paraxial and dipole approximations (small particle limit, weak focusing) the *transverse* trap stiffness is calculated as

$$\mathrm{k}_{\mathrm{trap}}^{(x)} = \alpha'_{\mathrm{eff}} E_0^2 / \mathrm{w}_0{}^2, \tag{3.41}$$

where ${E_0}^2 \propto P$ is the field intensity at the focus, λ is the wavelength, w_0 the field confinement (beam waist) and $\alpha_{\mathrm{eff}}{}'$ is the particle polarisability. A similar expression holds for the *longitudinal* trap stiffness (for details see chapter 2). For the parameters used in our experiments we find that the particle's oscillation frequency in x direction is $f_0^{(x)} = (\mathrm{k}_{\mathrm{trap}}/m)^{1/2}/(2\pi) = 120\,\mathrm{kHz}$. For the axial oscillation frequency we find $f_0^{(z)} = 37\,\mathrm{kHz}$ and for the y direction we measure $f_0^{(y)} = 134\,\mathrm{kHz}$. The different oscillation frequencies in x and y directions originate from the asymmetry of the laser focus (c.f. section 2.2). The linear dependence of the trap stiffness on laser power has been verified for all three directions and is shown in Fig. 3.3(a). In Fig. 3.3(b) we show the spectral densities of the x, y, and z motions recorded at a pressure of $P_{\mathrm{gas}} = 6.3\,\mathrm{mBar}$.

3.4.2 Pressure dependence of damping coefficient

Once a particle has been trapped, the interaction with the background gas thermalises its energy with the environment and, according to the fluctuation-dissipation theorem, damps the particle's motion with the rate Γ_0 in Eq. (3.1). From kinetic theory we find that [Li et al., 2011; Beresnev et al., 1990]

$$\Gamma_0 \;=\; \frac{6\pi\eta a}{m}\frac{0.619}{0.619+\mathrm{Kn}}(1+c_K)\;, \tag{3.42}$$

where $c_K = 0.31\mathrm{Kn}/(0.785 + 1.152\mathrm{Kn} + \mathrm{Kn}^2)$, η is the viscosity coefficient of air and $\mathrm{Kn} = \bar{l}/a$ is the Knudsen number. When the mean free path $\bar{l} \propto 1/P_{\mathrm{gas}}$ is much larger than the radius of the particle, Γ_0 becomes proportional to P_{gas}. Fig. 3.4 shows the measured value of Γ_0 for all three directions as a function of pressure. For a pressure of $P_{\mathrm{gas}} = 10^{-5}\,\mathrm{mBar}$ we measure a damping of $\Gamma_0\,/\,2\pi = 10\,\mathrm{mHz}$, which corresponds to a quality

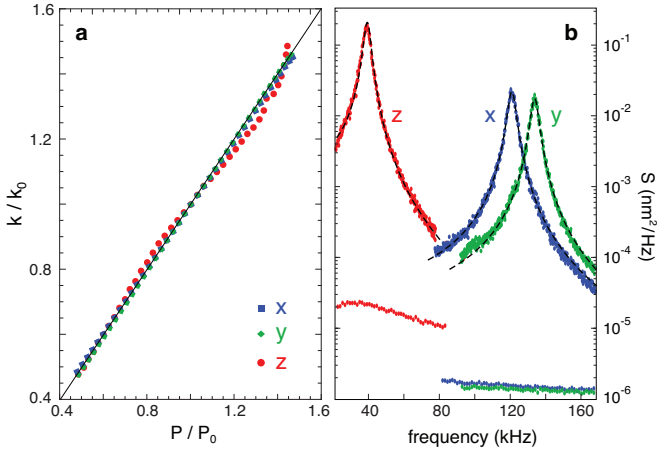

Figure 3.3: **Trap stiffness and spectral densities**. **(a)** *Normalized trap stiffness in the x, y, and z directions as a function of normalised laser power. Dots are experimental data and the solid line is a linear fit.* **(b)** *Spectral densities of the x, y, and z motions. The trapped particle has a radius of $a = 69\,nm$ and the pressure is $P_{\mathrm{gas}} = 6.3\,mBar$. The spectral separation of the resonances makes it possible to feedback-cool the trapped particle with a single laser beam. The resonance frequencies are $f_0 = 37\,kHz$, $120\,kHz$ and $134\,kHz$, respectively. The dashed curves are fits according Eq. (3.43) and the data on the bottom correspond to the noise floor.*

factor of $Q = 10^7$, a value that is higher than the quality factors achieved with clamped oscillators [Poot and van der Zant, 2012]. In ultrahigh vacuum ($P_{\mathrm{gas}} = 10^{-9}$ mBar), the quality factor will reach values as high as $Q \sim 10^{11}$.

3.4.3 Effective temperature

Activation of the parametric feedback loop gives rise to additional damping $\delta\Gamma$ and a frequency shift $\delta\Omega$. The resulting spectral line shapes are defined

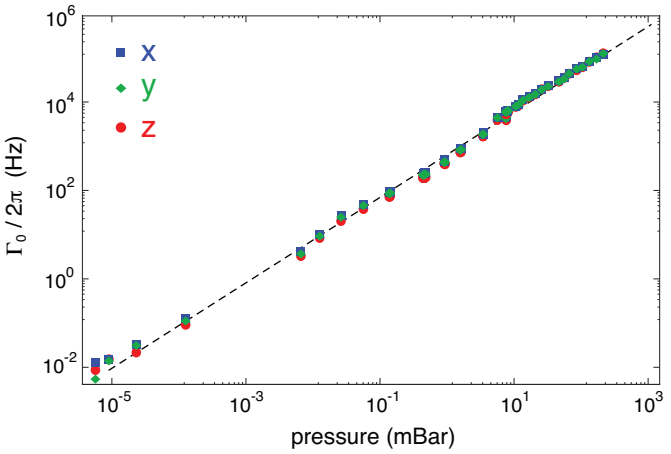

Figure 3.4: **Damping rate as a function of gas pressure.** *The damping rate Γ_0 decreases linearly with pressure P_{gas}. The dashed line is a fit according to Eq. (3.42).*

by the power spectral density $S_q(\Omega)$, which follows from Eq. (3.1) as

$$\begin{aligned} S_q(\Omega) &= \int_{-\infty}^{\infty} \langle q(t)\, q(t-t') \rangle \, \mathrm{e}^{-i\Omega t'} \, dt' \\ &= \frac{\Gamma_0 \, k_B T_0 \,/\, (\pi m)}{([\Omega_0 + \delta\Omega]^2 - \Omega^2)^2 + \Omega^2 [\Gamma_0 + \delta\Gamma]^2} \,. \end{aligned} \tag{3.43}$$

Integrating both sides over Ω yields the mean square displacement

$$\langle q^2 \rangle \;=\; \langle q(0)\, q(0) \rangle \;=\; \frac{k_B T_0}{m(\Omega_0 + \delta\Omega)^2} \, \frac{\Gamma_0}{\Gamma_0 + \delta\Gamma} \,. \tag{3.44}$$

According to the equipartition principle, the effective temperature T_{eff} follows from $k_B T_{\mathrm{eff}} = m(\Omega_0 + \delta\Omega)^2 \langle q^2 \rangle$. Considering that $\delta\Omega \ll \Omega_0$ we obtain

$$T_{\mathrm{eff}} \;=\; T_0 \, \frac{\Gamma_0}{\Gamma_0 + \delta\Gamma} \,, \tag{3.45}$$

where T_0 is the equilibrium temperature in the absence of the parametric feedback ($\delta\Gamma = 0$). Thus, the temperature of the oscillator can be raised or lowered, depending on the sign of $\delta\Gamma$ in Eq. (3.45).
Note that (3.45) differs from the previously derived expression (3.39). While the latter is exact, the former is only approximately valid because under the action of feedback the particle is not in a true thermodynamic equilibrium but rather in a steady state. In the phase space distribution the term depending on the squared energy $E(q,p)^2$ causes correlations between q and p that are absent in thermal equilibrium.

The experimental results of parametric feedback cooling are shown in Fig. 3.5, which depicts the dependence of the effective temperature T_{eff} on pressure. Following the theoretical prediction (3.39), the effective temperature scales as $\Gamma_0^{1/2}$ for constant feedback gain η. At $P_{\text{gas}} \sim 4 \times 10^{-4}$mBar the feedback gain is increased. This results in a sudden drop of the effective temperature. For lower pressures the gain is held constant again.

The cooling action of the feedback loop competes with reheating due to collisions with air molecules, ultimately setting a minimum achievable temperature for each pressure value. Since the area under the line shape defined in Eq. (3.43) is proportional to T_{eff}, feedback cooling not only increases the linewidth but also lowers the signal amplitude until it reaches the noise floor. Nevertheless, we are able to reach temperatures of $T_{\text{eff}} \sim 50\,\text{mK}$ while maintaining the particle in the trap.

3.5 Towards the ground state

The here introduced trapping and cooling technique represents an important step towards ground state cooling. In the quantum limit, a mechanical oscillator exhibits discrete states separated in energy by $\hbar(\Omega_0 + \delta\Omega) \sim \hbar\Omega_0$. The mean thermal occupancy is

$$\langle n \rangle = \frac{k_B T_{\text{eff}}}{\hbar\Omega_0} \,. \tag{3.46}$$

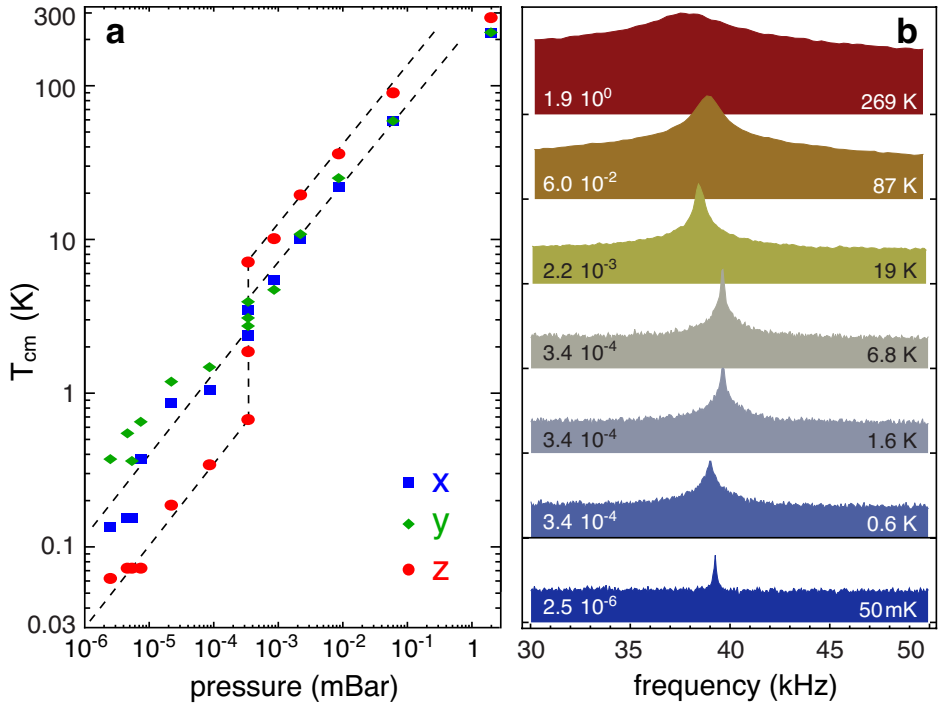

Figure 3.5: **Parametric feedback cooling.** **(a)** *Dependence of the center-of-mass temperature T_{eff} on pressure. The cooling rate (the slope of the dashed lines) is similar for the different directions x, y and z. The feedback gain has been increased at a pressure of $\sim 0.3\,\mu$Bar causing a kink in the curves.* ***(b)*** *Spectra of the z motion evaluated for different pressures and temperatures T_{eff}. The area under the curves is proportional to T_{eff}. The numbers in the figure indicate the pressure in mBar.*

In order to resolve the quantum ground state we require $\langle n \rangle < 1$. For a 120 kHz oscillator, this condition implies $T_{\text{eff}} \sim 6\,\mu$K. According to equation (3.45), a low pressure implies a low damping rate and thus, extrapolating Fig. 3.5a, we find that this temperature will be reached at ultrahigh vacuum (10^{-11} mBar), provided that the particle oscillation can be measured

and the feedback remains operational. Alternatively, lower occupancy can be reached at higher pressures by an increase of the feedback gain. Laser power noise introduces fluctuations in the trap stiffness and therefore in the mechanical oscillation frequency. We believe that the resulting random phase error in the feedback loop is the current limiting factor in cooling. This phase error can be minimised by using background suppression and laser stabilisation techniques [Seifert et al., 2006]. The noise floor in our measurements is currently $1.2\,\mathrm{pm}/\sqrt{\mathrm{Hz}}$.

In feedback cooling, the particle's position has to be measured in order to operate the feedback loop. Measurement uncertainty of x, y, and z introduced by shot-noise therefore limits the lowest attainable temperature T_{eff}. The measurement accuracy is fundamentally limited by the standard quantum limit, which follows from the uncertainty principle.

3.5.1 The standard quantum limit

Photons that scatter off the particle carry information about it's position, which sub-sequentially can be read out via photo detection. The signal improves with the number of photons N_{ph} that interact with the particle. However, even for an ideal detector the stochastic arrival of photons adds an uncertainty to the measurement. For a laser beam with N_{ph} photons the uncertainty in photon number due to shot noise is $\Delta n = \sqrt{N_{\mathrm{ph}}}$. Thus the momentum uncertainty is $\Delta p = \sqrt{N_{\mathrm{ph}}}\hbar k_q$, where k_q is the wavevector of the scattered photon into direction q. From the uncertainty principle $\Delta q \Delta p \geq \hbar/2$ it follows that the position uncertainty is $\Delta q = 1/(2\sqrt{N_{\mathrm{ph}}}k_q)$. Therefore, the position measurement improves as $\sim 1/\sqrt{N_{\mathrm{ph}}}$ with the number of photons. On the other hand, due to the momentum uncertainty $\Delta p \propto \sqrt{N_{\mathrm{ph}}}$, the finite probability to excite the mechanical oscillator increases with the number of photons. Consequently, the uncertainty in the measured energy

$$\Delta E = 1/2(m\Omega_0^2 \Delta q^2 + \Delta p^2/m), \tag{3.47}$$

consists of two terms, measurement uncertainty and measurement back-action, respectively. The standard quantum limit is achieved when the

measurement uncertainty is minimized, that is when both terms contribute equally.

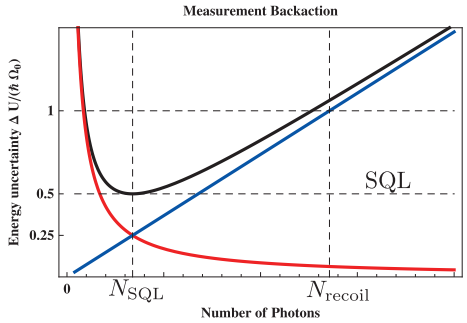

Figure 3.6: **Measurement backaction.** *The standard quantum limit is reached when the measured position uncertainty is equal to the momentum imparted by the photons that carry the information about the position. The red curve shows the measurement uncertainty, the blue curve the measurement back-action and the black curve shows the sum of the two.*

3.5.2 Recoil heating

Evidently, the measurement uncertainty Δq can be reduced by increasing the signal power at the detector, for example by higher laser power or by using a larger particle size a and hence a larger scattering cross-section $\sigma_{\text{scatt}} = k^4|\alpha|^2/(6\pi\epsilon_0^2)$. However, strong scattering introduces recoil heating, which destroys the coherent particle motion.

In general, photon recoil is a small effect since the photon momentum is small compared to the momentum of the mechanical oscillator. However, at very low pressures, collisions of the oscillator with air molecules becomes negligible and photon recoil becomes the dominating decoherence process. To understand the effect of recoil from our previous discussion of measurement backaction, consider the number of photons needed to add one quantum of mechanical energy $\hbar\Omega_0$ to the oscillator. The recoil energy of a single photon emitted in direction q is given by $\hbar^2 k_q^2/2m$, where m is

the mass of the oscillator. Therefore, $N_{\mathrm{recoil}} = 2m\hbar\Omega_0/\hbar^2 k_q^2$ photons need to interact with the oscillator to add one quantum of mechanical energy. The number of photons that are scattered by a particle with scattering cross section σ_{scatt} within a time interval Δt is $N_{\mathrm{scat}} = P_{\mathrm{scat}}\Delta t/\hbar\omega$, where $P_{scat} = \sigma_{\mathrm{scatt}} I_0$ is the scattered power and $I_0 = P_{\mathrm{in}}/\sigma_{\mathrm{focus}}$ is the intensity at the laser focus.
From this the time $\Delta t_{\mathrm{recoil}}$ it takes to scatter N_{recoil} photons follows as

$$\Gamma_{\mathrm{recoil}} = 1/\Delta t_{\mathrm{recoil}} = \left[\frac{\hbar^2 k_q^2/2m}{\hbar\Omega_0}\right]\left[\frac{I_0\,\sigma_{\mathrm{scatt}}}{\hbar\omega}\right]. \tag{3.48}$$

Finally, to obtain the recoil rate in direction q, we consider the probability of observing a photon scattered in this direction. Since for a sub-wavelength particle, the scattered light featuers a dipolar radiation pattern, the probability of observing a particle in direction $\{\theta, \phi\}$ is $P(\theta, \phi) = \frac{3}{8}\sin^2\theta$. Thus, the contribution to recoil from all photons in direction q is

$$k_q^2 = \int_0^{2\pi}\int_0^{\pi} P(\theta,\phi)(\mathbf{k}\cdot\mathbf{n}_q)^2\,\sin\theta \mathrm{d}\theta\mathrm{d}\phi = k^2 \begin{cases} 2/5 & \text{q=y,z} \\ 1/5 & \text{q=x} \end{cases}, \tag{3.49}$$

where $\mathbf{k}\cdot\mathbf{n}_q$ is the projection of the wavevector

$$\mathbf{k} = (k_x, k_y, k_z) = k(\cos\theta, \sin\theta\cos\phi, \sin\theta\sin\phi). \tag{3.50}$$

in direction q. Here, x is the direction of polarisation of the incident electric field. Since a dipole doesn't radiate along the direction of polarisation also the recoil along the direction of polarisation is reduced.

3.5.3 Detector bandwidth

We continue the discussion to gain some insight into the limits of the detection. Consider the number of photons available to detect the particle position q. As before $N_{\mathrm{scat}} = P_{\mathrm{scat}}\Delta t/\hbar\omega$, where now the measurement time $\Delta t = 1/B$ is given by the bandwidth of the detector B. The position uncertainty is then easily found as

$$\Delta q \geq \sqrt{\hbar c\lambda B/(8\pi P_{\mathrm{scat}})}. \tag{3.51}$$

For our experimental values $a = 70nm$, $P_{\text{in}} = 100\,\text{mW}$, $\lambda = 1064\,\text{nm}$ and $B = 300\,\text{kHz}$, we find that $\approx 10^8$ photons are scattered and that the position uncertainty is $\Delta q \approx 6.3\,\text{pm}$, which is of the order of the zero point motion. Our experimental parameters are therefore close to the optimum. From (3.51), one might argue that the position uncertainty can be further improved by simply reducing the bandwidth of the detector. However, for the feedback to work we need to be sensitive to changes in the amplitude $q_0(t)$ and phase $\phi(t)$ of the particle motion[1]. Classically, the particle trajectory can be written as $q(t) = q_0(t)\sin(\Omega_0 t + \phi(t))$, where $q_0(t)$ and $\phi(t)$ are slowly varying functions that vary over timescales of the order of $\sim 1/\Gamma_{\text{decoher.}}$. In other words, the maximum time $\Delta t_{\text{meas.}}$ we have for the measurement of $q(t)$ is the time over which $q(t + \Delta t_{\text{meas.}})$ is correlated with $q(t)$.

In ultrahigh vacuum, the dominant decoherence process is recoil heating and therefore $\Gamma_{\text{decoher.}} = \Gamma_{\text{recoil}} \propto P_{\text{scat.}}$. Using $B \approx \Gamma_{\text{recoil}}$, the position uncertainty (3.51) becomes independent of power. This is again a manifestation of the uncertainty principle, which tells us that the minimum uncertainty in the position measurement is given by the zero point motion.

Ultimately, we are interested in the number of coherent oscillations that can be observed. Employing the expression for the trap stiffness derived in section 2.3, we find that the number

$$N_{\text{osc}} = \frac{\Omega_0}{2\pi\Gamma_{\text{recoil}}} \propto 1/(ka)^3 \tag{3.52}$$

of coherent oscillations also does not depend on power. Hence, we can choose the power high enough to make photon shot noise the dominant noise source.

In conclusion, we have shown that neither the number of coherent oscillations, nor the minimum position uncertainty depend on power. As a consequence, we can work in a regime where the measurement uncertainty is only limited by photon shot noise. In that case, the minimum measurement

[1] Actually for the feedback we only need to know the right phase. However, the amplitude gives us the energy.

uncertainty is achieved by a detector with bandwidth $B \approx \Gamma_{\mathrm{recoil}}$. The discussion highlights the tradeoff between measurement uncertainty and recoil heating. A nanoparticle of size of $a \sim 70\,\mathrm{nm}$ is a good compromise between the two limiting factors. Notice that Γ_{recoil} and the photon scattering rate differ by a factor of $\sim 10^{-9}$, and hence most of the scattered photons do not alter the center-of-mass state of the particle. The possibility of observing the particle without destroying its quantum coherence is a critical advantage over atomic trapping and cooling experiments. Finally, parametric cooling should work even without continuously tracking $q(t)$ as long as the frequency and the phase of the center-of-mass oscillation are known.

3.6 Conclusion

We have demonstrated that an optically trapped nanoparticle in high vacuum can be efficiently cooled in all three dimensions by a parametric feedback scheme. The parametric feedback makes use of a *single* laser beam and is therefore not limited by alignment inaccuracies of additional cooling lasers. Theoretical considerations show that center-of-mass temperatures close to the quantum ground state are within reach. To fully exploit the quantum coherence of a laser-trapped nanoparticle, parametric feedback cooling can be combined with *passive* dynamical back-action cooling [Kippenberg and Vahala, 2007], for example by use of optical cavities [Chang et al., 2010; Romero-Isart et al., 2010; Kiesel et al., 2013] or electronic resonators [Teufel et al., 2011]. The results shown here also hold promise for ultrasensitive detection and sensing [Geraci et al., 2010]. The ultrahigh quality factors and small oscillation amplitudes yield force sensitivities on the order of $10^{-20}\,\mathrm{N}/\sqrt{Hz}$ [Stipe et al., 2001], which outperforms most other ultrasensitive force measurement techniques by orders of magnitude, and can find applications for the detection of single electron or nuclear spins [Rugar et al., 2004], Casimir forces and vacuum friction, phase transitions [Lechner et al., 2013], and non-Newtonian gravity-like forces [Geraci et al., 2010].

CHAPTER 4

Dynamics of a parametrically driven levitated particle

A prerequisite for applications of a nanomechanical resonator, such as sensing, is a thorough understanding of the resonator response to changes in its environment. The dynamic response to different external stimuli and the oscillator parameters can be characterised by applying a known external force. In this chapter we use parametric modulation of the trapping potential to excite an optically levitated particle in high vacuum and analyze its response for a range of different excitation modalities.

4.1 Introduction

For large oscillation amplitudes the particle motion is governed by a (Duffing) nonlinearity. This nonlinearity is common to most nanomechanical oscillators, which are ideal systems to explore nonlinear dynamical behaviour, as they exhibit high mechanical quality (Q) factors fast response times and fairly low drift and can be easily excited into the nonlinear regime [Unterreithmeier et al., 2010]. The response of a nonlinear oscillator exhibits characteristic phenomena such as multistability, hysteresis and discontinu-

ities. They can be exploited in a wide range of applications ranging from precision frequency measurement [Aldridge and Cleland, 2005], signal amplification via stochastic resonance [Almog et al., 2007], to mass sensing [Buks and Yurke, 2006]. They also allow for studying classical to quantum transitions [Katz et al., 2007].

Here we study the response of an optically levitated nanoparticle in high vacuum subject to parametric excitation. This allows to drive the particle oscillation in a controlled manner and thereby to fully characterise it's properties. A thorough understanding of the dynamics of an optically trapped particle in high vacuum is a necessary condition for ultimate control (i.e. ground state cooling) and many of the aforementioned applications.

4.2 Theoretical background

Fig. 4.1 shows a schematic of the experimental configuration. A single nanoparticle is trapped at the focus of the laser beam by means of the

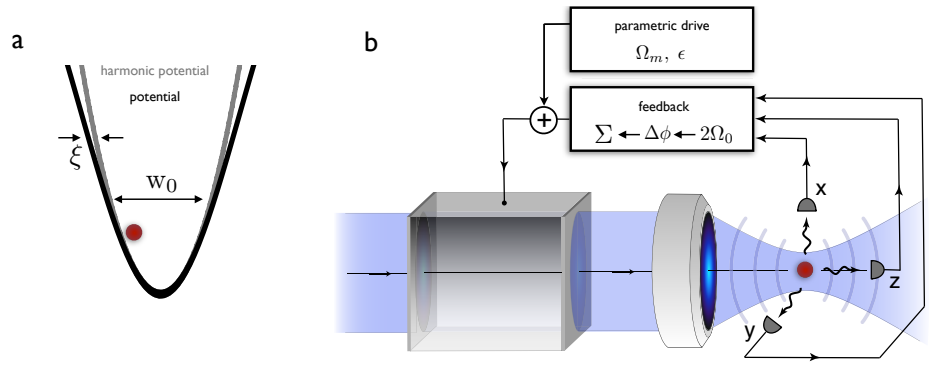

Figure 4.1: **Experimental configuration.** *(a) For large oscillation amplitudes, the optical potential is anharmonic. The anharmonicity gives rise to the Duffing term in* (5.3)*. (b) The center-of-mass motion of a laser-trapped nanoparticle is cooled with a parametric feedback loop. In addition to the feedback signal an external modulation is applied to drive the particle.*

optical gradient force and cooled parametrically by a feedback loop. In addition to the feedback signal, we apply a modulation at frequency Ω_m and modulation depth ϵ.

4.2.1 Equation of motion

The particle motion consists of three modes, each corresponding to a spatial oscillation along one of the three symmetry axes of the optical intensity distribution. For large oscillation amplitudes, the modes couple through cubic nonlinearities in the optical force (c.f. chapter 2). However, under the action of feedback cooling, the effective thermal amplitude $q_\mathrm{eff} = \left(2k_\mathrm{B}T_\mathrm{eff}\,/m\Omega_0^2\right)^{1/2}$ of the particle oscillation is much smaller than the size of the trap. As a consequence, coupling between the modes is negligible and the particle dynamics is well described by a one-dimensional equation of motion:

$$\ddot{q} + \Gamma_0\dot{q} + \Omega_0^2\left[1 + \underbrace{\epsilon\cos\left(\Omega_\mathrm{m}t\right)}_{\text{parametric drive}} + \underbrace{\Omega_0^{-1}\Gamma_0 q\dot{q}}_{\text{feedback}} + \underbrace{\xi q^2}_{\text{Duffing term}}\right]q = \frac{\mathcal{F}_\mathrm{fluct}}{m} \approx 0. \tag{4.1}$$

The damping Γ_0 can be controlled by the pressure of the vacuum chamber. In addition, the third term depends on several experimental parameters which allow us to control the particle motion as follows

- The *prefactor* is proportional to the mean optical power and defines the oscillation frequency Ω_0 of the trapped particle.
- *Parametric driving* with modulation depth ϵ and modulation frequency Ω_m allows to drive the particle motion. As we will see in the following sections, the most interesting phenomena occur when Ω_m is close to twice the natural frequency Ω_0 of the particle.
- *Nonlinear damping* is due to parametric feedback cooling. Without parametric drive ($\epsilon = 0$), the nonlinear damping reduces the effective thermal energy from T_0 to T_eff (c.f. chapter 3). It is important to

note that feedback cooling reduces the effective thermal motion in all three spatial directions. In contrast, parametric driving only excites the mode which fulfils the condition $\Omega_{\mathrm{m}} \approx 2\Omega_0$.

- The *Duffing* nonlinearity is due to the shape of the optical potential (c.f. chapter 2). It becomes significant when the particle's oscillation amplitude is comparable to the beam waist w_0.

The right hand side of equation (5.3) is a stochastic force due to random collisions with residual air molecules and therefore depends on pressure. The fluctuation-dissipation relation links the strength of the thermal force to the damping $\langle \mathcal{F}_{\mathrm{fluct}}(t)\, \mathcal{F}_{\mathrm{fluct}}(t') \rangle = 2m\Gamma_0\, k_{\mathrm{B}} T_{\mathrm{eff}}\, \delta(t-t')$. Under typical experimental conditions $Q = \Omega_0/\Gamma_0 \gg 1$. Hence, the stochastic force is much weaker than the nonlinear terms and the parametric driving and can be neglected in the description of the particle dynamics.

4.2.2 Overview of modulation parameter space

The response of the particle to the external modulation depends on the parameters of the external driving force ϵ and Ω_{m}, respectively. In the following we consider resonant and non-resonant parametric driving. For the former the condition $\Omega_{\mathrm{m}} \approx 2\Omega_0$ holds, whereas for the latter this condition is violated. In addition, for resonant driving, we can also distinguish between excitation below and excitation above threshold, respectively.

Resonance condition

Fig. 4.2 shows the frequency resolved particle response at 6 mBar as a function of modulation frequency Ω_{m} for fixed modulation depth ϵ. Modulation at frequency Ω_{m} produces sideband frequencies at $|\Omega_0 \pm \Omega_m|$ (red dashed lines). For very low modulation frequencies, the overlap of the sidebands leads to an apparent broadening of the resonance peak (lower inset Fig. 4.2). In high vacuum, the resonances and consequently also the modulation sidebands become sharper and we can resolve higher order sidebands (c.f. section 4.3.4). When the lower sideband $\Omega_m - \Omega_0$ becomes resonant with the

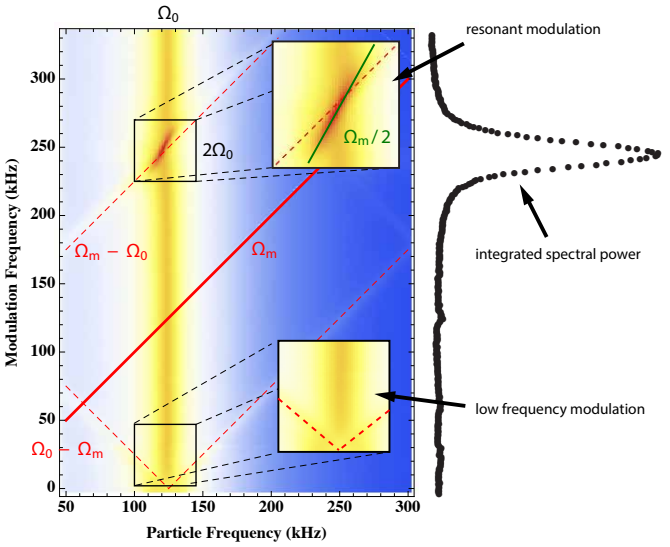

Figure 4.2: **Parametric excitation overview.** *The main figure shows the power spectral density (horizontal axis) of the x-mode ($\Omega_0 \sim 125$kHz) as a function of modulation frequency Ω_m (vertical axis). Modulation at frequency Ω_m (red solid line) produces sideband frequencies at $|\Omega_0 \pm \Omega_m|$ (red dashed lines). When the lower sideband $\Omega_m - \Omega_0$ becomes resonant with the particle resonance Ω_0, energy is transferred from the sideband to the particle (upper inset). This results in a increase of the particle energy and frequency locking to the external modulation (green solid line, c.f. section 4.3.1). The total particle energy is obtained by integration of the power spectral density. The integrated power spectral density as a function of modulation frequency is show as black data points to the right. On resonance, the thermal noise is parametrically amplified.*

particle resonance Ω_0, energy is transferred from the sideband to the parti-

cle (upper inset Fig. 4.2). This results in a increase of the particle energy. The total particle energy is obtained by integration over the power spectral density (black data points to the right).

Threshold condition

Near the resonance (upper inset Fig. 4.2), we distinguish between weak and strong resonant driving. For weak modulation, the Duffing term in Eq. (5.3) can be neglected and we observe parametric amplification of the thermal noise (black data points Fig. 4.2). However, if the driving is sufficiently strong, the Duffing term in Eq. (5.3) becomes important and the system makes a transition reminiscent of a phase transition. The particle motion changes from thermal (incoherent) motion to sustained (coherent) oscillations with a fixed frequency with respect to the external modulation.

In the parameter phase space near resonance, the stability condition (c.f. chapter 4.3.2)

$$\epsilon < \frac{2}{Q}\sqrt{1 + Q^2\left(2 - \Omega_\mathrm{m}/\Omega_0\right)^2}, \tag{4.2}$$

maps out a tongue shaped region (Arnold tongue), which is shown as grey area in Fig. 4.3a. Typically $Q \gg 1$ and the exact condition (4.2) is well approximated by

$$|\delta_\mathrm{m}| < \epsilon/2 \tag{4.3}$$

shown as dashed diagonal lines, where $\delta_\mathrm{m} = 2 - \Omega_\mathrm{m}/\Omega_0$ is the normalised modulation detuning. The particle response to the external modulation for a given set of parameters $\{\epsilon, \Omega_\mathrm{m}\}$ depends on the phase space trajectory of the two control parameters ϵ and Ω_m. For simplicity we consider only cases where one of the two is held constant while the other is varied. In that case we can distinguish five cases

I. *Frequency up and down sweeps above threshold.* The response exhibits hysteresis and is discontinuous when the resonance is approached from below (c.f. section 4.4.3).

II. *Amplitude up and down sweeps below resonance.* The response exhibits hysteresis and is discontinuous when the threshold is crossed from below and from above (c.f. section 4.4.4).

III. *Amplitude up and down sweeps above resonance.* The response does not exhibit hysteresis and is continuous (c.f. section 4.4.4).

IV. *Approaching the instability region.* The frequency of the thermal mode is pulled towards the sideband (c.f. section 4.3.3).

V. *Below threshold.* The response does not exhibit hysteresis and is continuous. The regime below the onset of self-sustained oscillations can be used for mechanical parametric amplification and thermal noise squeezing [Rugar and Gruetter, 1991; Lifshitz and Cross, 2009]. (c.f. Fig. 4.2 black data points - at the parametric resonance the thermal noise is parametrically amplified).

4.2.3 Secular perturbation theory

Within the resonance region (grey tongue shaped region Fig. 4.3), we are interested in solutions $q(t)$ that are slow modulations of the linear resonance oscillations. Therefore, we introduce a dimensionless slow time scale $T = \kappa\Omega_0 t$ and displacement amplitude $A(T)$. With the slowly varying envelope approximation (SVEA)

$$q = \frac{q_0}{2} A e^{i\Omega_0 t} + c.c. \tag{4.4a}$$

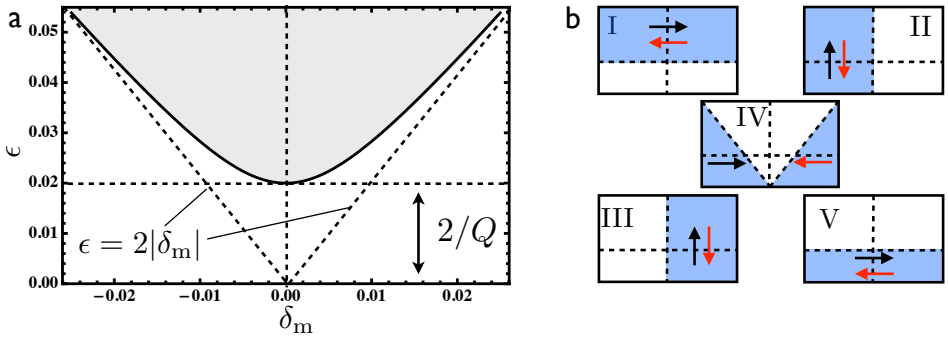

Figure 4.3: **Near resonant modulation: parameter space.** *(a) The stability condition* (4.2) *divides the the* ϵ-Ω_m *plane into two regions, thermal motion (white) and self oscillation (grey). If the stability condition is fulfilled, the particle oscillation amplitude is given by it's effective temperature. Above threshold (grey), the particle enters a regime of coherent oscillations in sync with the external modulation. The modulation depth threshold on resonance depends on the* Q *factor (here* 50*). The dashed diagonal lines correspond to* $Q = \infty$*. This is a good approximation for typical configurations, where the* Q*-factor is larger than* 10^4*. (b) The particle response depends on the value and the trajectory of the two control parameters* ϵ *and* δ_m*.*

and using $\dot{A} = \frac{dA}{dt} = \Omega_0 \kappa \frac{dA}{dT}$ we get:

$$\dot{q} = \Omega_0 \frac{q_0}{2} \left[\kappa \frac{dA}{dT} + iA \right] e^{i\Omega_0 t} + c.c. \tag{4.4b}$$

$$\ddot{q} = \Omega_0^2 \frac{q_0}{2} \left[\kappa^2 \frac{d^2A}{dT^2} + i2\kappa \frac{dA}{dT} - A \right] e^{i\Omega_0 t} + c.c. \tag{4.4c}$$

$$q^2 \dot{q} = \frac{q_0^3}{8} \Omega_0 \left[2\kappa |A|^2 \frac{dA}{dT} + i|A|^2 A + \kappa A^2 \frac{dA^*}{dT} \right] \tag{4.4d}$$

$$\times e^{i\Omega_0 t} + c.c. \tag{4.4e}$$

$$q^3 = \frac{3q_0^3}{8} |A|^2 A e^{i\Omega_0 t} + c.c. \tag{4.4f}$$

$$\epsilon \cos(\Omega_m t) q = \frac{\epsilon q_0}{4} A^* e^{(\Omega_m - 2\Omega_0)t} e^{i\Omega_0 t}, \tag{4.4g}$$

where c.c. stands for complex conjugate and we dropped small corrections from fast oscillating terms. For a consistent expansion [Villanueva et al., 2013; Lifshitz and Cross, 2009], we apply the rescaling

$$\tilde{\gamma_0} = \frac{\Gamma_0}{\Omega_0 \kappa};\ \tilde{\eta} = \frac{\eta}{\xi};\ \tilde{\epsilon} = \frac{\epsilon}{\kappa} \tag{4.5}$$

with scale factors $\kappa = \Gamma_0/\Omega_0 = Q^{-1}$ and $q_0^2 = \kappa/\xi$. Plugging (4.4) into (5.3) yields

$$\begin{aligned}
&\Omega_0^2 \frac{q_0}{2}\left[\kappa^2 \frac{d^2A}{dT^2} + i2\kappa\frac{dA}{dT} - A\right] e^{i\Omega_0 t} \\
&+ \tilde{\gamma}_0 \kappa \Omega_0^2 \frac{q_0}{2}\left[\kappa\frac{dA}{dT} + iA\right] e^{i\Omega_0 t} \\
&+ \Omega_0^2 \frac{q_0}{2} A e^{i\Omega_0 t} \\
&+ \frac{q_0}{8}\Omega_0^2 \tilde{\eta}\kappa\left[2\kappa|A|^2\frac{dA}{dT} + i|A|^2 A + \kappa A^2 \frac{dA^*}{dT}\right] e^{i\Omega_0 t} + c.c. \\
&+ \Omega_0^2 \kappa \frac{3q_0}{8}|A|^2 A e^{i\Omega_0 t} + c.c. \\
&+ \frac{\tilde{\epsilon} q_0}{4}\kappa A^* e^{-i(\delta\Omega_m - 2\Omega_0)t}\, e^{i\Omega_0 t} = 0
\end{aligned} \tag{4.6}$$

Dropping higher order terms $\mathcal{O}(\kappa^2)$ and fast oscillating terms we arrive at

$$\frac{dA}{dT} = -\frac{\tilde{\gamma}_0}{2}A - \frac{1}{8}\tilde{\eta}|A|^2 A + i\frac{3}{8}|A|^2 A + i\frac{\tilde{\epsilon}}{4}A^* e^{-i\tilde{\delta}_{\mathrm{m}} T}, \tag{4.7}$$

where $\tilde{\delta}_{\mathrm{m}} = \delta_m/\kappa$ is the rescaled normalised detuning $\delta_m = (2 - \Omega_{\mathrm{m}}/\Omega_0)$. To get rid of the phase factor in (4.7), we substitute $A = \tilde{A}\exp(-iT\tilde{\delta}_{\mathrm{m}}/2)$. This gives

$$\frac{d\tilde{A}}{dT} = -\frac{\tilde{\gamma}_0}{2}\tilde{A} + i\frac{\tilde{\delta}_{\mathrm{m}}}{2}\tilde{A} - \left[\frac{1}{8}\tilde{\eta} - i\frac{3}{8}\right]|A|^2\tilde{A} + i\frac{\tilde{\epsilon}}{4}\tilde{A}^*. \tag{4.8}$$

4.2.4 Steady state solution

In the following we investigate the steady state solution A_0, which satisfies $\frac{d}{dT}A = 0$. Aside from the trivial solution $A_0 = 0$, the non-trivial steady state solution $A_0 = a_0 e^{-i\phi}$ of (4.8) is given by

$$\frac{d}{dT}A_0 = -i\left[-i\left(\frac{\tilde{\gamma}_0}{2} + \frac{1}{8}\tilde{\eta}a_0^2\right) - \left(\frac{\tilde{\delta}_\mathrm{m}}{2} + \frac{3}{8}a_0^2\right)\right] a_0 e^{-i\phi} + i\frac{\tilde{\epsilon}}{4}a_0 e^{i\phi} = 0, \tag{4.9}$$

where

$$\tilde{\gamma}_0 + \frac{1}{4}\tilde{\eta}a_0^2 = -\frac{\tilde{\epsilon}}{2}\sin 2\phi, \tag{4.10}$$

$$\tilde{\delta}_\mathrm{m} + \frac{3}{4}a_0^2 = -\frac{\tilde{\epsilon}}{2}\cos 2\phi. \tag{4.11}$$

Thus, a_0 and ϕ are given as the solutions to

$$\phi = \frac{1}{2}\tan^{-1}\left(\frac{\tilde{\gamma}_0 + \frac{1}{4}\tilde{\eta}a_0^2}{\tilde{\delta}_\mathrm{m} + \frac{3}{4}a_0^2}\right) \tag{4.12}$$

and

$$\left[\tilde{\gamma}_0 + \frac{1}{4}\tilde{\eta}a_0^2\right]^2 + \left[\tilde{\delta}_\mathrm{m} + \frac{3}{4}a_0^2\right]^2 = \frac{\tilde{\epsilon}^2}{4}. \tag{4.13}$$

Fig. 4.4 shows the amplitude solution

$$a_0^2 = \left[(\tilde{\eta}/4)^2 + (3/4)^2\right]^{-1} \times \left(-\left[\tilde{\gamma}_0\tilde{\eta} + 3\tilde{\delta}_\mathrm{m}\right]/4 \pm \sqrt{\left[(\tilde{\eta}/4)^2 + (3/4)^2\right]\tilde{\epsilon}^2/4 - \left[\tilde{\eta}\tilde{\delta}_\mathrm{m}/4 - 3\tilde{\gamma}_0/4\right]^2}\right) \tag{4.14}$$

as a function of detuning δ_m. Note that the solution with the negative sign corresponds to the unstable mode.

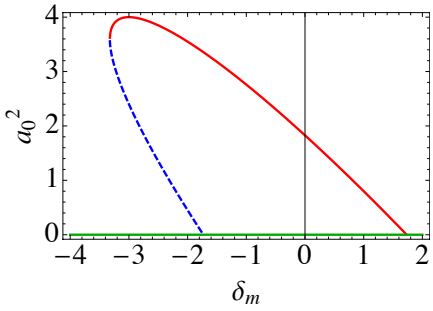

Figure 4.4: The three steady state solutions for different detuning. The parameters are $\tilde{\gamma}_0 = 1$, $\tilde{\eta} = 1$,$\tilde{\epsilon} = 4$.

4.3 Dynamics below threshold (linear regime)

To find the equation of motion for small perturbations δA from equilibrium, we make the ansatz $\tilde{A} = A_0 + \delta A$ and plug it into (4.8). Linearization around the trivial solution $A_0 = 0$ yields

$$\frac{d}{dT}\delta A = \left(-\frac{\tilde{\gamma}_0}{2} + i\frac{\tilde{\delta}_\mathrm{m}}{2}\right)\delta A + i\frac{\tilde{\epsilon}}{4}\delta A^*.$$

Writing $\delta A = r \exp i\phi$, we find the equations of motion for the amplitude and the phase of the parametrically driven oscillator.

$$\dot{r} = -\frac{\tilde{\gamma}_0}{2}r + \frac{\tilde{\epsilon}}{4}\sin(2\phi)r, \tag{4.15a}$$

$$\dot{\phi} = \frac{\tilde{\delta}_\mathrm{m}}{2} + \frac{\tilde{\epsilon}}{4}\cos(2\phi). \tag{4.15b}$$

Equation (4.15b) is known as the Adler equation. It is this equation that explains the steady state, and in fact also the transient, injection-locking behaviour of a harmonic oscillator with an external signal [Siegman, 1986].

4.3.1 Injection locking

According to the Adler equation (4.15b), a steady-state locked oscillation ($\dot{\phi} = 0$) has a fixed phase relative to the external drive

$$\phi_{\mathrm{ss}}(\tilde{\delta}_{\mathrm{m}}) = \frac{1}{2}\cos^{-1}\left(-\frac{\tilde{\delta}_{\mathrm{m}}}{\tilde{\epsilon}/2}\right). \tag{4.16}$$

The phase lag changes from $+\pi/4$ to $-\pi/4$ as $\tilde{\delta}_{\mathrm{m}}$ is tuned from $-\tilde{\epsilon}/2$ to $\tilde{\epsilon}/2$ and changes sign at $\tilde{\delta}_{\mathrm{m}} = 0$. The Adler equation depends only on ϕ and we can integrate it

$$\tan(\frac{\phi}{2}) = \frac{\tilde{\delta}_{\mathrm{m}}}{\Delta\Omega_b} + \frac{\tilde{\epsilon}/2}{\Delta\Omega_b}\tanh\left(\frac{\Delta\Omega_{\mathrm{b}}\,(t-t_0)}{2}\right). \tag{4.17}$$

Here, t_0 incorporates the initial conditions and the beat frequency is given by $\Delta\Omega_{\mathrm{b}} = \sqrt{(\tilde{\epsilon}/2)^2 - \tilde{\delta}_{\mathrm{m}}^2}$ [Knünz et al., 2010]. Note that $\tilde{\epsilon}/2 > |\tilde{\delta}_{\mathrm{m}}|$, since we are considering the behaviour within the lock-in region. From (4.17) it follows that for an injected signal within the lock-in region, the phase will always pull-in smoothly towards the steady-state value given by (4.16). This is easily seen by considering a small perturbation $\delta\phi$ from the steady state $\phi = \phi_{\mathrm{ss}} + \delta\phi$. From (4.15b) we find

$$\delta\dot{\phi} = -\left[\left(\frac{\tilde{\epsilon}}{2}\right)^2 - \tilde{\delta}_{\mathrm{m}}^2\right]\delta\phi \tag{4.18}$$

Consequently, the phase relaxes exponentially to its steady state value.

4.3.2 Linear instability

Using the steady state value ϕ_{ss} in (4.15a), we find that the amplitude grows exponentially at a rate

$$g_{\mathrm{L}} = -\frac{\tilde{\gamma}_0}{2} + \frac{1}{2}\left[\left(\frac{\tilde{\epsilon}}{2}\right)^2 - \tilde{\delta}_{\mathrm{m}}^2\right] \tag{4.19}$$

If the total gain becomes positive, the oscillation amplitude grows exponentially until saturation due to nonlinearities. Note that the stability condition (4.2) is an immediate consequence of (4.19):

$$\epsilon < \frac{2}{Q}\sqrt{1 + Q^2\delta_{\mathrm{m}}^2}.$$

At the threshold detuning δ_{th} this becomes an equality. Since for high Q δ_{th} depends only on the modulation depth ϵ, measuring the slope of δ_{th} as a function of the external modulation $\epsilon_{\mathrm{V}} = c_{\mathrm{V}}\epsilon$ is a way to calibrate the modulation depth ϵ, where c_{V} is the calibration factor.

4.3.3 Frequency pulling

Let us now consider the case where the modulation frequency is close to but still outside the lock-in range, that is $|\tilde{\epsilon}| < |\tilde{\delta}_{\mathrm{m}}|$. The beat frequency is now defined as $\Delta\Omega_{\mathrm{b}} = \sqrt{\tilde{\delta}_{\mathrm{m}}^2 - (\tilde{\epsilon}/2)^2}$ and the hyperbolic tangent of (4.17) becomes a trigonometric tangent:

$$\tan(\frac{\phi}{2}) = \frac{\tilde{\delta}_{\mathrm{m}}}{\Delta\Omega_b} + \frac{\tilde{\epsilon}/2}{\Delta\Omega_b}\tan\left(\frac{\Delta\Omega_{\mathrm{b}}\,(t - t_0)}{2}\right). \tag{4.20}$$

From this it follows that the oscillation signal consist of a new primary carrier component with a pulled frequency [Siegman, 1986]

$$\Omega = \Omega_{\mathrm{m}} - \Omega_0 + \sqrt{(\Omega_{\mathrm{m}} - 2\Omega_0)^2 - \Omega_0\,(\epsilon/2)^2}. \tag{4.21}$$

Fig. 4.5a shows the power spectral density (PSD) for different modulation frequencies. As the lower sideband $\Omega_{\mathrm{m}} - \Omega_0$ approaches the lock in region, the particle oscillation frequency is pulled towards the sideband. In Fig. 4.5b, the oscillator is injection locked and only one resolution limited component is left. Figure 4.5c shows a quantitative analysis of frequency pulling which is in good agreement with (4.21).

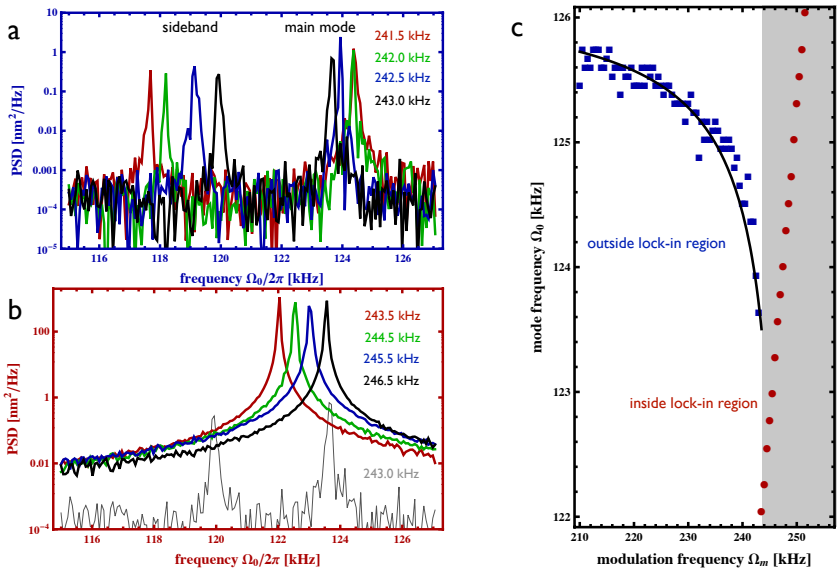

Figure 4.5: **Frequency pulling.** *When the sideband* $\Omega_{\mathrm{m}} - \Omega_0$ *approaches the main mode* Ω_0*, the main mode is pulled toward the sideband. (a) PSD for modulation frequencies below the lock-in region. (b) PSD for modulation frequencies within the lock-in region. Note that the vertical scale is different from (a). For comparison a PSD from outside the lock-in region is shown in grey. (c) The frequency of the main mode as a function of modulation frequency. The grey region mark the lock-in region. The black line is a fit to* (4.21)*. Here, the pressure is* $P_{\mathrm{gas}} = 1.9 \times 10^{-5}\,\mathrm{mBar}$ *and the modulation depth is* $\epsilon = 0.04$*.*

4.3.4 Off-resonant modulation (low frequency)

A modulation at a frequency much smaller than the particle oscillation $\Omega_{\mathrm{m}} \ll \Omega_0$ does not affect the particle energy $k_{\mathrm{B}}T_{\mathrm{eff}}$. However, the oscillation frequency is a slowly varying function of time. Hence, the particle position is of the form

$$q(t) \approx q_{\mathrm{eff}} \cos\left(\Omega_0 \left[1 + \frac{\epsilon}{2}\cos\left(\Omega_{\mathrm{m}} t\right)\right] t\right). \tag{4.22}$$

Using the identity

$$e^{ia\cos(b)} = J_0(a) + 2\sum_{k=1}^{\infty} i^k J_k(a)\cos(kb), \tag{4.23}$$

we find that the power spectral density of the particle position exhibits sidebands at $\Omega_0 \pm n\Omega_\mathrm{m}$ ($n = 1, 2, \dots$). The strength of the sidebands depends on the modulation depth ϵ and modulation frequency Ω_m.
Fig. 4.6 shows the particle PSD as a function of modulation frequency for $\epsilon = 24 \times 10^{-3}$. We can distinguish the five lowest sidebands. For small modulation depth only the lowest sidebands contribute and they become dimmer as the modulation frequency increases. The presence of sidebands in the spectrum allows us to understand the parametric resonance condition $\Omega_\mathrm{m} \approx 2\Omega_0$. The condition is satisfied when the sideband $\Omega_\mathrm{m} - \Omega_0$ approaches a particle resonance. This allows for resonant energy transfer from the sideband to the particle. Thus, the energy of the resonant mode increases.

Off-resonant modulation can also lead to phase noise. If the modulation is not at a single frequency but broadband, the sidebands of all the frequency components overlap. Consequently, the spectrum exhibits a single peak which is broader than the natural linewidth Γ_0. This kind of broadening is known as phase noise [Cleland and Roukes, 2002] and can be caused by laser intensity fluctuations which are predominantly at low frequencies.

4.4 Dynamics above threshold (nonlinear regime)

As we have seen in section 4.3.2 the oscillation amplitude grows large for driving above threshold. The following section considers the particle dynamics in the nonlinear regime.

For comparison with the experimental data we convert (4.14) back to

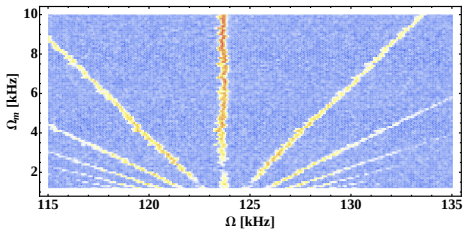

Figure 4.6: **Low frequency modulation.** *For modulation frequencies much smaller than the particle oscillation frequency, the PSD of the particle position exhibits sidebands. The modulation depth is* $\epsilon = 24 \times 10^{-3}$.

physical quantities

$$q^2 = \frac{-1}{\eta\delta_{\mathrm{th}}^2}\left[3\frac{\xi}{\eta}\delta_m + Q^{-1} - \sqrt{\epsilon^2\delta_{\mathrm{th}}^2 - \delta_m^2 + 3\frac{\xi}{\eta}Q^{-2}\left(2Q\delta_m - 3\frac{\xi}{\eta}\right)}\right]$$
$$\approx \frac{-1}{\eta\delta_{\mathrm{th}}^2}\left[3\frac{\xi}{\eta}\delta_m - \sqrt{\epsilon^2\delta_{\mathrm{th}}^2 - \delta_m^2}\right], \tag{4.24}$$

where

$$\delta_{\mathrm{th}} = \sqrt{9\xi^2 + \eta^2}\,/2\eta\,. \tag{4.25}$$

The approximation holds for $Q \gg 1$. This is the case under typical experimental conditions and for simplicity we assume that $Q \to \infty$ from here on. Note that we have dropped the amplitude solution with the negative sign, since it belongs to the unstable solution.

4.4.1 Nonlinear frequency shift

Additionally, typically $\xi \gg \eta$ (c.f. Eq. 5.3) and we can further approximate $\delta_{\mathrm{th}} \approx 3\xi\,/2\eta$ and

$$q^2 \approx -\frac{4}{3\xi}\left[\delta_{\mathrm{m}} + \epsilon/2\right]. \tag{4.26}$$

For weak driving at nonzero detuning δ_{m}, the second term becomes negligible and we obtain $\Omega_{\mathrm{m}}/2 = \Omega_0 + 3\xi q^2/8$. Recalling that $\Omega_{\mathrm{m}}/2$ is the particle

oscillation frequency of the locked particle, the nonlinear frequency shift is given by

$$\Delta\Omega_{\mathrm{NL}} = 3\xi q^2/8. \tag{4.27}$$

4.4.2 Nonlinear instability

From (4.24) it follows that a solution only exists if

$$\epsilon^2\delta_{\mathrm{th}}^2 - \delta_m^2 > 0. \tag{4.28}$$

This condition plays a similar role as the linear stability condition (4.2). However, whereas (4.2) gives the parameter range for which the linear system is stable, (4.28) is the stability condition for the nonlinear solution.

4.4.3 Modulation frequency sweeps

In the following we consider the particle response for fixed modulation depth ϵ as the modulation frequency Ω_{m} is swept over the resonance of the x motion at $2\Omega_0 \sim 250\mathrm{kHz}$.

Fig. 4.7a shows a map of the particle energy as Ω_{m} is increased from 240 kHz to 255 kHz, for values of ϵ ranging from 1×10^{-3} to 24×10^{-3}. For off resonant modulation, the particle energy remains at $T_{\mathrm{eff}} = \frac{m\Omega_0^2}{2k_{\mathrm{B}}}x^2 \approx 17\,\mathrm{K}$. For modulation frequencies within the lock-in range, the particle energy increases significantly. The lock-in region, as predicted by the linear stability condition (4.3), is shown as black dashed lines.

Fig. 4.7b shows the frequency sweep performed in the opposite direction. The high frequency threshold is still given by (4.3). However, the low frequency threshold is pushed towards lower frequencies (white dashed line) in agreement with the nonlinear stability condition (4.28).

Fig. 4.7c shows a horizontal cut through subfigures a and b indicated by black dotted lines ($\epsilon = 22\times10^{-3}$). When the instability region is approached from below, the energy stays at T_{eff} until the threshold is reached. Above threshold, the motion locks to the external modulation and the energy is given by (4.24). As the modulation frequency is further increased,

parameter	method 1	method 2	combined
η [μm^{-2}]	6.1 ($\pm$4%)	7.2 ($\pm$7%)	6.3 ($\pm$3%)
ξ[μm^{-2}]	$-$10.2 ($\pm$4%)	$-$9.5 ($\pm$6%)	$-$10.0 ($\pm$3%)

Table 4.1: **Nonlinear coefficients** *extracted from experimental data of frequency sweeps. Method 1 extracts the parameters from the threshold values corresponding to figures 4.7d,e. Method 2 extracts the parameters from a fit to individual scans corresponding to figures 4.7c.*

the particle energy makes a smooth transition to the off-resonant energy. Conversely, when the instability region is crossed from above, the energy smoothly increases as predicted by (4.24). Because of the (negative) Duffing nonlinearity, the increasing oscillation amplitude, pushes the effective resonance frequency $\Omega_{\text{eff.}} = \Omega_0 \left(1 + \frac{3}{8}\xi x^2\right)$ to lower frequencies. Since the lock-in region depends on the resonance frequency, it is also dragged along.

From (4.28), we find the lower threshold frequency

$$\Omega_{\text{th}} = \Omega_0 \left[2 - \epsilon\delta_{\text{th}}\right]. \tag{4.29}$$

where the particle energy falls back to the off-resonant value. At this modulation frequency the particle's oscillation amplitude reaches it's maximum value

$$x^2_{\text{max}} = \frac{-3\xi}{\eta^2\delta_{\text{th}}}\epsilon. \tag{4.30}$$

Fig. 4.7d,e show the threshold frequency Ω_{th} and energy $E_{\text{max}} = \frac{1}{2}m\Omega_0^2 x^2_{\text{max}}$ together with their respective fits. From the fits and equations (4.29) and (4.30) we extract the nonlinear coefficients. Alternatively we obtain the nonlinear coefficients from a fit of (4.24) to the modulation downward sweep (blue dashed curve Fig. 4.7c). The coefficients obtained with the two methods are listed in table 4.1.

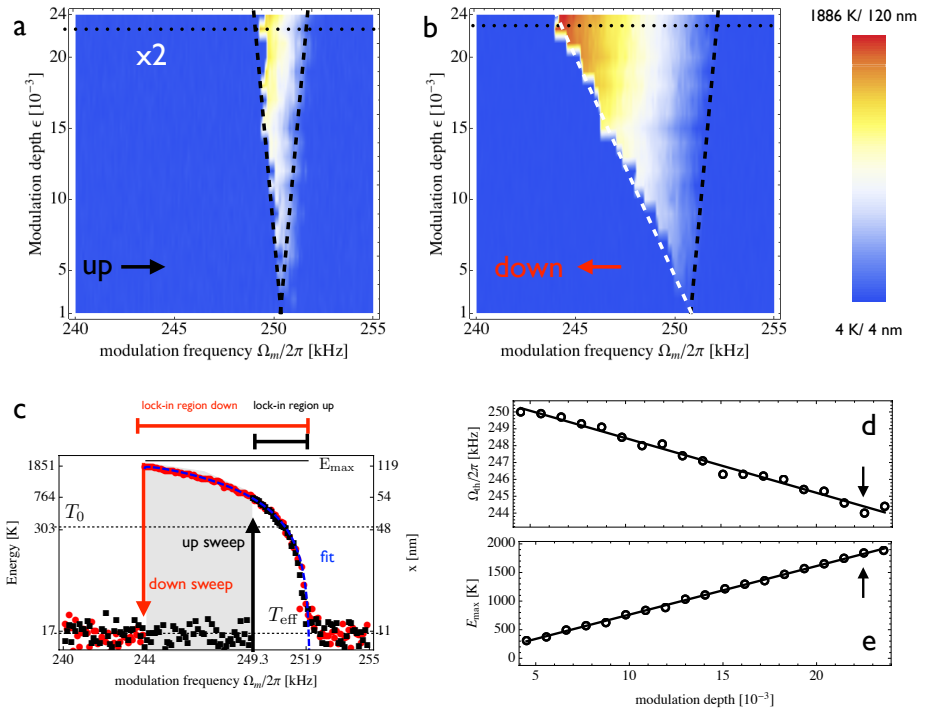

Figure 4.7: **Frequency Sweep.** *(a) For fixed modulation depth and increasing modulation frequency, the particle energy maps out a triangular region in the ϵ-Ω_m plane. The black dashed line marks the instability threshold* (4.3)*. (b) For decreasing modulation frequency, the lower instability threshold is pushed to lower frequencies. (c) Up and down sweep at $\epsilon = 22 \times 10^{-3}$ (black dotted line in subfigures a and b). The blue dashed line is a fit to* (4.24)*. (d) Threshold modulation depth (white line in subfigure b) and (e) threshold particle energy as a function of modulation depth. The black arrows mark the data points which correspond to subfigure c.*

4.4.4 Modulation depth sweeps

Next, we consider the situation where the modulation depth ϵ is varied while the modulation frequency Ω_m is kept constant at a frequency close to

resonance $\Omega_\mathrm{m} \approx 2\Omega_0$.

Fig. 4.8a shows a map of the particle energy as ϵ is increased from 0.1×10^{-3} to 28×10^{-3}, for values of Ω_m ranging 247.5 kHz to 252.5 kHz. For the modulation depth given by the stability condition (4.3), the particle energy remains at $T_\mathrm{eff} \approx 15K$. For modulation depths above threshold (black dashed lines), the particle energy increases to the value given by (4.24).

Fig. 4.8b shows the modulation depth sweep performed in the opposite direction. For modulation frequencies above resonance, the threshold is still given by (4.3). In contrast, for modulation frequencies below resonance, the particle continues to oscillate with high amplitude even if the modulation depth is reduced significantly below the threshold value of the upward sweep down to a minimum value ϵ_min (white dashed line).

Fig. 4.8c shows a vertical cut through subfigures a and b indicated by black dotted lines ($\Omega_\mathrm{m} = 248.3\,\mathrm{kHz}$). When the modulation depth is increased from zero, the particle energy stays at T_eff until the threshold $\epsilon = 2\delta_\mathrm{m}$ is reached. Above threshold, the motion locks to the external modulation and the energy increases suddenly to the value given by (4.24). As the modulation depth is further increased the particle energy increases slowly. Conversely, when the modulation depth is reduced, the energy decreases. However, the energy doesn't fall back to T_eff at $\epsilon = 2\delta_\mathrm{m}$ but continues to follow the solution (4.24) until the minimum modulation depth

$$\epsilon_\mathrm{th} = \frac{\delta_m}{\delta_\mathrm{th}}. \tag{4.31}$$

At this modulation depth the amplitude is given by

$$x^2_\mathrm{min} = \frac{-3\xi}{\eta^2\delta_\mathrm{m}}\epsilon^2_\mathrm{th}. \tag{4.32}$$

Fig. 4.7d,e show the threshold modulation depth ϵ_th and energy $E_\mathrm{min} = \frac{1}{2}m\Omega_0^2 x^2_\mathrm{min}$ together with their respective fits. From the fits and equations (4.31) and (4.32) we extract the nonlinear coefficients. Alternatively, we obtain the nonlinear coefficients from a fit of (4.24) to the modulation depth

parameter	method 1	method 2	combined
η [μm^{-2}]	4.3 ($\pm$7%)	14 ($\pm$59%)	4.3 ($\pm$7%)
ξ[μm^{-2}]	$-$16.0 ($\pm$6%)	$-$25 ($\pm$54%)	$-$16.0 ($\pm$6%)

Table 4.2: **Nonlinear coefficients** *extracted from experimental data. Method 1 extracts the parameters from the threshold values corresponding to figures 4.8d,e. Method 2 extracts the parameters from a fit to individual scans corresponding to figure 4.8c.*

downward sweep (blue dashed curve Fig. 4.7c). The coefficients obtained with the two methods are listed in Table 4.2.

4.4.5 Relative phase between particle and external modulation

So far, we merely considered the energy of the particle oscillation while a resonant modulation is applied. In the following we also consider the relative phase between the particle oscillation and the external modulation. As expected from the previous analysis, we find that there exists a fixed phase relation.

Fig. 4.9 shows the phase of the particle with respect to the external modulation as the modulation frequency is scanned across the resonance. For a modulation frequency downward sweep, the particle's resonance frequency is pulled toward the modulation sideband and the relative phase locks to

$$\phi_0 = \phi(\delta_\mathrm{m} = 0) = -\frac{1}{2}\tan^{-1}\left(\frac{\eta}{3\xi}\right) \tag{4.33}$$

even before the upper modulation threshold $(2 + \epsilon/2)\Omega_0$ is reached. Upon crossing the lock-in region, the phase grows continuously to its maximum

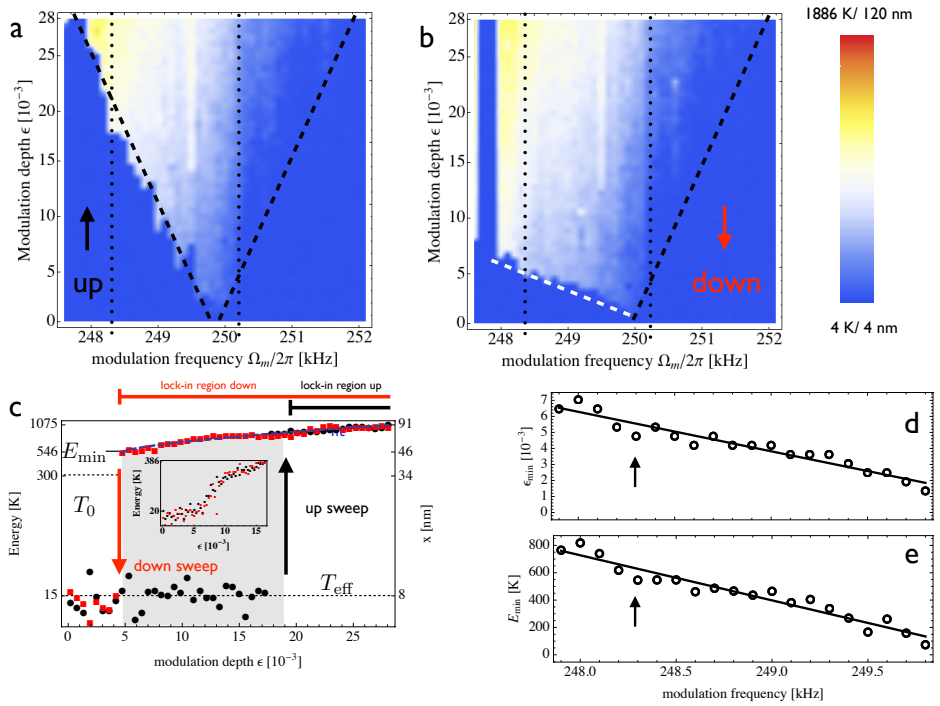

Figure 4.8: **Modulation depth sweep.** *(a) For fixed modulation frequency and increasing modulation depth, the particle energy maps out a triangular region in the ϵ-Ω_m plane. The black dashed line marks the instability threshold* (4.3)*. (b) For decreasing modulation depth, the lower instability threshold is pushed to lower modulation depth. (c) Up and down sweep at $\Omega_\mathrm{m} = 248.3\,\mathrm{kHz}$ (black dotted line in subfigures a and b). The blue dashed line is a fit to* (4.24)*. The inset shows up and down sweep above resonance, where no hysteresis is observed. (d) Threshold modulation depth (white line in subfigure b) and (e) threshold particle energy as a function of modulation depth. The black arrows mark the data points which correspond to subfigure c.*

value[1]

$$\phi_{\mathrm{th}} = \phi(\delta_{\mathrm{m}} = \delta_{\mathrm{th}}) = \frac{1}{2}\tan^{-1}\left(\frac{3\xi}{\eta}\right). \tag{4.34}$$

This transition is accompanied by an increase in particle energy. For the nonlinear parameters obtained from a fit of the particle amplitude to (4.24), the theoretical phase according to (4.12) is shown as blue dashed line. When the modulation frequency is swept in the opposite direction, the particle phase locks to ϕ_{th} as soon as the downward threshold modulation frequency $\Omega_{\mathrm{th}}^{(\mathrm{down})}$ is reached even though the amplitude remains at it's off-resonant value. The phase stays at ϕ_{th} until the upper $\Omega_{\mathrm{th}}^{(\mathrm{up})}$ threshold is reached, where the phase jumps to the solution given by (4.12).
The high sensitivity of the phase to an external modulation over a wide range could be exploited to improve the sensitivity and bandwidth in the detection of weak periodic signals.

4.4.6 Nonlinear mode coupling

Until now, we have neglected coupling between the three spatial modes. However, for large oscillation amplitudes, the modes couple because the trap stiffness along a given direction depends on the oscillation amplitude along any direction. The trap stiffness along x is of the form (c.f. chapter 2)

$$\mathrm{k}_{\mathrm{trap}}^{(x)} = m\Omega_0^2\left(1 - \sum_{i=x,y,z}\xi_i^{(x)}x_i^2\right) \tag{4.35}$$

and respective expressions hold for the trap stiffness along y and z. Here, $\xi_x^{(x)} = \xi$ is the Duffing nonlinearity we have considered so far and $\xi_y^{(x)}$ and $\xi_y^{(x)}$ are the nonlinear coupling coefficients to y and z, respectively. To illustrate the nonlinear coupling we sweep the modulation frequency over a wide range which covers both the x and the y resonance.

[1]Note that the relative phase is periodic with periodicity of $\pi/2$. Therefore, the phase wraps around to negative values when it becomes larger than $\pi/4$

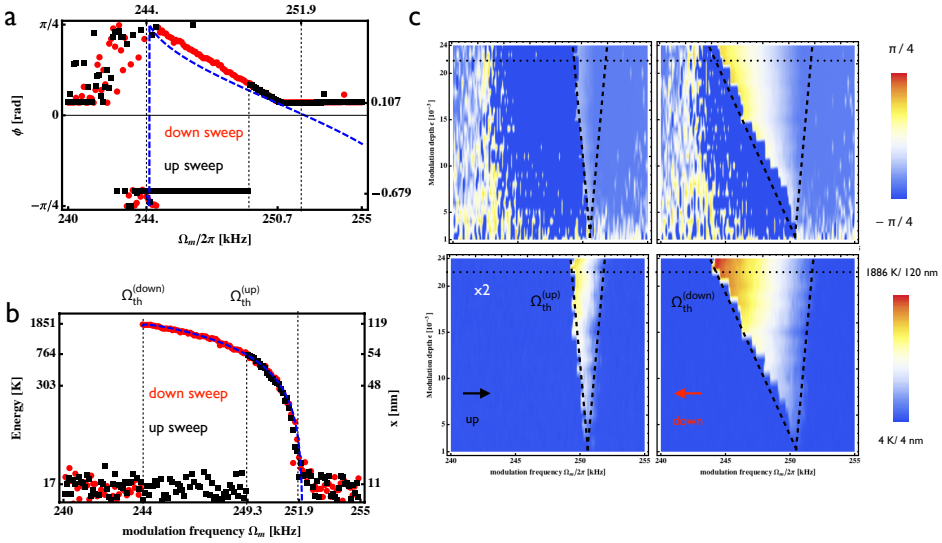

Figure 4.9: **Phase in lock-in region** *(a) Relative phase ϕ between particle oscillation and external modulation. As the lock in region is crossed from higher to lower modulation frequencies (red) the relative phase changes continuously from close to in-phase ($\phi \approx 0.1$) to out-of-phase ($\phi \approx \pi/4$). Interestingly, when the modulation frequency is increased (black), the phase locks to the external modulation as soon as $\Omega_{\mathrm{th}}^{(\mathrm{down})}$ is reached, while the amplitude remains at a low value. The blue dashed line is Eq.* (4.12) *for the parameters obtained from the amplitude fit of subfigure b. (b) The particle amplitude in the same frequency as the phase shown in subfigure a. (c) Phase map of modulation frequency up and down sweep, respectively (upper row) and corresponding amplitude maps (lower row). The amplitude maps are identical to figures 4.7a,b. The range where the phase is locked to the external modulation is larger than the range where the amplitude of the driven particle is above the background value.*

Fig. 4.10 shows a map of a modulation frequency downward sweep with modulation depth $\epsilon \sim 8 \times 10^{-3}$. The parametric modulation frequency is

reduced from 285 kHz down to 230 kHz exciting the resonances of the x and y mode, respectively. Within the lock-in range energy is transferred to the particle and the resonant mode is excited (c.f. Fig. 4.10a).

Fig. 4.10b,c show the spectra of the signals that correspond to x and y motion of the particle as a function of modulation frequency. As discussed before, when the modulation frequency is close to resonance ($\Omega_\mathrm{m} \approx 2\Omega_0$), the mode locks to the external modulation and the particle energy of the resonant mode increases, while the energy of the other mode remains at a low value. However, an analysis of the power spectral density reveals that both the frequency of the resonant mode and the frequency of the off-resonant mode are pulled to lower frequencies. This agrees with Eq. (4.35) with negative Duffing coefficients.

4.4.7 Sidebands

Aside from the oscillation at $\Omega_\mathrm{m}/2$, the resonant mode exhibits sidebands at $\Omega_\mathrm{m}/2 + \Omega_\pm$. The sidebands appear much weaker and much broader than the main peak. The origin of the sidebands can be understood from an analysis of the dynamics of small deviations from the steady state.

To find the equation of motion for small perturbations δA from equilibrium, we make the ansatz $\tilde{A} = A_0 + \delta A$ and plug it into (4.8). This yields

$$\begin{aligned}\frac{d}{dT}\delta A = &\left(-\frac{\tilde{\gamma}_0}{2} + i\frac{\tilde{\delta}_\mathrm{m}}{2} - 2\left[\frac{1}{8}\tilde{\eta} - i\frac{3}{8}\right]|A_0|^2\right)\delta A \\ &- \left[\frac{1}{8}\tilde{\eta} - i\frac{3}{8}\right]A_0^2\delta A^* + i\frac{\tilde{\epsilon}}{4}\delta A^* \end{aligned} \tag{4.36}$$

Now, making the ansatz $\delta A = e^{-i\phi}(ue^{i\omega T} + v^*e^{-i\omega T})$, we get

$$\begin{aligned}&\left(\dot{u}e^{i\omega T} + \dot{v}^*e^{-i\omega T}\right) + i\omega\left(ue^{i\omega T} - v^*e^{-i\omega T}\right) \\ &= i\frac{\tilde{\epsilon}}{4}e^{i2\phi}\left[(v-u)e^{i\omega T} + (u^*-v^*)e^{-i\omega T}\right] \\ &- \left[\frac{1}{8}\tilde{\eta} - i\frac{3}{8}\right]a_0^2\left[(u+v)e^{i\omega T} + (v^*+u^*)e^{-i\omega T}\right].\end{aligned}$$

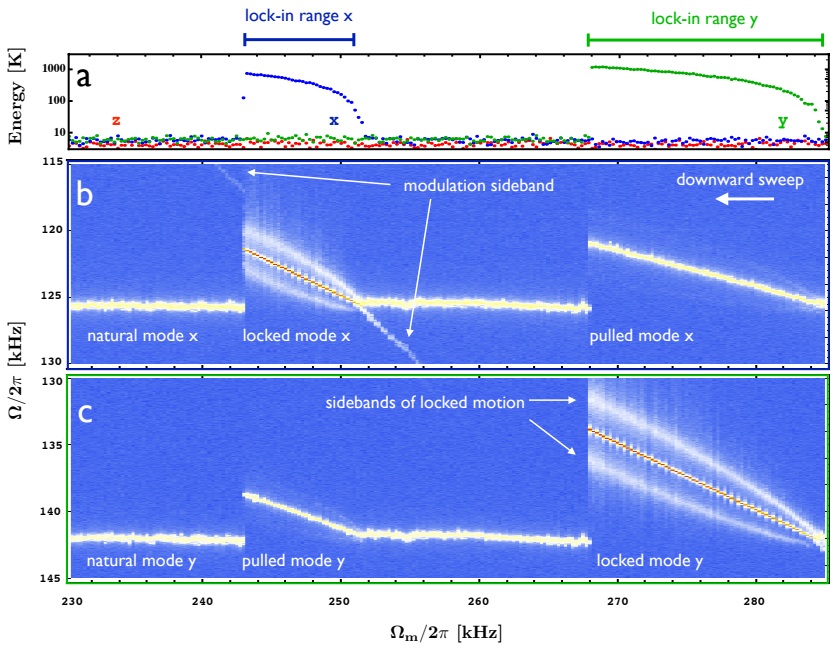

Figure 4.10: **Spectral map frequency down sweep.** *The parametric modulation frequency is reduced from 285kHz down to 230 kHz exciting the resonances of the x and y mode, respectively. Within the lock-in range energy is transferred to the particle and the resonant mode is excited. The particle oscillation of the resonant mode locks to the external modulation and oscillates at $\Omega_\mathrm{m}/2$ with modulation sidebands at $\Omega_\pm$. Here, the pressure is 1.6×10^{-4}mBar ($Q \sim 10^6$). The modulation depth is $\epsilon = 8 \times 10^{-3}$. (a) Only the mode near the lower modulation sideband $\Omega_0 \approx \Omega_\mathrm{m} - \Omega_0$ is excited. The energy of the other modes remains at T_eff. (b) PSD of x-mode on a logarithmic scale as a function of modulation frequency Ω_m. Outside the lock-in range, the mode frequency stays at it's natural value $\sim 126\,\mathrm{kHz}$. Within the lock-in range, the mode frequency is half the external modulation frequency. Within the lock-in range of the other mode, the frequency is pulled due to nonlinear coupling. However, the energy does not change. (c) PSD of y-mode as a function of modulation frequency Ω_m.*

yielding two coupled equations of motion

$$\dot{u} = -i\omega u - \left[\frac{1}{8}\tilde{\eta} - i\frac{3}{8}\right] a_0^2(u+v) - i\frac{\tilde{\epsilon}}{4}e^{i2\phi}(u-v)$$
$$\dot{v} = -i\omega v - \left[\frac{1}{8}\tilde{\eta} + i\frac{3}{8}\right] a_0^2(u+v) - i\frac{\tilde{\epsilon}}{4}e^{-i2\phi}(u-v).$$

Applying the transformation

$$\Psi = \begin{pmatrix} c \\ d \end{pmatrix} = e^{i\omega T} S^{-1} \begin{pmatrix} u \\ v \end{pmatrix}, \; S^{-1} = \begin{pmatrix} 1 & 1 \\ -i & i \end{pmatrix}, \tag{4.37}$$

this reads

$$\dot{\Psi} = H\Psi \tag{4.38}$$

with

$$H = \begin{pmatrix} -\tilde{\eta}a_0^2/4 & \tilde{\epsilon}\cos(2\phi)/2 \\ 3a_0^2/4 & \tilde{\epsilon}\sin(2\phi)/2 \end{pmatrix}.$$

Diagonalizing $\Lambda = \mathrm{diag}(\lambda_+, \lambda_-) = U^{-1}HU$ with

$$U = \begin{pmatrix} -\lambda_- - \frac{1}{4}\tilde{\eta}a_0^2 & -\lambda_+ - \frac{1}{4}\tilde{\eta}a_0^2 \\ 3a_0^2/4 & 3a_0^2/4 \end{pmatrix} \tag{4.39}$$

where

$$\lambda_\pm = -\frac{\tilde{\gamma}_0}{2} - \frac{\tilde{\eta}_0}{4}a_0^2 \pm i\sqrt{\frac{3}{4}a_0^2(\frac{3}{4}a_0^2 + \tilde{\delta}_\mathrm{m}) - \left(\frac{\tilde{\gamma}_0}{2}\right)^2} \tag{4.40}$$

are the eigenvalues of H, we find the solutions

$$\Phi = U^{-1}\Psi = \begin{pmatrix} \phi_+ \exp\lambda_+ T \\ \phi_-^* \exp\lambda_- T \end{pmatrix}, \tag{4.41}$$

where $\{\phi_+, \phi_-\}$ are determined by the initial conditions. Transforming back to the original variables

$$\begin{pmatrix} u \\ v \end{pmatrix} = e^{-i\omega T} SU\Phi, \tag{4.42}$$

we find

$$\begin{aligned}\delta A =& e^{-i\phi}\left[\left(\frac{3}{4}a_0^2+\tilde{\gamma}_0+\frac{1}{4}\tilde{\eta}a_0^2+\lambda_+\right)\phi_+ - i\left(\frac{3}{4}a_0^2-\tilde{\gamma}_0-\frac{1}{4}\tilde{\eta}a_0^2-\lambda_+\right)\phi_-\right]e^{\lambda_+ T}\\ &+e^{-i\phi}\left[\left(\frac{3}{4}a_0^2+\tilde{\gamma}_0+\frac{1}{4}\tilde{\eta}a_0^2+\lambda_-\right)\phi_-^* - i\left(\frac{3}{4}a_0^2-\tilde{\gamma}_0-\frac{1}{4}\tilde{\eta}a_0^2-\lambda_-\right)\phi_+^*\right]e^{\lambda_- T}.\end{aligned} \tag{4.43}$$

Thus, the frequencies of the modes of δA are given by (4.40) and consequently the sideband shift is

$$\Delta\Omega_\pm = \pm\sqrt{\frac{3}{4}a_0^2\left(\frac{3}{4}a_0^2+\tilde{\delta}_\mathrm{m}\right)-\left(\frac{\tilde{\gamma}_0}{2}\right)^2}. \tag{4.44}$$

Fig. 4.11 shows good agreement between the experimentally measured sideband shift of the y-mode and the theoretically expected shift (4.44).

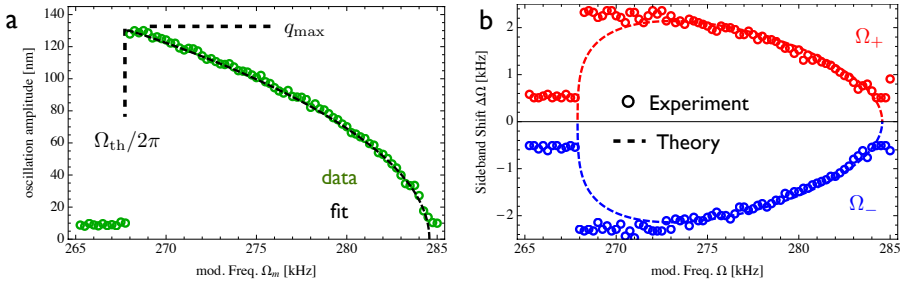

Figure 4.11: **Sidebands.** *(a) Y-mode oscillation amplitude of frequency down sweep (c.f. Fig. 4.10a). To good approximation, the nonlinear damping and nonlinear Duffing coefficient determine the cut-off frequency* Ω_{th} *and maximum amplitude* $q_{\max}$*, respectively. Fitting the experimental data to* (4.14)*, we extract the nonlinear coefficients* $\xi = -9\mu\mathrm{m}^{-2}$ *and* $\eta = 0.6\mu\mathrm{m}^{-2}$*. (b) Sidebands of y-mode as a function of modulation frequency* Ω_m*. Open circles are the experimental data and dashed lines are the theoretical curves* (4.40)*.*

4.5 Conclusions

In conclusion, we have parametrically excited an optically trapped nanoparticle well into the nonlinear regime. We have shown that each of the three individual spatial modes can be excited independently while the other modes are cooled by parametric feedback. We can measure the parameters of the nanomechanical oscillator by performing either amplitude or frequency sweeps of the external modulation. This provides a method to measure the nonlinear damping induced by parametric feedback cooling and consequently to optimise the feedback parameters.

Thus far, we have primarily focused on a one-dimensional description of the particle equation of motion. However, there remains still room for further investigation of the full three dimensional dynamics. In particular, the response to resonant (multi-frequency) driving fields is not fully understood. Beside CoM motion, the levitated dielectric particle can also rotate freely [Arita et al., 2011, 2013]. Further investigation along this line will potentially reveal valuable insights into ultimate performance limits of a levitated nanoparticle in high vacuum.

CHAPTER 5

Thermal nonlinearities in a nanomechanical oscillator

Nano- and micromechanical oscillators with high quality (Q) factors have gained much attention for their potential application as ultrasensitive detectors. In contrast to micro-fabricated devices, optically trapped nanoparticles in vacuum do not suffer from clamping losses, hence leading to much larger Q-factors. We find that for a levitated nanoparticle the thermal energy suffices to drive the motion of the nanoparticle into the nonlinear regime. First, we experimentally measure and fully characterize the frequency fluctuations originating from thermal motion and nonlinearities. Second, we demonstrate that feedback cooling can be used to mitigate these fluctuations. The high level of control allows us to fully exploit the force sensing capabilities of the nanoresonator. Our approach offers a force sensitivity of $20\,\mathrm{zN\,Hz^{-1/2}}$*, which is the highest value reported to date at room temperature, sufficient to sense ultra-weak interactions, such as non-Newtonian gravity-like forces.*

5.1 Introduction

Recent developments in optomechanics have evolved toward smaller and lighter resonators featuring high quality (Q) factors, which are important for the sensing of tiny masses [Chaste et al., 2012; Yang et al., 2006], charges [Cleland and Roukes, 1998], magnetic fields [Rugar et al., 2004] and weak forces [Stipe et al., 2001; Moser et al., 2013]. The presence of a force field or the adhesion of a small mass induces a change in the mechanical response and can be monitored by tracking either the oscillation frequency, phase or its amplitude. Ultimately, dissipation losses as well as thermomechanical noise and temperature fluctuations limit the Q-factors of clamped oscillators and consequently their sensing performance [Postma et al., 2005; Cleland and Roukes, 2002; Ekinci et al., 2004]. This can be circumvented by using an optically trapped nanoparticle in high vacuum. Indeed, the Q-factor of a levitated particle is only limited by collisions with residual air molecules and can potentially reach 10^{12} for small particles in ultra high-vacuum [Ashkin, 1971; Gieseler et al., 2012; Li et al., 2011; Romero-Isart et al., 2010; Chang et al., 2010]. In this chapter we first show that an optically trapped nanoparticle is sufficiently sensitive that thermal forces drive it out of its linear regime. Additionally, we demonstrate that feedback cooling can be used to mitigate frequency fluctuations associated with the thermal nonlinearities thereby recovering the force sensing capabilities of the oscillator.

5.2 Description of the experiment

In our experiment, a silica nanoparticle with diameter $\sim$ 75nm is trapped at room temperatue in the focal region of a tightly focused NIR laser beam (λ = 1064nm, polarized along the x-axis). The intensity near the focus of the objective (NA = 0.8) can be well approximated by Gaussian functions (c.f. Fig.5.1), defining a focal volume of $\mathrm{w}_x \times \mathrm{w}_y \times \mathrm{w}_z \approx 0.69\mu\mathrm{m} \times 0.54\mu\mathrm{m} \times 1.36\mu\mathrm{m}$ [1]. For large displacements, the optical potential

[1] estimated from numerical calculation of a highly focused beam with NA=0.8

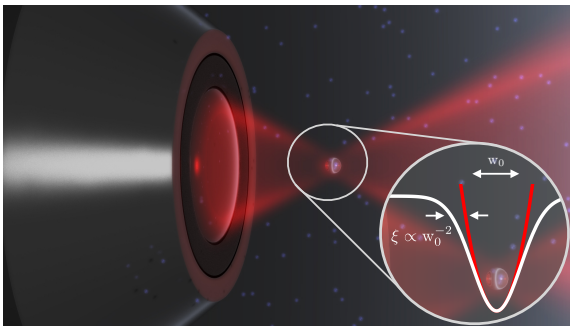

Figure 5.1: **Experimental configuration** *A silica nanoparticle is trapped by a tightly focused laser beam. Random collisions with residual air molecules drive the particle into the nonlinear regime of the potential. (inset) The focal intensity distribution forms a trap which can be approximated by a Gaussian potential (white). The deviation from a harmonic potential (red) is described by a Duffing nonlinearity.*

becomes anharmonic featuring a Duffing nonlinearity. For a Gaussian field distribution the nonlinear coefficients are given by

$$\xi_j = -2/\mathrm{w_j}^2, \tag{5.1}$$

where $\mathrm{w_i}$ is the beam waist radius or Rayleigh range. For small displacements $|q_i| \ll |\xi_j^{-1/2}|$, the nonlinearity is negligible and the three motional degrees of freedom decouple. Due to the asymmetry of the optical focus, the oscillation frequencies $\Omega_i = (k_i/m)^{1/2}$ along the three major axes are different ($\Omega_z/2\pi = 37\mathrm{kHz}$, $\Omega_\mathrm{x}/2\pi = 125\mathrm{kHz}$, $\Omega_\mathrm{y}/2\pi = 135\mathrm{kHz}$). The linear trap stiffness is given by $k_i = \alpha E_0^2/\mathrm{w_i}^2$, where E_0 is the electric field intensity at the focus. The gradient of the optical intensity distribution exerts a restoring force $F_i^{\mathrm{grad}} = -k_i \left(1 + \sum_{j=x,y,z} \xi_j q_j^2\right) q_i$ on a dipolar particle with polarizability α, that is displaced from the trap center by x_i. For a sphere of radius a and dielectric constant ϵ_p, the polarizability is $\alpha = 4\pi a^3 \epsilon_0 (\epsilon_p - 1)/(\epsilon_p + 2)$, ϵ_0 being the vacuum permittivity.

We experimentally determine the nonlinear coefficients by parametric excitation through modulation of the trapping laser at a frequency close the parametric resonance $\Omega_{\mathrm{mod}} \approx 2\Omega_i$ and find

$$(\xi_z, \xi_x, \xi_y) = (-0.98, -7.95, -10.41)\mu m^{-2}, \tag{5.2}$$

in good agreement with the values estimated from the size of the focus (5.1) (c.f. chapter 4).

5.2.1 Origin of nonlinear frequency shift

The equation of motion for each spatial degree of freedom ($i = x, y, z$) is given by

$$\ddot{q}_i + \Omega_i Q_i^{-1} \dot{q}_i + \Omega_i^2 \left(1 + \sum_{j=x,y,z} \xi_j q_j^2\right) x_i = \mathcal{F}_{\mathrm{fluct}} / m \, . \tag{5.3}$$

In the following we concentrate on a single degree of freedom and denote the corresponding resonance frequency by Ω_0 and the quality factor by Q. Random collisions with residual air molecules provide both damping $\Gamma_0 = \Omega_0 Q^{-1}$ and stochastic excitation $\mathcal{F}_{\mathrm{fluct}}$ of the trapped nanoparticle. From kinetic theory we find that the damping coefficient of a particle in a rarified gas is given by [Epstein, 1923; Chang et al., 2010]

$$\Gamma_0 = \frac{64a^2}{3m\bar{v}} P, \tag{5.4}$$

where $\bar{v} = (8k_B T/\pi\mu)^{1/2}$ is the average velocity and μ is the weight of the air molecules [O'Hanlon, 2003]. The random force $\mathcal{F}_{\mathrm{fluct}}$ is related to the damping coefficient by the fluctuation-dissipation theorem $\langle \mathcal{F}_{\mathrm{fluct}}(t) \mathcal{F}_{\mathrm{fluct}}(t') \rangle = 2m\Gamma_0 k_B T_0 \delta(t - t')$. The damping coefficient determines the frequency stability of the harmonic oscillator $\Delta\Omega_{\mathrm{L}} = \Omega_0 Q^{-1}$, and the temperature-dependent stochastic excitations determine the minimum oscillation amplitude according to $q_{\mathrm{th}} = \sqrt{2k_B T_0 / m\Omega_0^2}$. The thermal amplitude q_{th} is

usually small compared to the dimensions of the oscillator. However, for a small and hence light oscillator like our levitated nanoparticle, the thermal amplitude eventually becomes comparable to the particle size. Consequently, a proper description of the particle motion requires the inclusion of nonlinearities. The latter give rise to a frequency shift $\Delta\Omega_{\mathrm{NL}} = 3\xi\Omega_0/8\, q_{\mathrm{th}}^2$ [Dykman and Krivoglaz, 1984; Lifshitz and Cross, 2009]. In contrast to linear thermal frequency fluctuations, *nonlinear* frequency fluctuations add frequency noise but do not affect the damping.

In order to resolve the nonlinear frequency shift originating from thermal motion, the nonlinear contribution must be larger than the linear one, that is

$$\mathcal{R} = \frac{\Delta\Omega_{\mathrm{NL}}}{\Delta\Omega_{\mathrm{L}}} = \frac{3\xi Q k_B T_0}{4\Omega_0^2 m} \gg 1, \tag{5.5}$$

where T_0 is the temperature of the residual gas and k_B is Boltzmann's constant. To fulfil condition (5.5) a light and high-Q mechanical resonator is required. In our experiment, $m = 3 \times 10^{-18}$kg and $Q = 10^8$, as determined in a ring-down measurement at a pressure of $P_{\mathrm{gas}} = 0.5 \times 10^{-6}$mBar. These parameters place us well into the nonlinear regime. Importantly, the dependence of the Q-factor on pressure P_{gas} allows us to continuously tune the system between the linear and nonlinear regimes.

5.2.2 Nonlinear spectra

To demonstrate the differences between a thermally driven harmonic oscillator ($\mathcal{R} \ll 1$) and an anharmonic oscillator ($\mathcal{R} \gg 1$), we compare the particle's motion at high pressure (6 mBar) and at low pressure (1.2×10^{-2} mBar). These pressures correspond to Q-factors of 25 and 12×10^3, respectively. At high pressures (low Q) the dominant source of frequency fluctuations is linear damping $\Delta\Omega_{\mathrm{L}} = \Gamma_0$ and the power spectral density (PSD) of the particle motion features a single symmetric Lorenzian peak, whose width is equal to the linear damping coefficient Γ_0 (Fig. 5.2b). In contrast, at low pressure (high Q) nonlinear frequency fluctuations $\Delta\Omega_{\mathrm{NL}} = 3\xi\Omega_0\,/8\; q_{\mathrm{th}}^2$ dominate

and we observe an asymmetric peak that is considerably broader than what is expected for the equivalent linear oscillator. However, if we limit the observation time to time intervals $1/\Delta\Omega_{\mathrm{NL}} < \tau < 1/\Delta\Omega_{\mathrm{L}}$, we find a clean oscillation with an almost constant amplitude, corresponding to a narrow and symmetric peak in the frequency domain. For large oscillation amplitudes the peak appears down-shifted, consistent with the measured negative Duffing nonlinearity. Consequently, for observation times $\gg 1/\Delta\Omega_{\mathrm{NL}}$, the non-Lorenzian peak becomes a weighted average [Dykman et al., 1990]

$$S_{\mathrm{NL}}(\Omega) = \int \rho(E) S_{\mathrm{L}}(\Omega, E) dE, \tag{5.6}$$

over Lorenzian peaks centred at the shifted frequency $\hat{\Omega}_0(E) = \Omega_0 + 3\xi/(4m\Omega_0)\, E$ and weighted by the Gibbs distribution $\rho(E) = Z^{-1} \exp(-E/k_B T_0)$. Here, $Z = \int \rho(E) dE$ is the partition function and

$$S_{\mathrm{L}}(\Omega, E) = \frac{E}{\pi m \Omega_0^2} \frac{\Gamma_0}{\left(\Omega - \hat{\Omega}_0(E)\right)^2 + (\Gamma_0/2)^2}. \tag{5.7}$$

is the power spectral density of a harmonic oscillator with frequency $\hat{\Omega}_0(E)$ and energy E.
Note that (5.6) is valid in the low friction limit ($Q \gg 1$). An expression which holds for arbitrary $\mathcal{R}$ can be found in [Dykman and Krivoglaz, 1984].

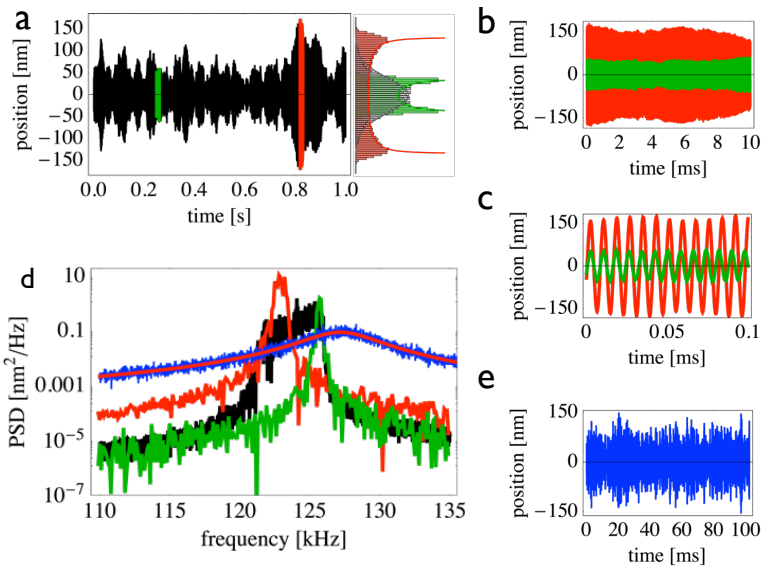

Figure 5.2: **Nonlinearity-induced frequency fluctuations** *(a) Time trace of the particle motion along x at 1.2×10^{-2} mBar. The oscillation amplitude changes randomly and the positions are normally distributed. (b,c) However, on time scales short compared to the relaxation time τ, the particle motion is sinusoidal with a constant oscillation amplitude over many cycles and has a position distribution featuring two lobes (subfigure (a) right). The part of the timetrace when the particle oscillates with a large (small) amplitude is shown in red (green). (d) From the long time trace (black) and the short time traces (red, green) we calculate the power spectral density (PSD). For short observation times we observe a Fourier limited symmetric PSD with an amplitude dependent center frequency. The overall PSD (black) results from a temporal average of the instantaneous PSDs (red, green). In contrast, the PSD of a low Q oscillator (blue) is described by a Lorentzian peak at all times (red thin line). (e) Time trace of particle motion at 6 mBar used to calculate the (blue) Lorentzian PSD in subfigure (b).*

5.3 Experimental results

In what follows we present further evidence that the observed frequency fluctuations are a consequence of thermal motion in the nonlinear optical potential. We analyze the correlations between the instantaneous frequencies and energies and we investigate the pressure dependence of the frequency fluctuations.

To quantify the frequency fluctuations, we continuously measure the instantaneous energy $E_i(t_j)$ and frequency $\Omega_i(t_j)$ of the three spatial modes ($i = x, y, z$), given by the area and the position of the maximum of the instantaneous PSDs, respectively (c.f. Fig. 5.2d). The instantaneous PSDs are calculated from position time traces $x_i^{(j)}(t)$ (where $t_j - \tau/2 < t < t_j + \tau/2$) of $\tau = 20\,\mathrm{ms}$ duration. Figs. 5.3a,b show the timetraces of the relative frequency fluctuations $\Omega_i/\langle\Omega_i\rangle$ of the three modes for high Q (low pressure) and low Q (high pressure), respectively. Fig. 5.3c shows the correlations between E_i and Ω_i as a function of pressure, calculated from 30min long time traces. The nonlinearity is conservative and, thus, doesn't change the particle energy, which is determined only by random molecule collisions. Therefore, the energy of the three degrees of freedom are uncorrelated. In contrast, a change in energy of one mode shifts the frequency of all modes (Eq. 5.3). At low pressure ($\mathcal{R} > 1$), the nonlinearities dominate and the frequency fluctuations are highly correlated. In contrast, at high pressure ($\mathcal{R} < 1$), linear damping dominates and consequently the frequencies become uncorrelated.

5.3.1 Frequency and energy correlations

In Figure 5.3d we plot the oscillator amplitude response to parametric modulation (black) and to thermal excitation (scatter plot) at a pressure of 10^{-5} mBar. Independently of the origin of the excitation, there is a linear relationship between the particle's energy and the particle's oscillation frequency. However, while the response to an excitation at a fixed frequency is sharp, the thermal response is downshifted and much broader. Indeed, according to Eq. 5.3, an average thermal excitation of the orthog-

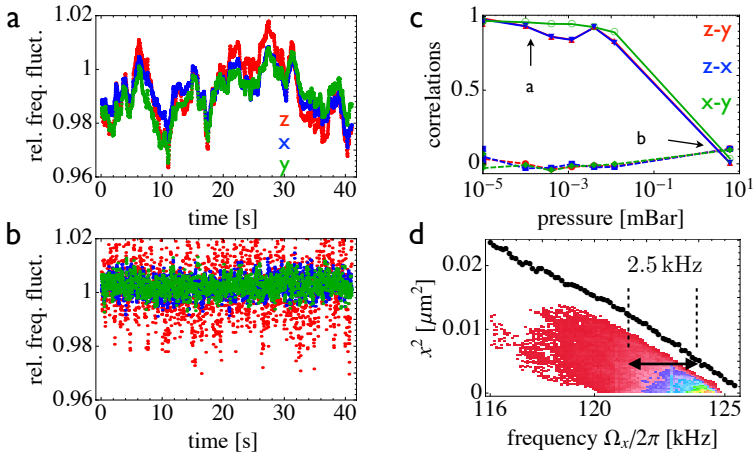

Figure 5.3: **Frequency and energy correlation.** *(a) Time traces of the instantaneous oscillation frequencies Ω_x, Ω_y and Ω_z evaluated at low pressure and (b) at high pressure. (c) Frequency and energy correlations as a function of pressure. The energies (dashed, lower curves) are uncorrelated and independent of pressure. The frequencies (solid, upper curves) are correlated at low pressure where nonlinear fluctuations dominate and uncorrelated at high pressure, where linear fluctuations dominate. The points labeled 'a' and 'b' indicate the pressures at which figures (a) and (b) were evaluated. (d) Energy vs. frequency for the oscillator in x-direction (x mode) obtained from both random fluctuations (colored density plot) and from parametric excitation (black). The thermal excitation of the orthogonal modes (y, z) shifts the resonance by $\approx 2.5\,\mathrm{kHz}$ in good agreement with the value estimated from the thermal amplitude and the measured nonlinear coefficients.*

onal modes (y and z) leads to an average shift the frequency of the mode under consideration (here x). The shift of the center of the frequency distribution ($\approx$ 2.5kHz) is in good agreement with the value estimated from the measured nonlinear coefficients and average thermal amplitudes (sup-

plementary information). Additionally, since the amplitudes of the modes fluctuate independently (c.f. Fig. 5.3c), we get a distribution of frequencies for a given oscillation amplitude of the considered mode. In contrast, when we drive the system parametrically at a fixed frequency, we simultaneously cool the orthogonal modes. Therefore, the contribution to the frequency shift originating from the orthogonal modes is negligible and we obtain a sharp response.

5.3.2 Pressure dependence of frequency fluctuations

In figure 5.4 we show the power spectral density of the relative frequency Ω/Ω_0 (fPSD) as a function of pressure. The fPSDs are calculated from 30 min long timetraces of the instantaneous frequencies (c.f. Fig.5.3). For low Q, the fPSD is flat as expected for a harmonic oscillator. In contrast for high Q the nonlinear coupling maps the Lorenzian power spectral density of the amplitude onto the frequency power spectral density, which is therefore given by

$$S_{\mathrm{f}}(\Omega) = I\frac{\Omega_c/\pi}{\Omega^2+\Omega_c^2}, \tag{5.8}$$

where I is the total spectral power, which is independent of pressure. The characteristic cut-off frequency Ω_c has a clear pressure dependence, as shown in Fig. 5.4c. This further confirms that the fluctuations arise as a combination of nonlinearities and thermal excitations.

The small mass and high Q-factor make the levitated nanoparticle an ultrasensitive force sensor with sensitivity of $S_F = 4k_BTm\Omega_0/Q \approx (20\mathrm{zN})^2/\mathrm{Hz}$ at room temperature, which compares to the best values achieved at cryogenic temperatures [Moser et al., 2013]. There are several ways to couple a force to a levitated nanoparticle, including electric [Li et al., 2011] and magnetic [Neukirch et al., 2013; Geiselmann et al., 2013] coupling or more subtle forces due to fluctuating charges within the particle [Zurita-Sánchez et al., 2004]. Additionally, in contrast to trapped ions [Knünz et al., 2010], the still considerable mass of the particle makes it susceptible to gravitational forces [Arvanitaki and Geraci, 2013].

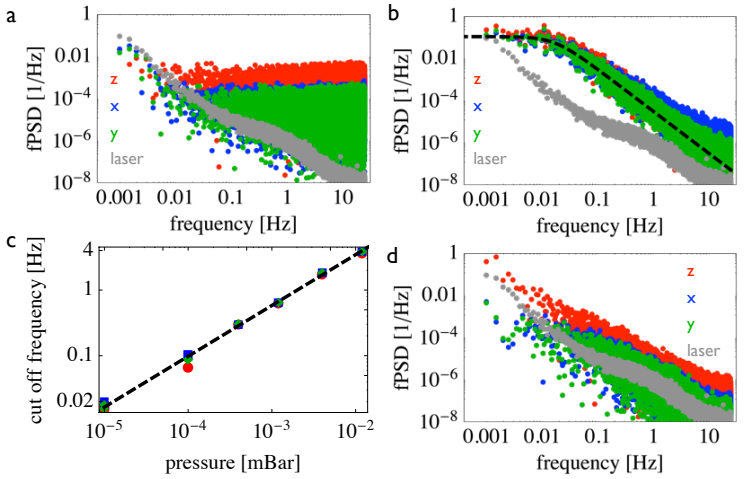

Figure 5.4: **Pressure dependence of frequency fluctuations.** *Pressure dependence of frequency fluctuations. (a) At high pressures (6mBar), the fluctuations are solely determined by the linear damping (low Q). (b) When the Q factor becomes larger (1e-5mBar), the fluctuations are dominated by nonlinear amplitude-frequency conversion. In this case, the frequency power spectral density (fPSD) exhibits a characteristic cut-off, which we extract from a fit to* (5.8) *(black dashed line). (c) The characteristic cut-off frequency depends on the Q factor which scales linearly with pressure. (d) Using feedback cooling, the fluctuations can be suppressed to the level of the laser intensity fluctuations (gray).*

In addition to constant forces, a levitated nanoparticle can detect position dependent forces. A position dependent force causes a frequency shift. Therefore, following the resonance frequencies of the nanoparticle allows for measuring a force gradient with a precision given by the noise floor of the frequency fluctuations. In practice though, as shown above nonlinear effects lead to frequency fluctuations in ultra-high Q oscillators. It is possible to surpass this limit by operating the oscillator at special points [Villanueva

et al., 2013]. Furthermore, as we show in the following, nonlinear frequency fluctuations can also be suppressed by feedback cooling [Gieseler et al., 2012]. Feedback cooling lowers the oscillation amplitude and therefore reduces the thermal motion of the oscillator. Under the action of feedback, the effective temperature reduces to $T_{\rm eff} = (\Gamma_0/\Gamma_{\rm fb})T$, where $\Gamma_{\rm fb}$ is the total damping with feedback [Mertz et al., 1993; Gieseler et al., 2012]. As shown in Fig.5.4d, we manage to reduce the frequency fluctuations to the level of the laser intensity fluctuations, which become the main source of frequency noise. Using active stabilization techniques, relative laser intensity noise can be brought to the level of $10^{-8}/\sqrt{\rm Hz}$ [Seifert et al., 2006].

5.3.3 Frequency stabilization by feedback cooling

We demonstrate the improved sensitivity by mimicking a periodic potential landscape. A modulation at 50mHz is applied to the trapping laser. The modulation causes a variation of the force gradient, which is measured as a frequency shift. As shown in Fig. 5.5, without feedback the signal is overwhelmed by noise while with feedback, the fluctuations are suppressed down to the level of laser intensity fluctuations and the applied signal is clearly visible. Using feedback cooling, we are able to improve the sensitivity of the oscillator by two orders of magnitude and achieve a relative frequency noise floor of $\sqrt{S_f}/\Omega_0$ of $3 \times 10^{-3}/\sqrt{\rm Hz}$ for frequencies below 1 Hz and $1 \times 10^{-4}/\sqrt{\rm Hz}$ for frequencies larger than 10Hz. In the absence of laser intensity noise the highest sensitivity is obtained when linear and nonlinear fluctuations contribute equally. However, since cooling to $T_{\rm eff} = T\,Q_{\rm eff}/Q$ is required to reduce nonlinear frequency fluctuations, the effective Q-factor is reduced, too. The best compromise is achieved when the linear and the

nonlinear frequency fluctuations contribute equally, that is

$$\begin{aligned}\Delta\Omega_{\mathrm{L}} =& \Delta\Omega_{\mathrm{NL}} \\ \Omega_0 Q_{\mathrm{eff}}^{-1} =& \frac{3}{8}\xi\Omega_0 r_{\mathrm{eff}}^2 = \frac{3\xi\Omega_0 k_B T_{\mathrm{eff}}}{4m\Omega_0^2} \\ \Rightarrow Q_{\mathrm{eff}}^{(\mathrm{opt})} =& \sqrt{\frac{4}{3}\frac{m\Omega_0^2}{\xi k_B T}Q} = \mathcal{R}^{-1/2}Q. \end{aligned} \tag{5.9}$$

Thus, under the assumption that with cooling the oscillation remains in the linear regime, the frequency spectral density is given by

$$S_f^{(\mathrm{opt})} = \frac{\Omega_0}{Q_{\mathrm{eff}}^{(\mathrm{opt})}} = \frac{\Omega_0}{Q}\mathcal{R}^{1/2}. \tag{5.10}$$

For the values presented here we obtain $\sqrt{S_f^{(\mathrm{opt})}}/\Omega_0 \sim 10^{-6}/\sqrt{\mathrm{Hz}}$, sufficient to sense ultraweak interactions, such as non-Newtonian gravity-like forces [Geraci et al., 2010]. However, to reach this value, relative intensity fluctuation have to be suppressed down to the same level.

The ultimate cooling limit is defined by the zero point motion $q_{\mathrm{zp}} = \sqrt{\hbar/2m\Omega_0}$. In order to resolve the nonlinear frequency shift due to the zero point motion $\Delta\Omega_{\mathrm{zp}}$, the condition

$$\frac{\Delta\Omega_{\mathrm{zp}}}{\Delta\Omega_{\mathrm{L}}} = \frac{3}{8}Q\xi q_{\mathrm{zp}}^2 \gg 1 \tag{5.11}$$

has to be satisfied in analogy to (5.5). This requires a Q factor of $Q = \Omega_0/\Delta\Omega_{\mathrm{zp}} \approx 10^{10}$. In absence of other noise sources, this regime is reached for pressures below 10^{-8}mBar.

5.4 Conclusion

In conclusion, we have demonstrated that a laser-trapped nanoscale particle in high vacuum defines an ultrasensitive force sensor. The thermal motion of the residual gas drives the nanoparticle into its nonlinear regime,

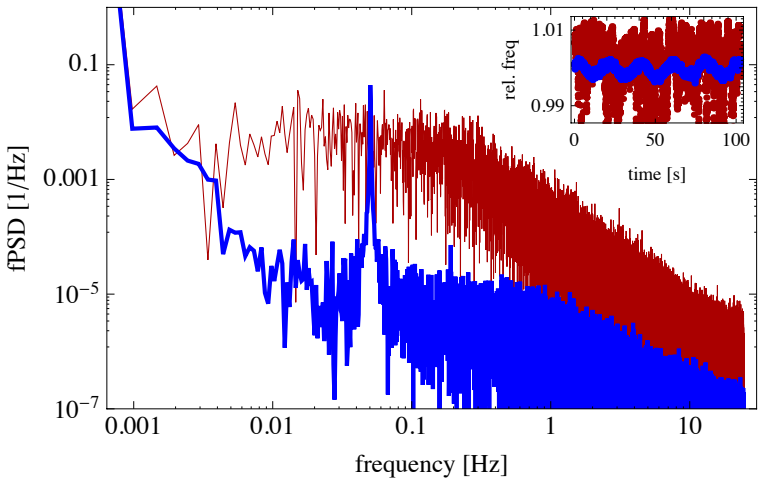

Figure 5.5: **Detection of a Periodic force gradient using feedback cooling.** *A periodic potential landscape is emulated by modulating the trapping frequency at* 50 mHz*. In absence of feedback cooling the small signal is overwhelmed by noise (red). Feedback cooling reduces the random frequency fluctuations thereby making it possible to detect the signal (blue). (inset) Time domain signal of relative frequency with (blue) and without feedback (red).*

which gives rise to frequency fluctuations. Using a parametric feedback cooling scheme, we can stabilize the nanoparticle and suppress its nonlinearities, without sacrificing sensitivity. We expect that feedback-controlled nanoparticles will find applications for sensing a wide range of interactions, including van der Waals and Casimir forces [Geraci et al., 2010], nuclear spins [Rugar et al., 2004], and gravitation [Arvanitaki and Geraci, 2013].

CHAPTER 6

Dynamic relaxation from an initial non-equilibrium steady state

Fluctuation theorems are a generalisation of thermodynamics on small scales and have been established as tools to measure thermodynamic quantities in non-equilibrium mesoscopic systems. Here, we study experimentally and theoretically non-equilibrium relaxation of a vacuum trapped nanoparticle from an initial steady state distribution to thermal equilibrium and show that the Crooks fluctuation theorem holds. The here established framework allows to study experimentally non-equilibrium fluctuation theorems for arbitrary steady states and can be extended to investigate experimentally quantum fluctuation theorems or systems which do not obey detailed balance.

6.1 Introduction

One of the tenets of statistical physics is the central limit theorem. It allows to reduce many microscopic degrees of freedom u_i ($i = 1 \dots N$, $N = \mathcal{O}(10^{23})$) to only a few macroscopic degrees of freedom U. The central limit theorem states that, independently of the distributions of the u_i,

a macroscopic extensive quantity U, such as the total energy of a system with N degrees of freedom follows a Gaussian distribution with a mean value $\langle U \rangle \propto N$ and variance $\sigma_U^2 \propto N$. Consequently, for $N \to \infty$, the relative fluctuations $\sigma_U / \langle U \rangle \to 0$ vanish and the macroscopic quantity becomes sharp. However, with the advance of nanotechnology it is now possible to study experimentally systems small enough that the relative fluctuations are comparable to the mean value. This gives rise to new physics where classical thermodynamic relations such as the second law of thermodynamics appear to be violated [Wang et al., 2002]. The statistical properties of the fluctuations are described by mathematical relations known as fluctuation theorems [Crooks, 1999; Jarzynski, 1997; Bochkov and Kuzovlev, 1981; Machlup and Onsager, 1953], which in the limit $N \to \infty$ recover the macroscopic thermodynamic relations.

Fluctuation relations are particularly important to understand fundamental chemical and biological processes, which occur on the mesoscale where the dynamics are dominated by thermal fluctuations [Bustamante et al., 2005]. They allow us, for instance, to relate the work along non-equilibrium trajectories to thermodynamic free-energy differences [Alemany et al., 2012; Collin et al., 2005]. Fluctuation theorems have been experimentally tested on a variety of systems including pendulums [Douarche et al., 2006], trapped microspheres [Wang et al., 2002], electric circuits [Garnier and Ciliberto, 2005], electron tunneling [Küng et al., 2012; Saira et al., 2012], two-level systems [Schuler et al., 2005] and single molecules [Hummer and Szabo, 2001; Liphardt et al., 2002]. Most experiments are described by an overdamped Langevin equation. However, systems in the underdamped regime, or in quantum systems where the concept of classical trajectory looses its usual meaning [Alemany et al., 2011], are less explored.

Here, we study experimentally the thermal relaxation of non-Gaussian steady states of a highly underdamped nanomechanical oscillator. Because of the low damping, the dynamics can be precisely controlled even at the quantum level [Teufel et al., 2011; Chan et al., 2011; O'Connell et al., 2010]. This high level of control allows to produce non-thermal steady states and makes them ideal candidates for investigating non-equilibrium fluctuations for transitions between arbitrary steady states. To prove the basic concept

of our approach, we investigate the relaxation of non-thermal initial states to thermal equilibrium. While for the initial steady state detailed balance can be violated, the relaxation dynamics are described by the Langevin equation which satisfies detailed balance and we can prove that the Crooks fluctuation theorem is fulfilled. Our experimental framework naturally extends to study transitions between arbitrary steady states and even to experimentally investigate quantum fluctuation theorems [Huber et al., 2008] for a nanomechanical oscillator prepared in a quantum state [Teufel et al., 2011; Chan et al., 2011; O'Connell et al., 2010].

6.2 Description of the experiment

The experimental configuration is shown in Fig. 6.1. We consider a silica nanoparticle of radius $a \sim 75\,nm$ and mass $m \sim 3\times10^{-18}\,kg$ that is trapped in vacuum by an optical tweezer (Fig. 6.1). Within the trap, the particle oscillates in all three spatial directions. To first approximation, the three motional degrees of freedom are well decoupled. Hence, the particle position q is described by the following one-dimensional equation of motion

$$\ddot{q} + \Gamma_0\dot{q} + \Omega_0^2 q = \left(\mathcal{F}_{\text{fluct}} + F_{\text{ext}}\right)/m, \tag{6.1}$$

where $\Omega_0/2\pi \sim 125\text{kHz}$ is the particle's angular frequency along the direction of interest, Γ_0 the friction coefficient and F_{ext} is an externally applied force. The random nature of the collisions does not only provide deterministic damping Γ_0 but also a stochastic force $\mathcal{F}_{\text{fluct}}$ that thermalises the energy of the particle. The fluctuation-dissipation theorem links the damping rate intimately to the strength of the stochastic force $\langle\mathcal{F}_{\text{fluct}}(t)\mathcal{F}_{\text{fluct}}(t')\rangle = 2m\Gamma_0 k_B T_0\delta(t-t')$, with T_0 being the bath temperature and k_B Boltzmann's constant.

The energy of the free harmonic oscillator with displacement q and momentum p is given by

$$E(q,p) = \frac{1}{2}\left(m\Omega_0^2 q^2 + p^2/m\right) = \frac{1}{2}m\Omega_0^2 q_0(t)^2, \tag{6.2}$$

where in the second part we use the slowly-varying amplitude approximation ($q(t) = q_0 \sin(\Omega_0 t)$, $\dot{q}_0 \ll \Omega_0 q_0$). This approximation is well satisfied in our experiments since it takes several oscillation periods for the particle amplitude to change (inset Fig. 6.2a).

Applying an external force F_{ext}, the system is initially prepared in a steady state with distribution $\rho_{\text{ss}}(u, \alpha)$, where $u = \{q, p\}$ describes the state of the system. At time $t = t_{\text{off}}$ the external force is switched off and we follow the evolution of the undisturbed system. Here, α denotes one or

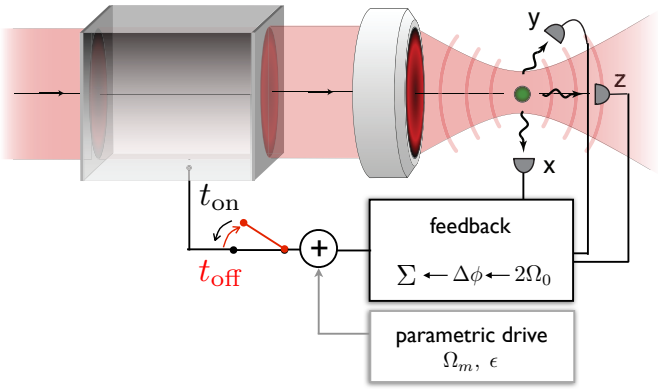

Figure 6.1: **Experimental setup.** *The particle is trapped by a tightly focused laser beam. In a first experiment, the particle is initially cooled by parametric feedback. At time $t = t_{\text{off}}$ the feedback is switched off and the particle trajectory is followed as it relaxes to equilibrium. After relaxation, the feedback is switched on again and the experiment is repeated. In a second experiment the particle is initially excited by an external modulation in addition to feedback cooling. Again at a time $t = t_{\text{off}}$, both the feedback and the external modulation are switched off and the particle is monitored as it relaxes.*

several parameters such as the strength of the feedback mechanism, which determines the initial steady state distribution. In general, $\rho_{\rm ss}(u, \alpha)$ is not known analytically.

6.2.1 Average energy relaxation

We derive from (6.1) the corresponding stochastic differential equation for the energy E of the unperturbed system[1] (c.f. Eq. 3.29):

$$\mathrm{d}E = -\Gamma_0 \left(E - k_{\rm B}T_0\right) \mathrm{d}t + \sqrt{E}\sqrt{\Gamma_0 k_{\rm B} T_0}\mathrm{d}W, \tag{6.3}$$

which has a deterministic and stochastic contribution. Carrying out an average over noise realisations and exploiting that $\langle \mathrm{d}W \rangle = 0$, the ensemble average of the energy evolves according to

$$\frac{\mathrm{d}\langle E \rangle}{\mathrm{d}t} = -\Gamma_0 \langle E \rangle + \Gamma_0 k_{\rm B} T_0. \tag{6.4}$$

This differential equation can be easily solved yielding an exponential relaxation of the average energy to its equilibrium value of $k_{\rm B}T_0$

$$\langle E(t) \rangle = k_{\rm B}T_0 + [\langle E(0) \rangle - k_{\rm B}T_0] e^{-\Gamma_0 t}, \tag{6.5}$$

where $\langle E(0) \rangle$ is the average energy at time 0.

According to Eq. 6.5, we expect the particle's energy to increase (decrease) as it relaxes to equilibrium if the particle's initial energy is below (above) the energy of the thermal bath. However, due to the smallness of the system, there is also a finite probability that molecule collisions further decrease (increases) the particle's energy. In the following section we show that the fluctuation theorem

$$\frac{P_t(Y)}{P_t(-Y)} = e^{-Y}. \tag{6.6}$$

[1] i.e. the feedback or any other modulation is off

holds for the a quantity Y, which accounts for the contribution of feedback to the particle energy. Eq. 6.6 links the probability of observing a process were Y increases to the probability of observing a process where Y decreases. Since Y is an extensive quantity, irreversibility for macroscopic systems is a direct consequence of the fluctuation theorem.

6.3 Fluctuation theorem

The fluctuation theorem for relaxation from an arbitrary initial distribution can be derived based on two conditions:

momentum (time) reversal symmetry for all times and

detailed balance for $t > 0$.

Since the energy is quadratic in the momentum p, the former condition is always fulfilled if the distribution is a function of the energy only. This is the case for parametric feedback cooling. The latter condition is fulfilled for a system evolving according to a Langevin equation.

6.3.1 General case

Consider the relaxation from an initial steady state distribution

$$\rho_{\mathrm{ss}}(u,\alpha) = \frac{1}{Z_\alpha} \exp\left\{-\beta_0 H_\alpha\right\}, \tag{6.7}$$

to the equilibrium distribution

$$\rho_{\mathrm{eq}}(u) = \frac{1}{Z} \exp\{-\beta_0 E\}, \tag{6.8}$$

where $\beta_0 = 1/k_{\mathrm{B}}T_0$ is the inverse temperature of the thermal bath and where $Z_\alpha = \int \mathrm{d}u \rho_{\mathrm{ss}}(u,\alpha)$ and $Z = 2\pi k_{\mathrm{B}}T_0/\Omega_0$ are the partition functions of the initial distribution and the final equilibrium distribution, respectively. The initial distribution is determined by the total energy

$$H_\alpha(u) = E(u) - M_\alpha(u), \tag{6.9}$$

which we can write as the sum of the particle energy and the (negative) feedback energy $M_\alpha(u)$. To proof (6.6), we introduce

$$Y(u,v) = M(v) - M(u) = \Delta E - \beta_0^{-1}\Delta\phi, \tag{6.10}$$

which measures the difference in feedback energy between states u and v. For a simplified notation we have introduced $\Delta E = E(v) - E(u)$ and $\Delta\phi = \phi_\alpha(v) - \phi_\alpha(u) = \beta_0 \Delta H_\alpha$.

The distribution of Y at time t is obtained by averaging over all initial conditions u_0 and all possible trajectory endpoints u_t after time t

$$P_t(Y) = \int du_0 \int du_t \rho_{\rm ss}(u_0) p_t(u_0 \to u_t) \delta\left[M(u_t) - M(u_0) - Y\right] \tag{6.11}$$

$$= \int du \int dv \rho_{\rm ss}(u) p_t(u \to v) \delta\left[M(v) - M(u) - Y\right], \tag{6.12}$$

where $\delta(u)$ is the Dirac function and we changed variables $\{u_0, u_t\} \to \{u, v\}$ to save some writing. $P_t(Y)dY$ is the probability to observe Y in the interval $[Y, Y + dY]$. Accordingly, the probability to observe $-Y$ is

$$P_t(-Y) = \int du \int dv \rho_{\rm ss}(u) p_t(u \to v) \delta\left[M(v) - M(u) + Y\right]. \tag{6.13}$$

Renaming integration variables yields

$$P_t(-Y) = \int dv \int du \rho_{\rm ss}(v) p_t(v \to u) \delta\left[M(u) - M(v) + Y\right] \tag{6.14}$$

$$= \int dv \int du \rho_{\rm ss}(v) p_t(v \to u) \delta\left[M(v) - M(u) - Y\right]$$

$$= \int du \int dv \rho_{\rm ss}(u) \frac{\rho_{\rm ss}(v)}{\rho_{\rm ss}(u)} p_t(v \to u) \delta\left[M(v) - M(u) - Y\right].$$

Additionally, by combining (6.7), (6.8) and (6.10), it is easy to show that

$$\frac{\rho_{\rm ss}(v)}{\rho_{\rm ss}(u)} = \frac{\rho_{\rm eq.}(v)}{\rho_{\rm eq}(u)} e^{Y(u,v)}. \tag{6.15}$$

Now, we know that a system evolving according to the Langevin equation at temperature T_0 obeys the detailed balance condition with respect to the equilibrium distribution $\rho_{\text{eq.}}(u)$. In particular this holds for the unperturbed system (feedback off) [1]

$$\rho_{\text{eq.}}(u)p_t(u \to v) = \rho_{\text{eq.}}(\bar{v})p_t(\bar{v} \to \bar{u}). \tag{6.16}$$

Here, $\bar{u}$ denotes the phase space point $\bar{u} = \{q, -p\}$ obtained from $u = \{q, p\}$ by inversion of the momenta and $p_t(u \to v)$ is the probability (density) to find the system at v at time t provided it was at u at time 0. Now, detailed balance (6.16) implies

$$\frac{\rho_{\text{eq.}}(v)}{\rho_{\text{eq.}}(u)}p_t(v \to u) = p_t(\bar{u} \to \bar{v}), \tag{6.17}$$

where we used that $\rho_{\text{eq.}}(u) = \rho_{\text{eq.}}(\bar{u})$ since the energy $E(u)$, and hence also distribution (6.8) is symmetric with respect to momentum reversal. This symmetry also applies to the feedback energy $M(u) = M(\bar{u})$ and, therefore, also applies to the initial steady state distribution (6.7), that is

[1] Since we can derive a Langevin equation for the energy E (more precisely $\epsilon = \sqrt{E}$), this holds also true for the system evolving under feedback

$\rho_{\rm ss}(u,\alpha) = \rho_{\rm ss}(\bar{u},\alpha)$ (c.f. chapter 3). Therefore, (6.14) can be written as

$$P_t(-Y) = \int du \int dv \rho_{\rm ss}(u) e^{Y(u,v)} \frac{\rho_{\rm eq.}(v)}{\rho_{\rm eq}(u)} p_t(v \to u) \delta\left[M(v) - M(u) - Y\right] \tag{6.18}$$

$$\begin{aligned}
&= \int du \int dv \rho_{\rm ss}(u) e^{Y(u,v)} p_t(\bar{u} \to \bar{v}) \delta\left[M(v) - M(u) - Y\right] \\
&= \int d\bar{u} \int d\bar{v} \rho_{\rm ss}(\bar{u}) e^{Y(\bar{u},\bar{v})} p_t(\bar{u} \to \bar{v}) \delta\left[M(\bar{v}) - M(\bar{u}) - Y\right] \\
&= \int du \int dv e^{Y(u,v)} \rho_{\rm ss}(u) p_t(u \to v) \delta\left[M(\bar{v}) - M(\bar{u}) - Y\right] \\
&= e^{Y} \underbrace{\int du \int dv \rho_{\rm ss}(u) p_t(u \to v) \delta\left[M(\bar{v}) - M(\bar{u}) - Y\right]}_{P_t(Y)},
\end{aligned}$$

where in the third line we changed variables to $\bar{u}$ and $\bar{v}$, using $\left|\frac{\partial(\bar{u},\bar{u})}{\partial(u,v)}\right| = 1$ and used the fact that $M(u)$ is symmetric with respect to momentum reversal, that is $M(u) = M(\bar{u})$. In the fourth line we renamed the integration variables and in the final step we have used that the Dirac delta vanishes for all $Y(u,v) \neq Y$[1]. Note that $Y(u,v)$ is a function of the states u and v, while Y is the value for which we evaluate the probability $P_t(Y)$.

Finally, we arrive at the Crooks fluctuation relation for Y:

$$\Rightarrow \frac{P_t(Y)}{P_t(-Y)} = e^{-Y}. \tag{6.19}$$

The relation is valid for any time $t > 0$. Note that the time t is arbitrary and it is not required that within this time the system actually reaches the

[1] $Y(u,v) = M(v) - M(u) = M(\bar{v}) - M(\bar{u})$, thus all contributions $Y(u,v) \neq Y$ to the integral vanish and we can substitute $Y(u,v) \to Y$. Since Y doesn't depend on the states u, v, we can pull it out of the integral.

equilibrium distribution, thus $P_t = P$. From this relation we can easily obtain

$$\langle e^Y \rangle = \int \mathrm{d}Y P(Y) e^Y = \int \mathrm{d}Y P(-Y) = 1, \tag{6.20}$$

where the last step involves a variable change from Y to $-Y$.

6.3.2 Relaxation from an initial equilibrium state

If the initial steady state $\rho_{\mathrm{ss}}(u, \alpha)$ is an equilibrium distribution $e^{-\beta E(u)}/Z(\beta)$ corresponding to the temperature $T = 1/k_B\beta$, the expressions become particularly simple. In this case, $\Delta\phi = \beta\Delta E$ and

$$Y = (\beta_0 - \beta)(E_t - E_0). \tag{6.21}$$

6.3.3 Relaxation from a steady state generated by parametric feedback

If the initial steady state $\rho_{\mathrm{ss}}(u, \alpha)$ is due to parametric feedback cooling, the total energy is given by (c.f. chapter 3)

$$H_\alpha = E + \frac{\alpha}{4}E^2. \tag{6.22}$$

In this case, $\Delta\phi = \beta_0\Delta H$ and

$$Y = -\beta_0\frac{\alpha}{4}\left(E_t^2 - E_0^2\right). \tag{6.23}$$

Theoretical position distribution

Based on the energy distribution $\rho_{\mathrm{fb}}(E, \alpha)$ of Eqs. 6.7 and 6.22 we can derive the phase space distribution $\rho_{\mathrm{fb}}(q, p, v)$ of the non-equilibrium steady state generated by application of the feedback. We start by writing the joint probability distribution function $\rho_{\mathrm{fb}}(q, E, \alpha)$ to observe the pair (q, E) as

$$\rho_{\mathrm{fb}}(q, E, \alpha) = \rho(q|E, \alpha)\rho_{\mathrm{fb}}(E, \alpha), \tag{6.24}$$

where $\rho(q|E,\alpha)$ is the conditional probability to observe the position q for a given energy E at feedback strength α. Assuming that the motion of the oscillator is essentially undisturbed during an oscillation period (this is the assumption that we have made all along), the distribution of positions is given by

$$\rho(q|E,\alpha) = \begin{cases} \frac{\Omega_0}{\pi\sqrt{2E/m-\Omega_0^2 q^2}} & \text{if } q^2 \leq \frac{2E}{m\Omega_0^2} \\ 0 & \text{else} \end{cases} \tag{6.25}$$

simply because the probability to find the system at q is inversely proportional to the magnitude of the velocity, $|v| = |p|/m = \sqrt{2E/m - \Omega_0^2 q^2}$ the system has at q. This conditional probability distribution diverges at the turning points $\pm q_0 = \pm\sqrt{2E/m\Omega_0^2}$ and it vanishes for $|q| > q_0$. Multiplying the conditional distribution $\rho(q|E,\alpha)$ with the energy distribution from Eq. (6.7) one obtains the desired joint distribution $\rho_{\rm fb}(q,E,\alpha)$. Next, we change variables from (q,E) to (q,p). The respective distributions are related by

$$\rho_{\rm fb}(q,p,\alpha) = \frac{1}{2}\rho_{\rm fb}(q,E,\alpha)\left|\frac{\partial(q,E)}{\partial(q,p)}\right| \tag{6.26}$$

The Jacobian of the transformation is given by

$$\left|\frac{\partial(q,E)}{\partial(q,p)}\right| = \begin{vmatrix} \frac{\partial q}{\partial q} & \frac{\partial q}{\partial p} \\ \frac{\partial E}{\partial q} & \frac{\partial E}{\partial p} \end{vmatrix} = \frac{|p|}{m}. \tag{6.27}$$

In Eq. 6.26 we have exploited that the distribution $\rho_{\rm fb}(q,p,\alpha)$ is symmetric in p, and the factor $1/2$ arises because p and $-p$ correspond to the same energy $E = m\Omega_0^2 q^2/2 + p^2/2m$. Thus, the phase space density $\rho_{\rm fb}(q,p,\alpha)$ becomes

$$\begin{aligned} \rho_{\rm fb}(q,p,\alpha) &= \frac{1}{2}\rho_{\rm fb}[E(q,p),\alpha]\frac{\Omega_0}{\pi\sqrt{2E/m-\Omega_0^2 q^2}}\frac{|p|}{m} \\ &= \frac{\Omega_0}{2\pi}\rho_{\rm fb}[E(q,p),\alpha], \end{aligned} \tag{6.28}$$

where we have used that $|p|/m = \sqrt{2E/m - \Omega_0^2 q^2}$. Note that the second case of Eq. (6.25) does not need to be taken into account, because for given

q and p, the condition $q^2 \leq 2E/m\Omega_0^2$ is always obeyed. Using the energy distribution from Eqs. 6.7 and 6.22 we finally obtain

$$\rho_{\mathrm{fb}}(q,p,\alpha) = \frac{\Omega_0}{2\pi Z_\alpha} \exp\left\{-\beta_0 E(q,p) - \beta_0 \alpha E(q,p)^2\right\}. \tag{6.29}$$

From the phase space density $\rho_{\mathrm{fb}}(q,p,\alpha)$ one can get the distribution $\rho_{\mathrm{fb}}(q,\alpha)$ of the positions by integration over the momenta:

$$\rho_{\mathrm{fb}}(q,\alpha) = \int_{-\infty}^{\infty} \mathrm{d}p\, \rho_{\mathrm{fb}}(q,p,\alpha). \tag{6.30}$$

Carrying out the integral yields the position distribution

$$\rho_{\mathrm{fb}}(q,\alpha) = \sqrt{\frac{\beta_0 m\Omega_0^2(4+\alpha m\Omega_0^2 q^2)}{8\pi^3}} \frac{\exp\left[-\frac{\beta_0(4+\alpha m\Omega_0^2 q^2)^2}{32\alpha}\right]}{\mathrm{erfc}\left(\sqrt{\beta_0/\alpha}\right)} \times \mathrm{K}_{1/4}\left[\frac{\beta_0(4+\alpha m\Omega_0^2 q^2)^2}{32\alpha}\right], \tag{6.31}$$

where erfc and $\mathrm{K}_{1/4}$ are the complementary error function and a generalized Bessel function of the second kind, respectively.

6.4 Experimental results

In the following we experimentally investigate the fluctuation theorem (6.19) for two different initial steady state distributions, parametric feedback cooling (ss = fb) and external modulation (ss = mod), respectively.

6.4.1 Relaxation from feedback cooling

First, we enforce a non-equilibrium state on the particle by applying a force $F_{\mathrm{ext}} = F_{\mathrm{fb}}$ to the oscillating particle through a parametric feedback scheme

[Gieseler et al., 2012]. The feedback $F_{\rm fb} = -\eta\Omega_0 q^2 \dot{q}$ adds a cold damping $\Gamma_{\rm fb}$ to the natural damping Γ_0. This is different to thermal damping, where an increased damping is accompanied by an increase in fluctuations. Since parametric feedback adds an amplitude dependent damping $\Gamma_{\rm fb}(u) \propto q^2$, oscillations with a large amplitude experience a stronger damping than oscillations with a small amplitude.

Position distribution

At time $t = t_{\rm off}$ the feedback is switched off. Once the feedback is switched off, the collisions with the surrounding molecules are no longer compensated by the feedback and the particle energy increases and the system relaxes back to the thermal equilibrium distribution (Fig. 6.2c,d).

The relaxation experiment is carried out 10^4 times, i.e., we repeatedly prepare initial conditions u_0 distributed according to $\rho_{\rm fb}(u_0, \alpha)$ watch the system as it evolves from u_0 to u_t in time t. Along each $\sim 1s$ trajectory we sample the position at a rate of 625kHz and from integration over 64 successive position measurements we obtain the energy at a rate of 9.8kHz. In figure 6.2a we show the average over the individual time-traces together with a fit to (6.5). Equilibrium is reached after a time of the order of $\tau_0 = 1/\Gamma_0 = 0.17$s. According to Eq. 6.5 and the measurement shown in Fig. 6.2, the average energy of the particle increases monotonically. However, due to the small size of the particle, the fluctuating part of (6.3) is comparable to the deterministic part and hence an individual trajectory can be quite different from the ensemble average in (6.5). Fig. 6.2b shows four realizations of the relaxation experiment. Each particle trajectory $q(t)$ results from switching off the feedback at a time $t = t_{\rm off}$.

Fluctuation theorem

The 10^4 trajectories allow us to evaluate the distributions $P_{\rm fb}(Y) = \langle \delta[Y - Y(u_t)] \rangle$ for different times t, where Y is calculated from Eq. 6.23 with the energies E_0, E_t measured at time 0 and t, respectively. Fig. 6.3a shows the

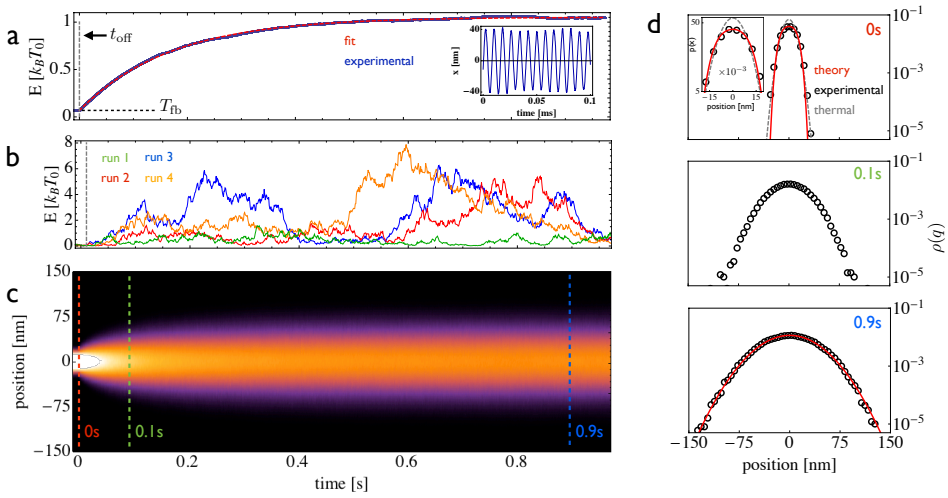

Figure 6.2: **Time evolution of relaxation of feedback cooled particle.** *(a) The particle is initially prepared with low energy $k_BT_{\rm eff}$ by parametric feedback cooling. At time $t_{\rm off}$ the feedback is switched off and the particle energy relaxes to the equilibrium energy k_BT_0. The average energy increases exponentially (The red dashed line is a fit to Eq. 6.5). (b) Each realization of the relaxation experiment renders a different trajectory and the time it takes the particle to acquire an energy equal to the thermal energy k_BT_0 deviates considerably from the average exponential increase of subfigure a. (c) Time evolution of the position distribution resulting from switching and (d) Cross cuts at* 0, 0.1s *and* 0.9s, *respectively. The red lines are the theoretical position distributions. The initial distribution shows a small deviation from a thermal equilibrium distribution (gray dashed line). Inset subfigure a: Over short times the particle oscillates with constant amplitude.*

measured steady state distribution in excellent agreement with (6.7) and (6.22). For comparison, the equivalent thermal distribution is shown (gray dashed line). As shown in Fig. 6.3a, the distributions $P_{\rm fb}(Y)$ are symmetric

for short times, whereas they become increasingly asymmetric for longer times, with higher probabilities for positive Y and lower probabilities for negative Y. To apply the fluctuation theorem (6.19) to our measurements we define

$$\Sigma(Y) = \ln\left[\frac{P(Y)}{P(-Y)}\right] = -Y, \tag{6.32}$$

where $\Sigma(Y)$ is predicted to be time-independent. Using the distributions for Y shown in Fig. 6.3b we compute $\Sigma(Y)$. The resulting data is shown in Fig. 6.3c. Since (6.19) is time-independent, we take the time-averaged distributions to improve the statistics. Fig. 6.3d shows $\Sigma(\langle P(Y)\rangle_t)$ in excellent agreement with the fluctuation theorem!

6.4.2 Relaxation from excited state

With our experimental apparatus we can study non-equilibrium relaxation for arbitrary initial states and transition between them. We demonstrate our capabilities by producing an extremely non-Gaussian initial distribution. In a second experiment, the system is driven by applying a parametric modulation in addition to parametric feedback cooling $F_{\text{ext}} = F_{\text{fb}} + F_{\text{mod}}$, where $F_{\text{mod}} = \epsilon\Omega_0^2 \cos(\Omega_{\text{mod}} t) q$ with modulation frequency $\Omega_{\text{mod}} = 249\text{kHz}$ and modulation depth $\epsilon = 0.03$.

Modulation at $\Omega_{\text{mod}}/2\pi$ brings the particle into oscillation at 124.5kHz and amplitude q_0. The resulting initial steady state position distribution features a characteristic double-lobe distribution

$$\rho_{\text{harm}}(q) = \frac{\pi^{-1}}{\sqrt{q_0^2 - q^2}} \tag{6.33}$$

of an harmonic oscillation. As in the previous experiment, at $t = t_{\text{off}}$ the modulation and the parametric feedback are switched off simultaneously, and we measure the dynamics during relaxation. Fig. 6.4 shows the relaxation of the particle's average energy and position distribution. The average initial energy is larger than the thermal energy $k_B T_0$ and relaxes

exponentially to the equilibrium value according to (6.5). As in the previous experiment, individual realizations of the switching experiment differ significantly from the average (Fig. 6.4b). As the system relaxes, the two lobes of the initial position distribution broaden until they merge into a single Gaussian peak.

Since the form of the initial distribution $\rho_{\mathrm{mod}}(E)$ is not know analytically

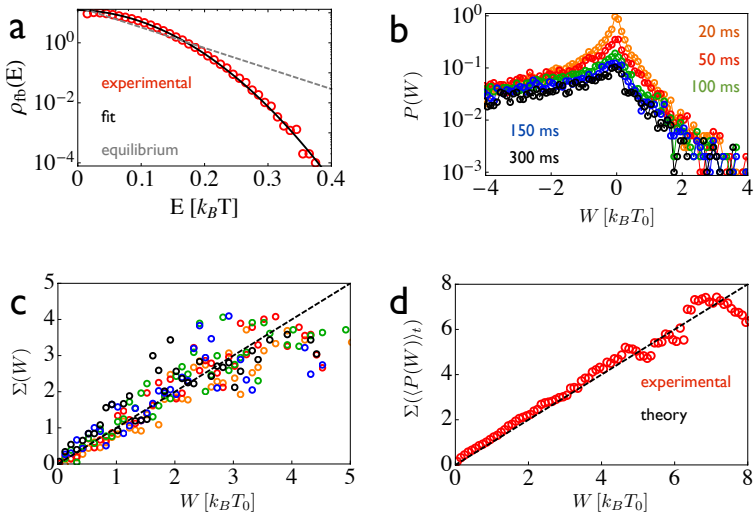

Figure 6.3: **Fluctuation theorem** *for the nanoparticle in Fig. 6.2. (a) Energy distribution with feedback on (red circles) and fit to Eq. 6.7 (black solid line). Large amplitude oscillations experience stronger damping and are therefore suppressed with respect to an equilibrium distribution with identical average energy (gray dashed line). (b) Probability density $P(Y)$ evaluated at different times after switching off the feedback. (c) The function $\Sigma(Y)$ evaluated for the distributions shown in (c) and (d) evaluated for the time averaged distributions $\langle P(Y)\rangle_t$ is in excellent agreement with the theoretical prediction (black dashed line).*

(as it is the case for parametric feedback), we determine it experimentally. With the measured initial distribution, we calculate Y according to Eq. 6.10

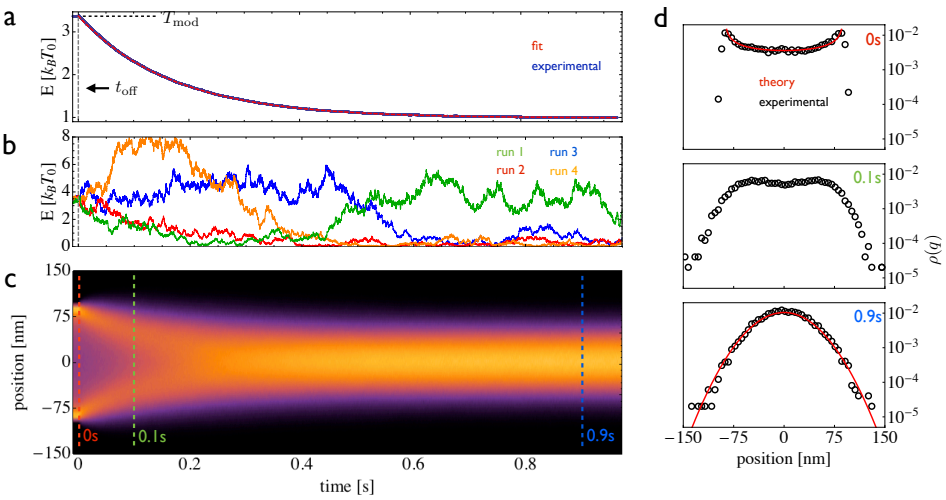

Figure 6.4: **Time evolution of relaxation of excited particle.** *(a) The particle is initially prepared with high energy k_BT_{eff} by applying a parametric modulation in addition to parametric feedback. At time t_{off} the feedback is switched off and the particle energy relaxes to the equilibrium energy k_BT_0. The average energy decreases exponentially (The red dashed line is a fit to Eq. 6.5). (b) Each realization of the relaxation experiment renders a different trajectory and the time it takes the particle to acquire an energy equal to the thermal energy k_BT_0 deviates considerably from the average exponential decrease of subfigure a. (c) Time evolution of the position distribution resulting from switching and (d) cross cuts at* 0, 0.1s *and* 0.9s, *respectively. The red lines are the theoretical position distributions, respectively. The initial distribution features a sharply peaked double lobe distribution, characteristic for a harmonic oscillation. As the system evolves, the two peaks smear out and approach each other until they form a single Gaussian.*

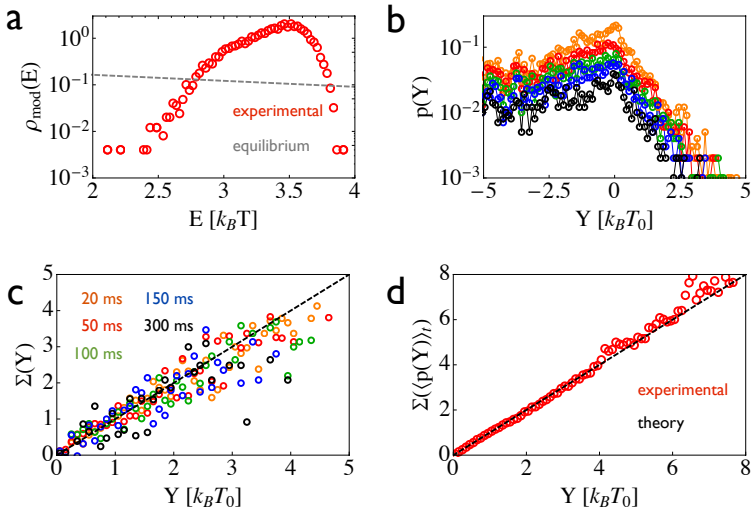

Figure 6.5: **Fluctuation theorem** *for the nanoparticle in Fig. 6.4. (a) The energy distribution with feedback and modulation on (red circles) differs significantly from an equilibrium distribution with identical average energy (gray dashed line). (b) Probability density $P(Y)$ evaluated at different times after switching off the feedback. (c) The function $\Sigma(Y)$ evaluated for the distributions shown in (c) and (d) evaluated for the time averaged distributions $\langle P(Y)\rangle_t$ is in excellent agreement with the theoretical prediction (black dashed line).*

from the energies E_0, E_t measured at times 0 and t, respectively. Fig. 6.5a shows the initial energy distribution $\rho_{\mathrm{mod}}(E)$. It features a narrow spread around a non-zero value and therefore differs significantly from a thermal distribution with identical effective temperature (gray dashed line). As before, we calculate $\Sigma(Y)$ and $\Sigma(\langle p(Y)\rangle_t)$ from the distributions $P(Y)$ and find excellent agreement with the theoretical prediction (Fig. 6.5).

6.5 Conclusion

In conclusion, we have measured energy fluctuations of a highly underdamped nanomechanical oscillator during relaxation from non-equilibrium steady states. Thanks to the low damping, the time scales of the random force and the intrinsic timescale of the oscillator separate. This allows us to control the motional degrees of freedom of the oscillator and to prepare it in an arbitrary initial state and study it's dynamics during relaxation to equilibrium. We show both theoretically and experimentally that the fluctuation theorem is fulfilled for relaxation from a steady state to thermal equilibrium. The here presented experimental framework naturally extends to study the transitions between arbitrary steady states and quantum fluctuation theorems similar to a recent proposal for trapped ions [Huber et al., 2008]. Further, we envision that our exponential approach of using an highly controllable nano-mechanical oscillator for studying fluctuation theorems will open up experimental and theoretical investigation of fluctuation theorems in more complex settings which arise for instance from the interplay of thermal fluctuations and nonlinearities [Gieseler et al., 2013] and in which detailed balance might be violated [Dykman and Krivoglaz, 1979; Dykman, 2012].

Appendix

A Calibration

In this section we relate the measured power spectral density to the physical one. This allows us to extract the calibration factor $c_{\text{calib.}}$, the radius of the particle a, the effective temperature T_{eff} and the natural damping rate Γ_0.

A.1 Calibration factor

We write the power spectral density in the form

$$S(\Omega) = \frac{a_1}{(a_3^2 - \Omega^2)^2 + a_2^2\Omega^2}, \tag{34}$$

where

$$a_1 = (c_{\text{calib}})^2 \frac{k_{\text{B}} T_0}{\pi m} \Gamma_0, \tag{35}$$

$$a_2 = \Gamma_0 + \delta\Gamma \text{ and} \tag{36}$$

$$a_3 = \Omega_0 + \delta\Omega \tag{37}$$

are the fit parameters and $c_{\text{calib.}}$ is a calibration factor with units V/m.

When the feedback is switched off $\delta\Gamma$ and $\delta\Omega$ are zero. Therefore, $a_2 = \Gamma_0$ and we find the particle radius a from the measured pressure P_{gas} and

$$a = 0.619 \frac{9\pi}{\sqrt{2}} \frac{\eta d_{\text{m}}^2}{\rho_{\text{SiO}_2} k_{\text{B}} T_0} \frac{P_{\text{gas}}}{\Gamma_0}, \tag{38}$$

where we have expanded (3.42) for small $\text{Kn}^{-1} = \text{a}/\bar{\text{l}}$. This is a valid approximation for the particle size and pressures considered here. For a gas at pressure P_{gas} and temperature T_0, the free mean path is given by $\bar{l} = (k_{\text{B}} T_0)/(\sqrt{2} d_{\text{m}}^2 \pi P_{\text{gas}})$, where $d_{\text{m}} = 0.372\,\text{nm}$ is the diameter of the gas molecules [O'Hanlon, 2003]. Here, $\eta = 18.27 \times 10^{-6}\,\text{Pa s}$ the viscosity of air and $\rho_{\text{SiO}_2} = 2200\,\text{kg/m}^3$ the density of Silica.

The calibration factor is then

$$c_{\text{calib}} = \sqrt{\frac{a_1}{a_2}\frac{\pi m}{k_{\text{B}}T_0}}, \tag{39}$$

where $m = 4\pi\,\rho_{\text{SiO}_2} a^3\,/3$ is the mass of the particle.

A.2 Effective temperature

From a calibration measurement without feedback and a measurement with feedback on we calculate the effective temperature as

$$T_{\text{eff}} = T_0 \frac{R^{(\text{FB})}}{R^{(\text{calib.})}}, \tag{40}$$

where $R = a_1/a_2$. The superscripts denote measurements with feedback on (FB) and feedback off (calib.), respectively.

A.3 Natural damping rate

In the case when the feedback is off the natural damping rate is simply given by $a_2 = \Gamma_0$. However, despite the fact that the feedback broadens the resonance, we can still determine Γ_0 from the shape of the power spectral density. Because the coefficient a_1 also depends on Γ_0 we find that

$$\Gamma_0 = \frac{a_1^{(\text{FB})}}{R^{(\text{calib.})}}, \tag{41}$$

where $R^{(\text{calib.})}$ is determined from a calibration measurement without feedback.

Bibliography

J.S. Aldridge and A.N. Cleland *Noise-enabled precision measurements of a Duffing nanomechanical resonator* Physical Review Letters **94**, 156403 (2005)

A. Alemany, M. Ribezzi, and F. Ritort *Recent progress in fluctuation theorems and free energy recovery* arXiv:1101.3174 (2011)

A. Alemany, A. Mossa, I. Junier, and F. Ritort *Experimental free-energy measurements of kinetic molecular state using fluctuation theorems* Nature Physics **8**, 688694 (2012)

R. Almog, S. Zaitsev, O. Shtempluck, and E. Buks *Signal amplification in a nanomechanical Duffing resonator via stochastic resonance* Applied Physics Letters **90**, 013508 (2007)

A.A. Ambardekar and Y. Li *Optical levitation and manipulation of stuck particles with pulsed optical tweezers* Optics Letters **30**, 1797-1799 (2005)

O. Arcizet, P.F. Cohadon, T. Briant, M. Pinard, and A. Heidmann. *Radiation-pressure cooling and optomechanical instability of a micromirror* Nature **444**, 71-74 (2006)

Y. Arita, A.W. McKinley, M. Mazilu, H. Rubinsztein-Dunlop, and K. Dholakia *Picoliter Rheology of Gaseous Media Using a Rotating Optically Trapped Birefringent Microparticle* Analytical Chemistry **83**, 8855-8858 (2011)

Y. Arita, M. Mazilu, and K. Dholakia *Laser-induced rotation and cooling of a trapped microgyroscope in vacuum* Nature Communications **4**, 2374 (2013)

J.L. Arlett, E.B. Myers, and M.L. Roukes *Comparative advantages of mechanical biosensors* Nature Nanotechnology **6**, 203-215 (2011)

A. Arvanitaki and A.A. Geraci *Detecting High-Frequency Gravitational Waves with Optically Levitated Sensors* Physical Review Letters **110**, 071105 (2013)

P. Asenbaum, S. Kuhn, S. Nimmrichter, U. Sezer, and M. Arndt. *Cavity cooling of free silicon nanoparticles in high-vacuum* Nature Communications **4**, 2743 (2013)

A. Ashkin *Acceleration and trapping of particles by radiation pressure.* Physical Review Letters **24**, 156-159 (1970)

A. Ashkin. *Optical Levitation by Radiation Pressure.* Applied Physics Letters **19**, 283-285 (1971)

A. Ashkin. *Forces of a single-beam gradient laser trap on a dielectric sphere in the ray optics regime* Biophysical Journal **61**, 569-582 (1992)

A. Ashkin and J.M. Dziedzic *Optical levitation in high vacuum* Applied Physics Letters **28**, 333-335 (1976)

A. Ashkin and J.M. Dziedzic *Feedback stabilization of optically levitated particles.* Applied Physics Letters **30**, 202-204 (1977)

A. Ashkin, J.M. Dziedzic, J.E. Bjorkholm, and S. Chu *Observation of a single-beam gradient force optical trap for dielectric particles* Optics Letters **11**, 288-290 (1986)

T. Bagci, A. Simonsen, S. Schmid, L.G. Villanueva, E. Zeuthen, J. Appel, J.M. Taylor, A. Sørensen, K. Usami, A. Schliesser, and E.S. Polzik *Optical detection of radio waves through a nanomechanical transducer* arXiv:1307.3467 (2013)

S.A. Beresnev, V.G. Chernyak, and G.A. Fomyagin. *Motion of a spherical particle in a rarefied gas. Part 2. Drag and thermal polarization.* Journal of Fluid Mechanics **219**, 405-421 (1990)

G.N. Bochkov and Y.E. Kuzovlev *Nonlinear fluctuation-dissipation relations and stochastic models in nonequilibrium thermodynamics* Physica A: Statistical Mechanics and its Applications **106**, 443-479 (1981)

V.B. Braginsky *Measurement of Weak Forces in Physics Experiments* University of Chicago Press (1977)

E. Buks and B. Yurke *Mass detection with a nonlinear nanomechanical resonator.* Physical Review E **74**, 046619 (2006)

C. Bustamante, J. Liphardt, and F. Ritort *The Nonequilibrium Thermodynamics of Small Systems.* Physics Today **58**, 43-48 (2005)

M. Campisi, P. Hanggi, and P. Talkner *Colloquium: Quantum fluctuation relations: Foundations and applications* Reviews of Modern Physics **83**, 771-791 (2011)

J. Chan, T.P. Mayer Alegre, A.H. Safavi-Naeini, J.T. Hill, A. Krause, S. Gröblacher, M. Aspelmeyer, and O. Painter *Laser cooling of a nanomechanical oscillator into its quantum ground state* Nature **478**, 89-92 (2011)

D.E. Chang, C.A. Regal, S.B. Papp, D.J. Wilson, J. Ye, O. Painter, H.J. Kimble, and P. Zoller *Cavity opto-mechanics using an optically levitated nanosphere* Proceedings of the National Academy of Sciences **107**, 1005-1010 (2010)

D.E. Chang, K.K. Ni, O. Painter, and H.J. Kimble *Ultrahigh-Q mechanical oscillators through optical trapping* New Journal of Physics **14**, 045002 (2012)

J. Chaste, A. Eichler, J. Moser, G. Ceballos, R. Rurali, and A. Bachtold *A nanomechanical mass sensor with yoctogram resolution* Nature Nanotechnology **7**, 301-304 (2012)

A.N. Cleland and M.L. Roukes *A nanometre-scale mechanical electrometer* Nature **392**, 160-162 (1998)

A.N. Cleland and M.L. Roukes *Noise processes in nanomechanical resonators* Journal of Applied Physics **92**, 2758-2769 (2002)

P.F. Cohadon, A. Heidmann, and M. Pinard *Cooling of a Mirror by Radiation Pressure* Physical Review Letters **83**, 3174 (1999)

D. Collin, F. Ritort, C. Jarzynski, S.B. Smith, I. Tinoco, and C. Bustamante *Verification of the Crooks fluctuation theorem and recovery of RNA folding free energies* Nature **437**, 231-234 (2005)

G.E. Crooks *The Entropy Production Fluctuation Theorem and the Nonequilibrium Work Relation for Free Energy Differences* Physical Review E **60**, 2721-2726 (1999)

F. Douarche, S. Joubaud, N.B. Garnier, A. Petrosyan, and S. Ciliberto *Work Fluctuation Theorems for Harmonic Oscillators* Physical Review Letters **97**, 140603 (2006)

M.I. Dykman *Fluctuating Nonlinear Oscillators. From nanomechanics to quantum superconducting circuits* Oxford University Press (2012)

M.I. Dykman and M.A. Krivoglaz *Theory of fluctuational transitions between the stable states of a non-linear oscillator* Soviet Physics - JETP **77**, 60-73 (1979)

M.I. Dykman and M.A. Krivoglaz *Theory of nonlinear oscillator interacting with a medium* Physics Reviews **5**, 265-441 (1984)

M.I. Dykman, R.R. Mannella, P.V.E. McClintock, S.M. Soskin, and N.G. Stocks *Noise-induced narrowing of peaks in the power spectra of underdamped nonlinear oscillators* Physical Review A **42**, 7041-7049 (1990)

M. Eichenfield, R. Camacho, J. Chan, K.J. Vahala, and O. Painter *A picogram- and nanometre-scale photonic-crystal optomechanical cavity* Nature **459**, 550-555 (2009)

K.L. Ekinci and M.L. Roukes *Nanoelectromechanical systems* Review of Scientific Instruments, **76**, 061101 (2005)

K.L. Ekinci, Y.T. Yang, and M.L. Roukes *Ultimate limits to inertial mass sensing based upon nanoelectromechanical systems* Journal of Applied Physics **95**, 2682-2689 (2004)

P.S. Epstein *On the resistance experienced by spheres in their motion through gases* Physical Review **23**, pages 710-733 (1923)

Europe. *A European strategy for Key Enabling Technologies - A bridge to growth and jobs* URL `http://ec.europa.eu/enterprise/sectors/ict/key_technologies/index_en.htm` (2012)

R.P. Feynman *There's plenty of room at the bottom* Engineering and Science **23**, 22-36 (1960)

N. Garnier and S. Ciliberto *Nonequilibrium fluctuations in a resistor* Physical Review E **71**, 060101 (2005)

M. Geiselmann, M.L. Juan, J. Renger, J.M. Say, L.J. Brown, F.J. García de Abajo, F. Koppens, and R. Quidant *Three-dimensional optical manipulation of a single electron spin* Nature Nanotechnology **8**, 175-179 (2013)

A.A. Geraci, S.B. Papp, and J. Kitching *Short-range force detection using optically cooled levitated microspheres* Physical Review Letters **105**, 101101 (2010)

J. Gieseler, B. Deutsch, R. Quidant, and L. Novotny *Subkelvin Parametric Feedback Cooling of a Laser-Trapped Nanoparticle* Physical Review Letters **109**, 103603 (2012)

J. Gieseler, L. Novotny, and R. Quidant *Thermal nonlinearities in a nanomechanical oscillator* Nature Physics **9**, 806810 (2013)

S. Gigan, H.R. Boehm, M. Paternostro, F. Blaser, G. Langer, J.B. Hertzberg, K. Schwab, D. Baeuerle, M. Aspelmeyer, and A. Zeilinger *Self-cooling of a micro-mirror by radiation pressure* Nature **444**, 6770 (2006)

M.S. Hanay, S. Kelber, A.K. Naik, D. Chi, S. Hentz, E.C. Bullard, E. Colinet, L. Duraffourg, and M.L. Roukes *Single-protein nanomechanical mass spectrometry in real time* Nature Nanotechnology **7**, 602-608 (2012)

L.O. Heim, J. Blum, M. Preuss, and H.J. Butt *Adhesion and friction forces between spherical micrometer-sized particles* Physical Review Letters **83**, 3328-3331 (1999)

K. Hornberger, S. Gerlich, P. Haslinger, S. Nimmrichter, and Markus Arndt *Colloquium: Quantum interference of clusters and molecules* Reviews of Modern Physics **84**, 157-173 (2012)

G. Huber, F. Schmidt-Kaler, S. Deffner, and E. Lutz *Employing trapped cold ions to verify the quantum Jarzynski equality* Physical Review Letters **101**, 070403 (2008)

G. Hummer and A. Szabo *Free energy reconstruction from nonequilibrium single-molecule pulling experiments* Proceedings of the National Academy of Sciences **98**, 3658-3661 (2001)

J.N. Israelachvili *Intermolecular and Surface Forces* Academic Press

C. Jarzynski *Nonequilibrium equality for free energy differences* Physical Review Letters **78**, 2690-2693 (1997)

R. Kaltenbaek, G. Hechenblaikner, N. Kiesel, O. Romero-Isart, K.C. Schwab, U. Johann, and M. Aspelmeyer *Macroscopic quantum resonators (MAQRO)* Experimental Astronomy **34**, 123-164 (2012)

I. Katz, A. Retzker, R. Straub, and R. Lifshitz *Signatures for a Classical to Quantum Transition of a Driven Nonlinear Nanomechanical Resonator* Physical Review Letters **99**, 040404 (2007)

N. Kiesel, F. Blaser, U. Delic, D. Grass, R. Kaltenbaek, and M. Aspelmeyer *Cavity cooling of an optically levitated submicron particle* Proceedings of the National Academy of Sciences **110**, 1418014185 (2013)

T.J. Kippenberg and K.J. Vahala *Cavity opto-mechanics* Optics Express **15**, 17172-17205 (2007)

S. Knünz, M. Herrmann, V. Batteiger, G. Saathoff, T.W. Hänsch, K. Vahala, and T. Udem *Injection Locking of a Trapped-Ion Phonon Laser* Physical Review Letters **105**, 013004 (2010)

B. Küng, C. Rössler, M. Beck, M. Marthaler, D. Golubev, Y. Utsumi, T. Ihn, and K. Ensslin *Irreversibility on the Level of Single-Electron Tunneling* Physical Review X, **2**, 011001 (2012)

W. Lechner, S.J.M. Habraken, N. Kiesel, M. Aspelmeyer, and P. Zoller *Cavity Optomechanics of Levitated Nanodumbbells: Nonequilibrium Phases and Self-Assembly* Physical Review Letters **110**, 143604 (2013)

T. Li. *Fundamental tests of physics with optically trapped microspheres* PhD thesis (2011)

T. Li, S. Kheifets, D. Medellin, and M. Raizen *Measurement of the instantaneous velocity of a Brownian particle* Science **328**, 1673-1675 (2010)

T. Li, S. Kheifets, and M. Raizen *Millikelvin cooling of an optically trapped microsphere in vacuum* Nature Physics **7**, 527-530 (2011)

K.G. Libbrecht and E.D. Black *Toward quantum-limited position measurements using optically levitated microspheres* Physics Letters A **321**, 99-102 (2004)

R. Lifshitz and M.C. Cross *Nonlinear Dynamics of Nanomechanical and Micromechanical Resonators* Review of Nonlinear Dynamics and Complexity, Wiley-VCH Verlag GmbH & Co. KGaA (2009)

Q. Lin, J. Rosenberg, D.E. Chang, R. Camacho, M. Eichenfield, K.J. Vahala, and O. Painter *Coherent mixing of mechanical excitations in nano-optomechanical structures* Nature Photonics **4**, 236242 (2010).

J. Liphardt, S. Dumont, S.B. Smith, I. Tinoco, and C. Bustamante *Equilibrium information from nonequilibrium measurements in an experimental test of Jarzynski's equality* Science **296**, 1832-1835 (2002)

N. Liu, F. Giesen, M. Belov, J. Losby, J. Moroz, A.E. Fraser, G. McKinnon, T.J. Clement, V. Sauer, and W.K. Hiebert *Time-domain control of ultrahigh-frequency nanomechanical systems* Nature Nanotechnology **3**, 715-719 (2008)

S. Machlup and L. Onsager *Fluctuations and Irreversible Processes* Physical Review **91**, 1505-1512 (1953)

A. Manjavacas and F.J. García de Abajo *Vacuum friction in rotating particles* Physical Review Letters **105**, 113601 (2010)

J. Mertz, O. Marti, and J. Mlynek *Regulation of a microcantilever response by force feedback* Applied Physics Letters **62**, 2344-2346 (1993)

C.H. Metzger and K. Karrai *Cavity cooling of a microlever* Nature **432**, 1002-1005 (2004)

P. Mohanty, D. Harrington, K. Ekinci, Y. Yang, M. Murphy, and M. Roukes *Intrinsic dissipation in high-frequency micromechanical resonators* Physical Review B **66**, 085416 (2002)

T.S. Monteiro, J. Millen, G.A.T. Pender, F. Marquardt, D. Chang, and P.F. Barker *Dynamics of levitated nanospheres: towards the strong coupling regime* New Journal of Physics **15**, 015001 (2013)

J. Moser, J. Guttinger, A. Eichler, M.J. Esplandiu, D.E. Liu, M.I. Dykman, and A. Bachtold *Ultrasensitive force detection with a nanotubemechanical resonator* Nature Nanotechnology **8**, 493-496 (2013)

P.A.M. Neto and H.M. Nussenzveig *Theory of optical tweezers* Europhysics Letters **50**, 702708 (2000)

L.P. Neukirch, J. Gieseler, R. Quidant, L. Novotny, and A.N. Vamivakas *Observation of nitrogen vacancy photoluminescence from an optically levitated nanodiamond* Optics Letters **38**, 2976-2979 (2013)

L. Novotny and B. Hecht *Principles of Nano-Optics* Cambridge University Press, 1st edition (2006)

A.D. O'Connell, M. Hofheinz, M. Ansmann, R.C. Bialczak, M. Lenander, E. Lucero, M. Neeley, D. Sank, H. Wang, M. Weides, J. Wenner, J.M. Martinis, and A.N. Cleland *Quantum ground state and single-phonon control of a mechanical resonator* Nature **464**, 697-703 (2010)

J.F. O'Hanlon *A User's guide to Vacuum Technology* Wiley-Interscience, 3rd edition (2003)

R. Omori, T. Kobayashi, and A. Suzuki *Observation of a single-beam gradient-force optical trap for dielectric particles in air* Optics Letters **22**, 816-818 (1997)

J.B. Pendry *Shearing the vacuum - quantum friction* Journal of Physics: Condensed Matter **9**, 10301 (1997)

J.B. Pendry *Quantum friction-fact or fiction?* New Journal of Physics **12**, 033028 (2010)

G. Pieplow and C. Henkel *Fully covariant radiation force on a polarizable particle* New Journal of Physics **15**, 023027 (2013)

M. Poggio, C. Degen, H. Mamin, and D. Rugar *Feedback Cooling of a Cantilever's Fundamental Mode below 5 mK* Physical Review Letters **99**, 017201 (2007)

M. Poot and H.S.J. van der Zant *Mechanical systems in the quantum regime* Physics Reports **511**, 273-335 2012

H.W.C. Postma, I. Kozinsky, A. Husain, and M.L. Roukes *Dynamic range of nanotube- and nanowire-based electromechanical systems* Applied Physics Letters **86**, 223105 (2005)

T.P. Purdy, R.W. Peterson, and C.A. Regal *Observation of Radiation Pressure Shot Noise on a Macroscopic Object* Science **339**, 801-804 (2013)

B. Richards and E. Wolf *Electromagnetic Diffraction in Optical Systems. II. Structure of the Image Field in an Aplanatic System* Proceedings of the Royal Society of London. Series A. Mathematical and Physical Sciences **253**, 358-379 (1959)

A. Rohrbach and E.H.K. Stelzer *Optical trapping of dielectric particles in arbitrary fields* Journal of the Optical Society of America A **18** 839-853 (2001)

O. Romero-Isart, A.C. Pflanzer, F. Blaser, R. Kaltenbaek, N. Kiesel, M. Aspelmeyer, and J. Cirac *Large Quantum Superpositions and Interference of Massive Nanometer-Sized Objects* Physical Review Letters **107**, 020405 (2011)

O. Romero-Isart, A.C. Pflanzer, M.L. Juan, R. Quidant, N. Kiesel, M. Aspelmeyer, and J.I. Cirac *Optically levitating dielectrics in the quantum regime: Theory and protocols* Physical Review A **83**, 013803 (2011)

O. Romero-Isart, M.L. Juan, R. Quidant, and J.I. Cirac *Toward quantum superposition of living organisms* New Journal of Physics **12**, 033015 (2010)

M.L. Roukes *Plenty of room, indeed* Scientific American **285**, 42-49 (2001)

D. Rugar and P. Gruetter *Mechanical parametric amplification and thermomechanical noise squeezing* Physical Review Letters **67**, 699-702 (1991)

D. Rugar, R. Budakian, H. J. Mamin, and B.W. Chui *Single spin detection by magnetic resonance force microscopy* Nature **430**, 329-332 (2004)

A.H. Safavi-Naeini, S. Gröblacher, J.T. Hill, J. Chan, M. Aspelmeyer, and O. Painter *Squeezed light from a silicon micromechanical resonator* Nature **500**, 185-189 (2013)

O.P. Saira, Y. Yoon, T. Tanttu, M. Möttönen, D. Averin, and J. Pekola *Test of the Jarzynski and Crooks Fluctuation Relations in an Electronic System* Physical Review Letters **109**, 180601 (2012)

J.C. Sankey, C. Yang, B.M. Zwickl, A.M. Jayich, and J.G.E. Harris *Strong and tunable nonlinear optomechanical coupling in a low-loss system* Nature Physics **6**, 707-712 (2010)

A. Schliesser, P. Del'Haye, N. Nooshi, K.J. Vahala, and T.J. Kippenberg *Radiation pressure cooling of a micromechanical oscillator using dynamical backaction* Physical Review Letters **97**, 243905 (2006)

S. Schuler, T. Speck, C. Tietz, J. Wrachtrup, and U. Seifert *Experimental Test of the Fluctuation Theorem for a Driven Two-Level System with Time-Dependent Rates* Physical Review Letters **94**, 180602 (2005)

F. Seifert, P. Kwee, M. Heurs, B. Willke, and K. Danzmann *Laser power stabilization for second-generation gravitational wave detectors* Optics Letters **31**, 2000-2002 (2006)

A.E. Siegman *Lasers* University Science Books (1986)

B.C. Stipe, H.J. Mamin, T.D. Stowe, T.W. Kenny, and D. Rugar *Noncontact friction and force fluctuations between closely spaced bodies* Physical Review Letters **87**, 96801 (2001)

M.D. Summers, D.R. Burnham, and D. McGloin *Trapping solid aerosols with optical tweezers: A comparison between gas and liquid phase optical traps* Optics Express **16**, 7739-7747 (2008)

J.D. Teufel, T. Donner, D. Li, J.W. Harlow, M.S. Allman, K. Cicak, A.J. Sirois, J.D. Whittaker, K.W. Lehnert, and R.W. Simmonds *Sideband cooling of micromechanical motion to the quantum ground state* Nature **475**, 359-363 (2011)

Q.P. Unterreithmeier, E.M. Weig, and J.P. Kotthaus *Universal transduction scheme for nanomechanical systems based on dielectric forces* Nature **458**, 1001-1004 (2009)

Q.P. Unterreithmeier, T. Faust, and J.P. Kotthaus *Nonlinear switching dynamics in a nanomechanical resonator* Physical Review B **81**, 241405 (2010)

K. Usami, A. Naesby, T. Bagci, B.M. Nielsen, J. Liu, S. Stobbe, P. Lodahl, and E.S. Polzik *Optical cavity cooling of mechanical modes of a semiconductor nanomembrane* Nature Physics **8**, 168-172 (2012)

H.C. Van De Hulst *Light scattering by small particles* Dover Publications (1981)

E. Verhagen, S. Deléglise, S. Weis, A. Schliesser, and T.J. Kippenberg *Quantum-coherent coupling of a mechanical oscillator to an optical cavity mode* Nature **482**, 63-67 (2012)

L.G. Villanueva, E. Kenig, R.B. Karabalin, M.H. Matheny, R. Lifshitz, M.C. Cross, and M.L. Roukes *Surpassing Fundamental Limits of Oscillators Using Nonlinear Resonators* Physical Review Letters **110**, 177208 (2013)

L.G. Villanueva, R.B. Karabalin, M.H. Matheny, E. Kenig, M.C. Cross, and M.L. Roukes *A Nanoscale Parametric Feedback Oscillator* Nano Letters **11**, 5054-5059 (2011)

G.M. Wang, E.M. Sevick, E. Mittag, D.J. Searles, and D.J. Evans *Experimental demonstration of violations of the second law of thermodynamics for small systems and short time scales* Physical Review Letters **89**, 50601 (2002)

E. Wolf *Electromagnetic Diffraction in Optical Systems. I. An Integral Representation of the Image Field* Proceedings of the Royal Society of London A: Mathematical and Physical Sciences **253**, 349-357 (1959)

Y.T. Yang, C. Callegari, X.L. Feng, K.L. Ekinci, and M.L. Roukes *Zeptogram-Scale Nanomechanical Mass Sensing* Nano Letters **6** 583-586 (2006)

A. Yariv *Quantum Electronics* Wiley, New York, 3rd edition (1989)

P. Zemánek, A. Jonas, L. Šrámek, and M. Liška *Optical trapping of Rayleigh particles using a Gaussian standing wave* Optics communications **151**, 273-285 (1998)

P. Zemánek, A. Jonas, L. Šrámek, and M. Liška *Optical trapping of nanoparticles and microparticles by a Gaussian standing wave* Optics Letters **24**, 1448-1450 (1999)

J. Zurita-Sánchez, J.J. Greffet, and L. Novotny *Friction forces arising from fluctuating thermal fields* Physical Review A **69**, 022902 (2004)

Acknowledgements

Before I started, most people would tell me that the merit of a PhD thesis is to learn how to deal with frustration. I never really believed that and thought "how bad can it be"? I was sure that if you are determined and willing to put in an extra effort, that sooner or later you will get your results. So I started off in early 2009, highly motivated by the prospect of being the first to achieve the quantum ground state of a macroscopic object. This turned out to be a bit too ambitious. A little more than a year after I had started, ground state cooling was demonstrated by the group of A. Cleland, while I was still struggling with trapping nanoparticles. Similarly, my enthusiasm suffered a mayor setback when T. Li, PhD candidate in the group of M. Raizen, published his work on levitated microspheres in Summer 2010, when I just had managed to trap and was working on the detection, and again a year later when he demonstrated feedback cooling of levitated microspheres in high vacuum, while I was developing the parametric feedback. It seemed like a hopeless struggle, a race I couldn't win. Eventually, I got the parametric feedback to work and three and a half years after the beginning of my PhD, I had my first paper accepted. Later on, it turned out that even though on first sight our setup was very similar to the Raizen experiment, the differences (parametric vs. linear feedback, nanoparticles vs microparticles) were significant enough to do interesting experiments that nobody else could do. Throughout all that time, Romain and Lukas somehow kept me going. I think they believed more in me than I did myself. Thank you for your support and confidence.

It is an unusual situation to have two supervisors, but I am very glad I did. Romain and Lukas are two different "species" of scientists. Nonetheless, they are very good in what they do and I learnt a lot from both of them. Romain, thank you for giving me the opportunity to work on a highly interesting and topical subject and for giving me the freedom and the support to come up and pursue my own ideas, even though quite a few of them never bear any fruits. Lukas, thank you for your professional and personal guidance and the enriching discussions we had. The way you approach science and the clarity of your work will always serve me as a good

example.

ICFO is truly a special place and I hope to see it continue its success story for years to come. Especially, I thank the Human Resources for helping me out with all the administrative hurdles and for making my arrival at ICFO as smooth as possible, the electronic workshop, in particularly Jose-Carlos, Jordi and Ricardo for their endless patience and for helping me to develop the electronics for the parametric feedback and Xavi and his team from the mechanical workshop for finding quick solutions for the vacuum chamber. I really enjoyed the ICFO+ program. Above all, the course on scientific writing by Jean-Luc Doumont was one of the best I have ever taken. I thank Darrick for patiently listening to my theory questions, Matteo and Francois for their advice on the cavity and Jan for is advice on general technical issues. I am also grateful to the people working with me on the trapping project. Brad for explaining all the different detection schemes (homo-, hetero- pseudo-homodyne and phase shifting) to me, even though usually his mind went so fast that it was hard to follow, Mathieu for guiding me through my first experiences in experimental physics, Marko, Vijay and Loïc for bouncing off ideas and proof reading my thesis. The work on the fluctuation theorem would have never become so deep without the contribution of Christoph Dellago. When he joined, it was like someone switching on the lights in a dark room.

Taking the risk of missing someone and realizing it on the day I receive the printed copy of the thesis, I want to acknowledge the people I met inside and outside of ICFO. You have become good friends and I share a lot of good memories with you: Michael, Michelle, Camila, Esteban, Jon, Nilli, Guillaume and Jan & family for Ballena Alegre, Sebas and Nela for caña, bravas and tango, Michael and Sebas for their BBQs, Marta, Pablo, Jan and Michael for having lunch on the beach many times (still, I think we should have gone more often), Giorgio and Mark for welcoming me into the group, Jon, Jan and Esteban for pushing me into crazy runs in Aigüastortes and accross the Garraf, Abadá Capoeira and Nação Zumbi for helping me to keep the balance, Eyal for showing me and Camila around Israel, Rob for runs on the beach, Sebas for inviting me to his home in Argentina, Ze Ger-

man community, Michael, Stefan, Benny, Mussie, Dominik, Don Bratwurst, Sebas for "How beautiful is the life?!", los Sepulvedos (Gustl, Paulinha, Davide) for being my first home in Barcelona and Camila for being my second and hopefully future home. Thanks to all my friends for staying in touch and keeping this friendship alive, Alex & Alex, Max, Alex K., Jan-Simon, Markus, Daniel, Thomas, Diepie, Martin, Ulf, Caro, Asier. I hope I get to see you more often.

Last but surely not least, I thank my family. Vielen Dank für eure Unterstützung all die Jahre. Auch wenn wir uns nur selten sehen, seit ihr sehr wichtig für mich, nicht nur als meine Eltern, Großeltern und Schwester, sondern auch als Vorbilder und Ratgeber. Das Wissen, dass ihr für mich da seit, gibt mir die Sicherheit und das Vertrauen meinen Interessen nachzugehen und meinen Weg zu finden. Ich bin stolz auf euch und freue mich, dass ihr fast vollzählig bei meiner Verteidigung anwesend sein werdet! João, muito obrigado também pelas suas visitas frequentes, pelas comidas boas e por me receber na sua família com muito carinho.

List of Publications

6. **Jan Gieseler**, Marko Spasenović, Lukas Novotny and Romain Quidant
Nonlinear mode-coupling and synchronization of a vacuum-trapped nanoparticle
Physical Review Letters, under review

5. **Jan Gieseler**, Romain Quidant, Christoph Dellago and Lukas Novotny
Dynamic relaxation of nanoscale particle from an initial non-equilibrium steady state
Nature Nanotechnology, under review

4. **Jan Gieseler**, Lukas Novotny and Romain Quidant
Thermal nonlinearities in a nanomechanical oscillator
Nature Physics **9**, 806-810 (2013)

3. Levi P. Neukirch, **Jan Gieseler**, Romain Quidant, Lukas Novotny and A. Nick Vamivakas
Observation of nitrogen vacancy photoluminescence from an optically levitated nanodiamond
Optics Letters **38**, 2976-2979 (2013)

2. **Jan Gieseler**, Brad Deutsch, Romain Quidant and Lukas Novotny
Subkelvin Parametric Feedback Cooling of a Laser-Trapped Nanoparticle
Physical Review Letters **109**, 103603 (2012).

1. F. B. P. Niesler, N. Feth, S. Linden, J. Niegemann, **J. Gieseler**, K. Busch, and M. Wegener
Second-harmonic generation from split-ring resonators on a GaAs substrate
Optics Letters **34**, 1997-1999 (2009).